Miniaturised components for next generation cold-atom quantum sensors

Alan Christopher Bregazzi

A thesis presented in the fulfilment of the requirements for the degree of

Doctor of Philosophy

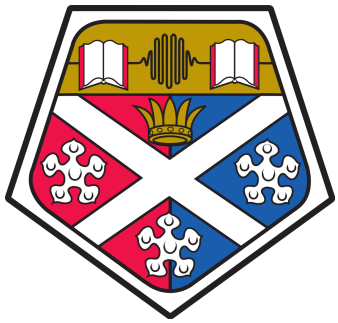

Experimental Quantum Optics and Photonics
Department of Physics and SUPA
University of Strathclyde

May 2024

Declaration

This thesis is the result of the author's original research. It has been composed by the author and has not been previously submitted for examination which has led to the award of a degree. Chapters 4, 6, 7 are partially based on publications by the author of this thesis. Details of these and the extent of the contribution of the author are clearly stated in the relevant chapters.

Signed:

Date:

Abstract

This thesis describes several investigations into different devices and techniques with the aim of reducing both the size and complexity of laser cooling experiments. While the focus here is placed on clocks, many of the techniques could be adapted and extended to different cold-atom sensors.

At the heart of each investigation lies a grating magneto-optical trap (GMOT) that allows the creation of cold-atom clouds of similar size and temperature to traditional 6-beam MOTs. Each experiment described here focuses on a different aspect of the wider systems required in cold-atom devices. Atom imaging along with routes to a maximised performance in microfabricated vacuum chambers are discussed. The possibility of loading optical lattices directly from the GMOT are also investigated. Using the same diffractive optic to load the GMOT, 1D and 3D optical lattices can be produced using a single input beam. This technique simplifies the creation of optical lattices along with improving their robustness to phase noise from the laser due to each lattice beam sharing a common phase. Finally, a cold-atom microwave clock is described and characterised. A short-term stability of $1.5 \times 10^{-11}\tau^{-1/2}$ is demonstrated, averaging down to 2×10^{-12} after 100 s. The short-term stability limit is found to be dominated by signal to noise ratio of the Ramsey fringes while the medium term is dominated by magnetic field noise due to the experiment being magnetically unshilded. Improvements to the experimental system are suggested to help improve the performance of the clock in both the short and long-term. In addition, routes towards a more compact set-up are discussed.

Acknowledgements

It is difficult to adequately thank everyone who has contributed to the completion of this thesis but here is an attempt. Firstly, I would like to thank my two supervisors Erling Riis and Paul Griffin. Throughout my PhD they have always been around to explain or help with a problem and never (outwardly at least) seemed to mind answering my many questions. Without their expert guidance and support I would certainly not be at this stage.

I had the excellent fortune at the start of my PhD to be thrown in the lab with James McGilligan. From James I have learnt many of the vital skills needed to be an effective experimentalist, for which I will always be grateful. In particular, he has passed down the attitude of "JFDI", which has served me well when convincing unruly experiments to work. Special thanks also goes to Aidan Arnold for his sage advise and baffling Mathematica notebooks. More importantly however, for inviting me to his office after my undergraduate viva to float the idea of starting a PhD in the EQOP group. Without this casual chat I would never have considered even applying for a PhD. A big thanks is also due to the Clock Team, past and present, who have made my time in the department, and occasionally the pub, so enjoyable.

In addition to the academics in EQOP, I'd like to extend my appreciation to Gaetano Mileti, Christoph Affolderbach and Etienne Batori who collaborated on the clock project. I especially enjoyed my time in the lab (and climbing wall) with Etienne, who's expertise really helped drive the clock forward.

I would also like to thank my friends and family for all the support and fun times outside of work. In particular, I'd like to acknowledge my mum and dad, who's quiet encouragement was instrumental in me starting down this road. Having such good role models throughout my life has no doubt contributed to any achievements I have had along the way. Now I'm finally finished I can also perhaps begin to answer some of mum's more challenging physics related questions, that continue to surprise and invariably confound me.

Last but not least, I'd like to thank my partner Grace. I'm sure last four years would have been much more difficult without you and I can't wait to see what we do together next.

Contents

List of Figures

List of Tables

List of Acronyms

- **AOM**: Acousto-Optic Modulator
- **ASE**: Amplified Spontaneous Emission
- **CCD**: Charge Coupled Device
- **CO**: Cross-Over
- **CPT**: Coherent Population Trapping
- **CSAC**: Chip-Scale Atomic Clock
- **DAC**: Digital to Analogue Converter
- **DAQ**: Data Acquisition
- **DMD**: Digital Micro-Mirror Device
- **ECDL**: Extended Cavity Diode Laser
- **EQOP**: Experimental Quantum Optics and Photonics
- **EOM**: Electro-Optical Modulator
- **GMOT**: Grating Magneto-Optical Trap
- **GPS**: Global Positioning System
- **GPSDO**: Global Positioning System Disciplined Oscillator
- **LIAD**: Light-Induced Atomic Desorption
- **LGR**: Loop-Gap Resonator
- **MASER**: Microwave Amplification by Stimulated Emission of Radiation
- **MEMS**: Micro-Electromechanical System

- **MOT**: Magneto-optical trap
- **NEG**: Non-Evaporable Getter
- **NPBS**: Non-Polarising Beam Splitter
- **OCXO**: Oven Controlled Crystal Oscillator
- **PD**: Photodiode
- **PBS**: Polarising Beam Splitter
- **POP**: Pulsed Optically Pumped
- **PSD**: Phase Space Density
- **QPN**: Quantum Projection Noise
- **RAFS**: Rubidium Atomic Frequency Standard
- **RIN**: Relative Intensity Noise
- **SLM**: Spatial Light Modulator
- **SWaP** : Size Weight and Power
- **TA** : Tapered Amplifier
- **TOF**: Time of Flight
- **UHV**: Ultra-High Vacuum
- **VBG**: Volume Bragg Grating

Chapter 1

Introduction

Although not generally considered by the average person, the world we live in is only made possible by the extremely precise timekeeping devices now widely available.[1,2] From more obvious examples such as GPS and telecommunications, to the correct functioning of the energy grid and financial systems, we now rely heavily on the remarkable stability and precision provided by atomic frequency references.

The need for precise timekeeping can perhaps be traced back to the famous "Longitude Problem" where in 1714 a prize of £20,000 was offered to anyone who could solve the issue of reliably measuring longitude during sea voyages.[3] At the time, the measurement of latitude was a relatively simple task, accomplished for example by observing the position of the sun relative to the horizon at midday, or using the North Star. Longitude however remained elusive, with the most reliable method being "dead reckoning". This relied on using the ship's speed and time spent travelling to make an estimation of the longitude. The downfalls of this method were becoming more apparent however, with many ships lost due to errors in navigation. Various solutions to the longitude problem were presented and discounted before a clock maker called John Harrison won a partial pay out for his development of the marine chronometer. The development of a sufficiently stable clock allowed the determination of longitude by simply comparing the time between the ship's location, determined by the sun, and the time at some reference point, determined by the marine chronometer. This basic principle of comparing the time at various locations is still used today in GPS, albeit with vastly superior frequency references.

1.1 Atomic Clock Principle

The operating principle of clocks has remained largely unchanged for thousands of years. First, a local oscillator (LO) is required. Originally the orbits of celestial bodies were tracked; their positions in the sky giving a reference as to the time of year or month.[3] For many centuries after their invention in 1656 however, the best clocks relied on the harmonic motion of a swinging pendulum to provide a LO.[1] These days quartz oscillators are most widely used for this task in wrist watches all the way up to atomic clocks. The pervasiveness of quartz oscillators can largely be attributed to the remarkable stabilities possible over short time scales before the oscillator frequency begins to drift, primarily due to thermal effects in the crystal. Secondly, a frequency counter is used to count the periods of oscillation. Without this crucial step one simply has a frequency reference and no firm idea of the actual passage of time can be inferred. In the case of pendulum clocks the harmonic motion of the pendulum is transferred through various gears to make the hands of the clock move, thus providing a counter. The final required step in creating a clock is generally some feedback mechanism to ensure the LO continues to tick at the correct rate. In the case of pendulum clocks this is accomplished by tuning the length of the pendulum. It is interesting to note that the most famous clock in the UK, housed inside Big Ben is adjusted by adding or removing pre-decimalisation pennies onto the pendulum weight. This changes the effective length of the pendulum by shifting its centre of mass, causing the clock mechanism to gain or lose two fifths of a second over twenty four hours.[4]

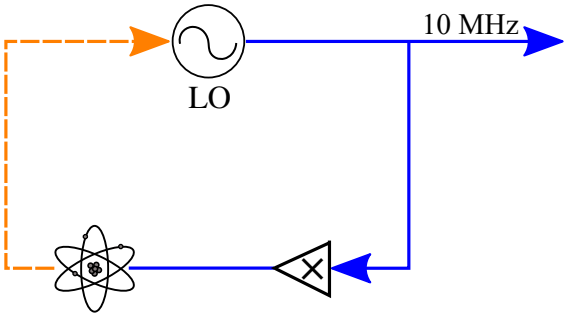

Figure 1.1: Schematic of atomic clock principle. Dashed line indicates error signal used to feedback onto the LO to lock it to the atomic transition.

While the general idea behind clocks has remained unchanged, the details of their operation are now unrecognisable from the early days spent tracking the

motion of the sun and moon. The best clocks today use atomic transitions as the frequency reference to feedback onto the LO (often operating at 10 MHz). To perform this feedback the frequency outputted by the LO is multiplied up to the atomic transition frequency. The atomic transition is then interrogated in some way and the resulting signal used to discern if the LO has drifted since the last measurement. Thus, an error signal can be constructed and the stability of the atomic transition is transferred onto the LO. This basic scheme is shown in Figure 1.1.

Atomic transitions have the notable advantage that all atoms of a specific species exhibit exactly the same transition frequency, governed by quantum mechanics and the universal constants. Despite the large interest in measuring potential variations in these constants,[5] as far as we currently know these transition frequencies also remain constant- assuming no external perturbations on the atom. Atomic transitions are therefore ideally suited towards making both reliable and repeatable measurements of the passage of time.

Another key factor in the increased performance of atomic clocks are the high frequencies of the atomic transitions used, typically in the GHz - THz regime. These high frequencies are divided down to more usable frequencies through the feedback scheme with the final clock output often being a 10 MHz or a one pulse per second signal (pps). Any frequency deviation of the atomic reference is consequentially also divided down, resulting in very high fractional frequency stabilities at the $10^{-10} - 10^{-18}$ level at an interrogation time of 1 s.[6,7]

The vast improvements in time keeping offered by atomic clocks are evident when it is considered that Harrison's H4 marine chronometer on its first voyage lost 5 s over the course of two months,[3] a notable feat at the time. By comparison the best optical clocks are now stable to around 1 s in the age of the universe.[7] Improvements to the accuracy and stability of clocks (especially when in conjunction with portable systems) opens the door to many new applications such as better navigation, more efficient use of power in electricity grids and faster, more reliable telecommunication infrastructure.

1.2 Size-Performance Trade-Off

The focus of this thesis is the demonstration of enabling technologies towards more compact cold-atom sensors, specifically clocks. Much of the system architecture discussed could however also be transferred to other sensors such as

interferometers. A widely used metric that is referred to throughout this thesis is size, weight and power (SWaP). This provides a very useful means of assessing the overall suitability of a device to be used outside of a laboratory environment where power and space are at a premium.

There exists a natural trade-off between the SWaP of a clock and its performance.[6] The chip-scale atomic clock (CSAC)[8] initially developed by NIST remains unrivalled in terms of its SWaP. Although extremely compact with a very low power consumption, its performance when compared to many other atomic clocks is modest. This highlights the need for a device to fit the task at hand. While CSAC performance is not as good as other larger clocks it is more than sufficient for many tasks and consequentially has had a large impact on the compact clock market, with over 100,000 devices already sold.[9] When constructing cold-atom clocks it must be acknowledged that the overall SWaP of the device will be much larger than many atomic vapour based devices, however the performance (if designed well) should far exceed that offered by the more compact vapour based clocks.

1.3 Future Frequency Standards

Since 1967 the SI second has been defined as "The duration of 9,192,631,770 periods of the radiation corresponding to the transition between the two hyperfine levels of the ground state of the caesium 133 atom".[2] In the next decade or so, this is expected to be updated and recast in terms of an optical transition due to the remarkable performance now offered by optical clocks[10] over the more traditional microwave based fountain clocks.[11]

This redefinition will eventually necessitate more compact and practical optical clocks. Some of the best optical clocks are based around atoms held in an optical lattice,[10] probing optical transitions with Hz level linewidth. While the launched cold atom clouds of current atomic fountain clocks offer a vastly increased interrogation time over thermal atomic beams, they are limited by the expansion of the cloud and practical considerations as to the maximum height atoms can be launched. By contrast, atoms can be held without loss of coherence in optical lattices for up to several seconds[12] which combined with the increased frequency (THz) of the interrogated transition results in vastly superior frequency references. Recently a Sr optical lattice clock demonstrated an experimental measurement of the gravitational redshift between two atomic clocks

realised just millimetres apart, highlighting the vast potential of these emerging frequency standards[7]

The complexity and sensitivity of these systems however necessitates that they are currently almost exclusively lab-based with high power consumption. With the redefinition of the SI second, more widespread and robust optical clocks will become vital to leveraging the improved timing capabilities of the new standard. Initially fundamental research will benefit most from this redefinition,[2] however, in time commercial and industrial applications will reach maturity, requiring improved frequency standards for the continuing proper functioning of the world we live in.

1.4 Publications Arising from this Work

Articles

- **A. Bregazzi**, P. F. Griffin, A. S. Arnold, D. P. Burt, G. Martinez, R. Boudot, J. Kitching, E. Riis, and J. P. McGilligan, "A simple imaging solution for chip-scale laser cooling," *Applied Physics Letters*, **119** 184002 (2021)

This paper constitutes the basis of Section 4.1.

- **A. Bregazzi**, P. Janin, S. Dyer, J. P. McGilligan, O. Burrow, E. Riis, D. Uttamchandani, R. Bauer, and P. F. Griffin, "Cold-atom shaping with MEMS scanning mirrors," *Optics Letters*, **48**, 37 (2022)

This paper constitutes the basis of Section 4.2.

- S. Dyer, K. Gallacher, U. Hawley, **A. Bregazzi**, P. Griffin, A. Arnold, D. Paul, E. Riis, and J. McGilligan, "Chip-scale packages for a tunable wavelength reference and laser cooling platform," *Physical Review Applied*, **19**, 044015 (2023)

- E. Batori, **A. Bregazzi**, B. Lewis, P. F. Griffin, E. Riis, G. Mileti, and C. Affolderbach, "An additive-manufactured microwave cavity for a compact cold-atom clock," *Journal of Applied Physics*, **133**, 224401 (2023)

- **A. Bregazzi**, E. Batori, B. Lewis, C. Affolderbach, G. Mileti, E. Riis and P. F. Griffin "A cold-atom Ramsey clock with a low volume physics package," *Scientific Reports*, **14**, 931 (2024)

The above two papers form the basis of the discussion presented in Chapter 6-7.

- In preparation: "Single-beam grating-chip 3D and 1D optical lattices"

Conferences Proceedings

- **A. Bregazzi**, J. Mcgilligan, A. Arnold, P. Griffin, and E. Riis, "Grating magneto-optical trap with integrated magnetic chip," in Conference proceedings, EFTF-IFCS 2022, Apr. 2022

- J. McGilligan, **A. Bregazzi**, S. Dyer, P. F. Griffin, A. S. Arnold, and E. Riis, "Progress towards a fully integrated cold-atom measurement platform," in Optical and Quantum Sensing and Precision Metrology II (S. M. Shahriar and J. Scheuer, eds.), SPIE, Mar. 2022

- **A. Bregazzi**, P. F. Griffin, A. S. Arnold, D. P. Burt, G. Martinez, R. Boudot, J. Kitching, E. Riis, and J. P. McGilligan, "Imaging solutions for a planar stacked MOT," in Conference proceedings, EFTF-IFCS 2022, Apr. 2022

- **A. Bregazzi**, E. Batori, B. Lewis, C. Affolderbach, G. Mileti, E. Riis, and P.Griffin, "A compact cold-atom double-resonance clock," in Quantum Sensing, Imaging, and Precision Metrology (S. M. Shahriar and J. Scheuer, eds.), SPIE, Mar. 2023

Chapter 2

Theory

The following chapter lays out much of the general theoretical understanding for results presented throughout this thesis. Where more theoretical work regarding specific experiments is required it will be presented in the corresponding chapter. It is worth noting that in the interest of brevity, derivations are kept to a minimum throughout this thesis. References to the original works are made when appropriate.

2.1 Atomic Structure

Alkali metals have a single outer valence electron, similar to hydrogen. This makes them comparatively simple to model and predict the behaviour of and is one of the primary reasons they feature so heavily in spectroscopic experiments. The orbital angular momentum of the valence electron around the nucleus is denoted by the quantum number L, and takes integer values between the limits $0 \leq L \leq n-1$, where n is the principal quantum number. This orbital angular momentum couples to the intrinsic spin of the electron, S, with the total angular momentum of the electron, J, taking values $|L-S| \leq J \leq L+S$. It is this L-S coupling that results in the atomic fine structure.[13]

In addition to electronic spin, the nucleus itself has an associated intrinsic spin, the angular momentum of which is indicated by I. Coupling of this nuclear spin with the total electronic spin results in the total atomic angular momentum, F. As before, F takes integer values $|I-J| \leq F \leq I+J$. This additional coupling regime results in the atomic hyperfine structure.[13] The various quantum numbers of a given energy level are described using the spectroscopic notation: $n^{2S+1}L_J$. A final energy level splitting of F levels into m_F sub-levels due to applied magnetic

fields is discussed in Sec 2.1.1. When the energy splitting induced by this magnetic field is small in comparison to the hyperfine splitting, the quantum number F provides a good description of the atomic behaviour.

2.1.1 Magnetic Field Shift

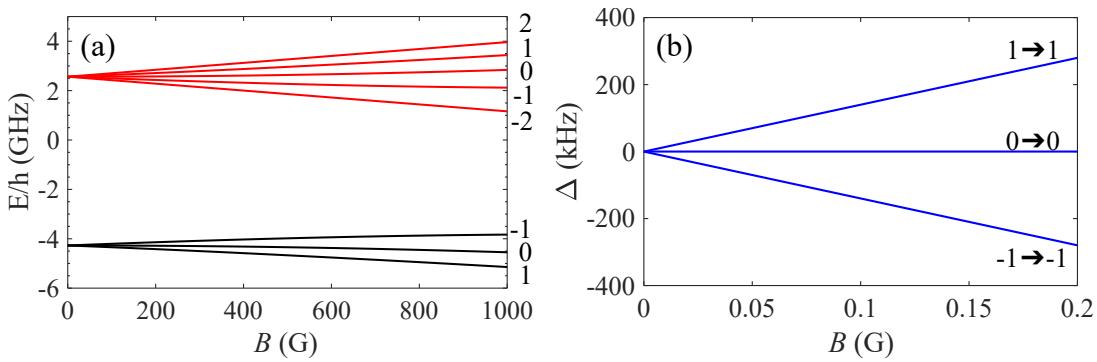

Figure 2.1: (a) Zeeman splitting of ^{87}Rb $F = 2$ (red lines) and $F = 1$ (black lines) hyperfine groundstates ($5^2S_{1/2}$). Numbers to right of plot indicate the specific m_F Zeeman state. (b) Frequency shift of $\Delta m_F = 0$ (π) transitions in hyperfine groundstate.

In the presence of a static magnetic field, B, defined as pointing along z, the hyperfine levels split further into $2F + 1$ so called Zeeman sub-levels. These additional levels, denoted by m_F, take integer values within the limits $-F \leq m_F \leq F$.

The energy splitting of these new levels can be calculated by considering the interaction Hamiltonian describing the contribution from orbital and nuclear spin components. If the energy shift is small compared to the hyperfine splitting, F can be considered a good quantum number and the interaction Hamiltonian is expressed as[14]

$$H_B = \mu_B g_F \frac{F_z}{\hbar} B_z, \tag{2.1}$$

where μ_B is the Bohr Magneton and g_F, the hyperfine Landé g-factor, is given by

$$g_F = g_J \frac{F(F+1) - I(I+1) + J(J+1)}{2F(F+1)} + g_I \frac{F(F+1) + I(I+1) - J(J+1)}{2F(F+1)}, \tag{2.2}$$

where g_J is the Landé factor and g_I is the nuclear g-factor. In the limit of low fields and to a first order approximation the Zeeman splitting is then given by

$$\Delta E_{|m_F\rangle} = m_F g_F \mu_B B. \tag{2.3}$$

A more precise calculation of Zeeman splitting, valid for the ground sate with $L = 0$ can be carried out using the Breit-Rabi equation,[14]

$$E_{|F,m_F\rangle} = -\frac{\Delta E_{hfs}}{2(2I+1)} + g_I \mu_B m B \pm \frac{\Delta E_{hfs}}{2}\left(1 + \frac{4mx}{2I+1} + x^2\right)^{1/2}, \tag{2.4}$$

where $m = m_I \pm m_J$, with the $\pm$ sign taken to be the same as in Eq 2.4. The hyperfine splitting is described by $\Delta E_{hfs} = A_{hfs}(I+1/2)$ with the quantity A_{hfs}, the magnetic dipole constant, being experimentally determined.[14] Finally,

$$x = \frac{(g_J - g_I)\mu_B B}{\Delta E_{hfs}}. \tag{2.5}$$

During the clock investigation (Chapter 6-7), this normal Zeeman effect is of critical importance. A small magnetic bias field is used to lift the degeneracy of the Zeeman sublevels and define a quantisation axis for the microwave cavity field to drive π transitions. It is clear from Eq 2.4 that a strong understanding of both the magnetic field strength and stability is required when characterising the clock accuracy and stability. Interrogating the $m_F = 0 \rightarrow m_F = 0$ transition reduces the clock frequency sensitivity as the atomic energy levels are only sensitive to a second order Zeeman shift with respect to magnetic field strength. This second order Zeeman shift is calculated as 575.15 Hz/G^2,[14] in contrast to the much higher $m_F = \pm 1 \rightarrow m_F = \pm 1$ sensitivity of 1.4 MHz/G, emphasised in Figure 2.1(b). The residual frequency sensitivity must still be carefully considered when constructing the clock error budget however.

When driving atomic transitions between m_F levels using linearly, π, polarised light $\Delta m_F = 0$. Right (left) hand circularly polarised light is denoted by σ^+ (σ^-) and results in $\Delta m_F = +1$ ($\Delta m_F = -1$). This useful naming convention is used throughout this thesis and is valid for both electric dipole and magnetic dipole transitions.

2.2 Interactions of Light and Atoms

To describe a two level atom (as shown in Figure 2.2) with the energy states $|g\rangle$ and $|e\rangle$ we shall first consider the Hamiltonian of the system, $\hat{H}$. This consists

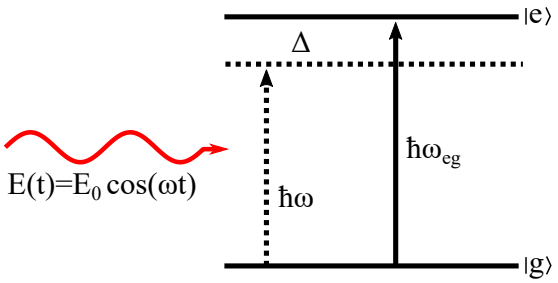

Figure 2.2: Energy levels of two level atom and driving laser field detuned by Δ from the excited state, $|e\rangle$.

of the sum of the atom Hamiltonian, $\hat{H}_a$, and the atom-light interaction Hamiltonian, $\hat{H}_i$, that couples the two atomic states in the absence of spontaneous emission,

$$\begin{aligned}\hat{H} &= \hat{H}_a + \hat{H}_i \\ &= E_g \left|g\right\rangle \left\langle g\right| + E_e \left|e\right\rangle \left\langle e\right| - \vec{d} \cdot \vec{E}(t),\end{aligned} \tag{2.6}$$

where $\vec{E}(t) = \vec{E_0} cos(\omega t)$ describes the light field, $E_n = \hbar\omega_n$ and $\vec{d}$ is the electric dipole operator. The evolution of a quantum state,

$$\left|\Psi(t)\right\rangle = \sum_n c_n(t) \left|n\right\rangle e^{-i\omega_n t} = c_g(t) e^{-i\omega_g t} \left|g\right\rangle + c_e(t) e^{-i\omega_e t} \left|e\right\rangle, \tag{2.7}$$

where $c_n(t)$ is the given state amplitude, is described by the Schrödinger equation,

$$i\hbar \frac{d}{dt} \left|\Psi(t)\right\rangle = \hat{H} \left|\Psi(t)\right\rangle. \tag{2.8}$$

This can in turn then be expressed in terms of time-dependent coefficients by substituting Eq 2.7 into Eq 2.8, where the index k describes the state of interest,

$$i\hbar \dot{c}_k(t) = \sum_n c_n(t) e^{-i\omega_{nk} t} \left\langle n\right| \hat{H}_i \left|k\right\rangle. \tag{2.9}$$

This then results in the rate equations

$$i\dot{c}_g(t) = c_e(t)\Omega \; cos(\omega t) e^{-i\omega_{eg}} = c_e(t) \frac{\Omega}{2} \left[e^{i(\omega_{eg} - \omega)t} + e^{-i(\omega_{eg} + \omega)t} \right], \tag{2.10a}$$

$$i\dot{c}_e(t) = c_g(t)\Omega \; cos(\omega t) e^{i\omega_{eg}} = c_g(t) \frac{\Omega}{2} \left[e^{i(\omega_{eg} + \omega)t} + e^{-i(\omega_{eg} - \omega)t} \right]. \tag{2.10b}$$

Here the Rabi frequency, Ω, is introduced. This essentially describes the atom-light coupling strength and is defined as

$$\Omega_{eg} = \frac{\langle e| \, d \cdot E_0 \, |g\rangle}{\hbar}. \tag{2.11}$$

Eq 2.10 can be further simplified with the substitution $\Delta = \omega - \omega_{eg}$ in additon to using the rotating wave approximation where fast oscillating terms containing $(\omega_{eg} + \omega)$ are ignored as they do not contribute to the dynamics of interest,[13] finally giving

$$i\dot{c}_g(t) = c_e(t)\frac{\Omega}{2}e^{i\Delta t}, \tag{2.12a}$$

$$i\dot{c}_e(t) = c_g(t)\frac{\Omega}{2}e^{-i\Delta t}. \tag{2.12b}$$

2.2.1 Rabi Oscillations

A key concept required for the microwave clock investigations is that of Rabi oscillations and microwave pulse areas. Beginning from Eq 2.12 it is possible to show that the probability amplitude of a given state after a time, τ, spent interacting with a electromagnetic field is given by[15]

$$\begin{aligned} c_g(t_0+\tau) = e^{i\Delta\tau/2}\Bigg\{ & c_e(t_0)e^{i(\Delta t_0+\phi)}\left[-i\, sin\theta\, sin\left(\frac{\Omega_r\tau}{2}\right)\right] \\ & + c_g(t_0)\left[cos\left(\frac{\Omega_r\tau}{2}\right) + i\, cos\theta\, sin\left(\frac{\Omega_r\tau}{2}\right)\right]\Bigg\} \end{aligned} \tag{2.13a}$$

$$\begin{aligned} c_e(t_0+\tau) = e^{-i\Delta\tau/2}\Bigg\{ & c_e(t_0)\left[cos\left(\frac{\Omega_r\tau}{2}\right) - i\, cos\theta\, sin\left(\frac{\Omega_r\tau}{2}\right)\right] \\ & + c_g(t_0)e^{-i(\Delta t_0+\phi)}\left[-i\, sin\theta\, sin\left(\frac{\Omega_r\tau}{2}\right)\right]\Bigg\}. \end{aligned} \tag{2.13b}$$

The off-resonant Rabi frequency is given by $\Omega_r = \sqrt{\Omega_{eg}^2 + \Delta^2}$. In addition, θ is defined between the limits $0 \leq \theta \leq \pi$ by: $sin\theta = \Omega_{eg}/\Omega_r$, $cos\theta = -\Delta/\Omega_r$.

The probability of finding an atom in a given state at time τ is found by taking the modulus squared of Eq 2.13, this equation is normalised such that $|c_e|^2 + |c_g|^2 = 1$. When plotted as a function of τ the atomic population is

found to oscillate sinusoidally between the ground and excited states at the Rabi frequency, these characteristic oscillations are known as Rabi oscillations or Rabi flopping.[15]

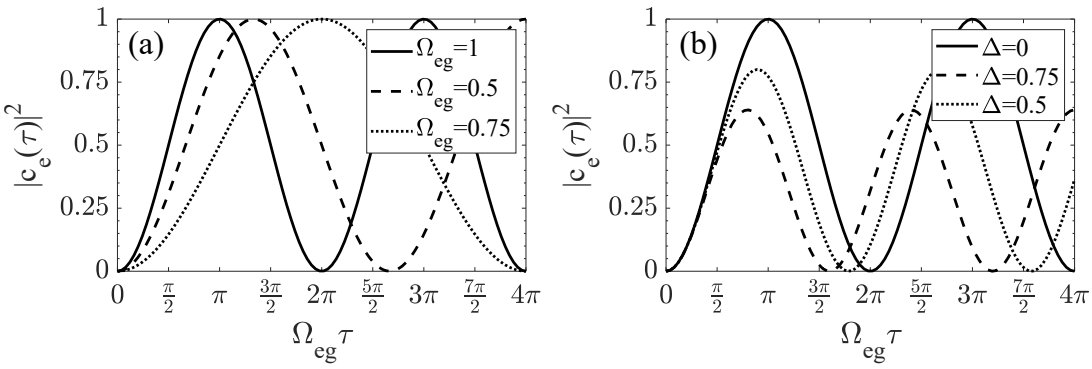

Figure 2.3: Theoretical Rabi oscillations, $|c_g(0)|^2 = 1$. (a) Rabi oscillations plotted for different Rabi frequencies with $\Delta = 0$. (b) Rabi oscillations plotted for different detunings with $\Omega_{eg} = 1$

Figure 2.3 shows Rabi oscillations for various detunings and Rabi frequencies for an atom initially in $|g\rangle$. From the solid black plots of Figure 2.3 we see when a pulse of duration $\Omega_{eg}\tau = \pi$ is applied the atomic population inverts from $|g\rangle$ to $|e\rangle$. This is known as a π pulse. Similarly, to reach an equal superposition state a $\pi/2$ pulse is required. This concept of π and $\pi/2$ pulses is used extensively in Ramsey-type clocks and atom interferometry.[15]

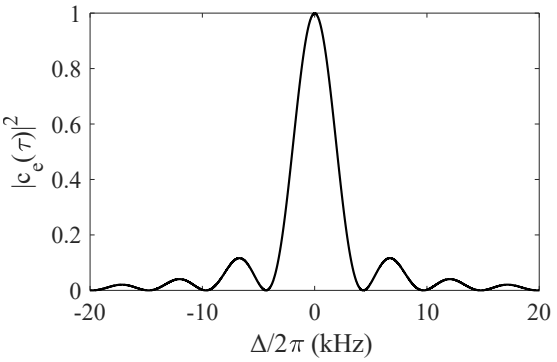

Figure 2.4: Excited state population for $|c_g(t = 0)|^2 = 1$ as a function of detuning. Plotted for τ=200 μs, $\Omega_{eg} = \pi/\tau$

During a clock sequence microwave pulses with a square amplitude modulation are usually applied and the frequency scanned to map out the resonance. This square wave appears as a spread in frequencies in the Fourier domain, the interference of which creates a characteristic sinc^2 distribution shown in Figure 2.4

with a central linewidth,

$$\Delta f = \frac{\Delta\omega}{2\pi} = \frac{1}{\tau}. \tag{2.14}$$

This method of probing a transition was first used in cold atoms to interrogate the groundstate splitting of caesium by Sesko and Wieman.[16] Here the authors were able to observe a resonance linewidth of 50 Hz, helping to lay the foundations for precision spectroscopy in cold atoms.

2.2.2 Ramsey Oscillations

The accuracy of a frequency standard is proportional to the reference signal's quality factor $Q = f_0/\Delta f$. The central frequency of the signal, f_0, is set by the atomic transition frequency. Therefore to increase the quality factor one must reduce the linewidth of the signal. One method of reducing the linewidth of the locking signal is to use Ramsey's separated oscillating fields method.[17]

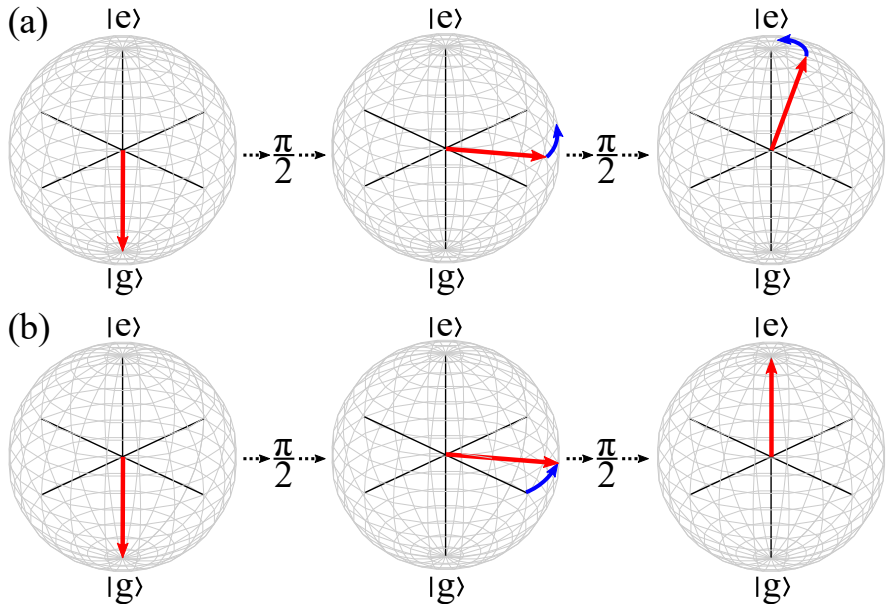

Figure 2.5: Bloch sphere visualisation of Ramsey interrogation. Atom initially in $|g\rangle$ is excited by $\pi/2$ pulse to superposition state. Atomic phase freely precesses around Bloch sphere during T_R before being excited by second $\pi/2$ pulse. LO phase or frequency detuning from atoms results in incomplete excitation to $|e\rangle$ shown in (a). LO phase and frequency being the same as the atoms results in perfect excitation to $|e\rangle$ as with (b).

This method applies a first $\pi/2$ pulse for $t = \tau$ to prepare the atoms in a

superposition state. From here the atomic phase is free to evolve in the dark for $t = T_R$, the "Ramsey time". In the Bloch sphere picture this corresponds to a vector precessing around the equator (see Figure 2.5). A second $\pi/2$ pulse is then applied. If the frequency and phase of the light is perfectly resonant with the atoms the sum of the two $\pi/2$ pulses results in perfect transfer to the upper state (north pole on the Bloch sphere). If however the frequency is detuned from resonance or a phase difference between the atoms and light has accumulated, the result is an incomplete transfer. This process can be modelled by successive applications of Eq 2.13, assuming $\Delta\phi = 0$ and $|c_e(t=0)|^2 = 0$, this results in[1]

$$|c_e(2\tau + T_R)|^2 = 4\frac{\Omega_{eg}^2}{\Omega_r^2} sin^2\left(\frac{\Omega_r \tau}{2}\right)\left[cos\left(\frac{\Delta T_R}{2}\right) cos\left(\frac{\Omega_r \tau}{2}\right) - \frac{\Delta}{\Omega_r} sin\left(\frac{\Delta T_R}{2}\right) sin\left(\frac{\Omega_r \tau}{2}\right)\right]^2. \tag{2.15}$$

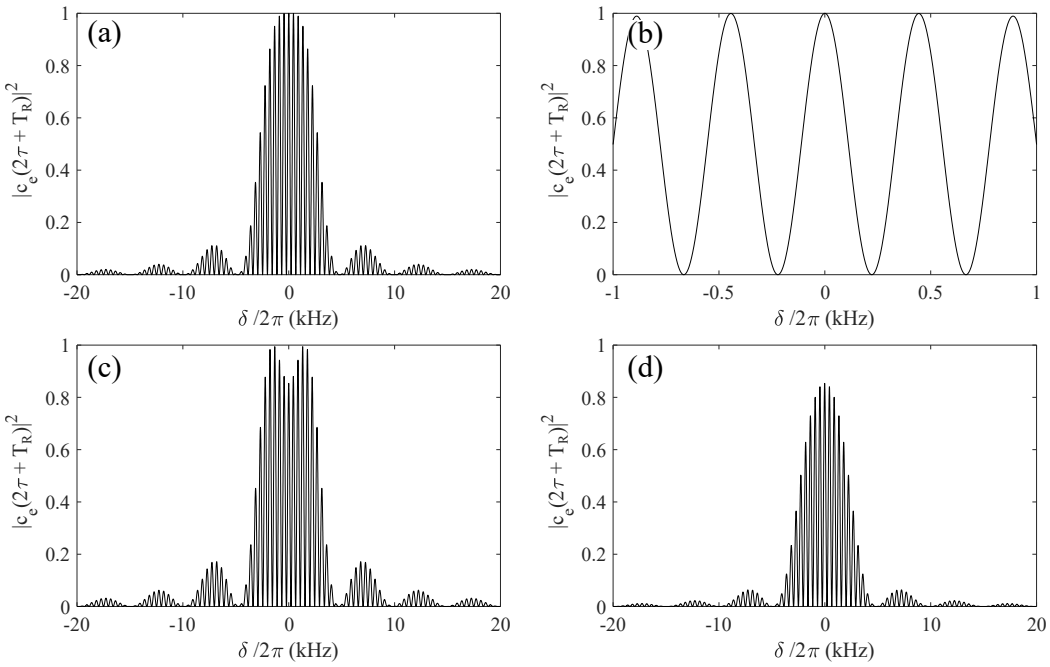

Figure 2.6: Theoretical Ramsey fringes, $T_R = 3$ ms, $\tau = 200$ μs. (a) Ramsey fringe plotted for $\Omega_{eg} = \pi/2\tau$. (b) Central oscillations of fringe. (c) Ramsey fringe plotted for $\Omega_{eg} = 1.25\pi/2\tau$. (d) Ramsey fringe plotted for $\Omega_{eg} = 0.75\pi/2\tau$.

A plot of a resulting Ramsey fringe with perfect $\pi/2$ pulse areas is shown in Figure 2.6(a-b), showing the interference effect between the two pulses. Fig-

ures 2.6(c) and (d) show the fringe pattern when over and under driving the transition respectively. The effect of the fringe interference is to create a sinusoidal modulation of the larger Rabi pedestal, centred on $\Delta = 0$. The narrowing effect of this process on the resonance is clear, resulting in a new linewidth proportional to the Ramsey time,

$$\Delta f = \frac{1}{2T_R}. \tag{2.16}$$

Ramsey's method was quickly adopted by the clock community,[18] notably in beam clocks.[1] Subsequently it was used in the first atomic fountain spectroscopy on sodium,[19] paving the way for the current realisation of the SI second. Cold-atom clouds are ideally suited here due to the long coherence lifetimes typical of cold-atoms allowing T_R to be extended further than possible with thermal ensembles.

2.2.3 Magnetic Dipole Transitions

The previous sections discussed electric dipole transitions, magnetic dipole transitions as used in the clock experiment are described in much the same way. Instead of being coupled by an oscillating electric field as with Eq 2.6 the two atomic levels are now coupled by a magnetic field,

$$\vec{B} = \vec{B_0} cos(\omega t + \phi). \tag{2.17}$$

This modifies the system Hamiltonian,

$$\begin{aligned} \hat{H} &= \hat{H}_a + \hat{H}_i \\ &= E_g \left|g\right\rangle \left\langle g\right| + E_e \left|e\right\rangle \left\langle e\right| - \vec{\mu} \cdot \vec{B}(t), \end{aligned} \tag{2.18}$$

where μ is the magnetic dipole operator. The Rabi frequency in this case is expressed as

$$\Omega_{eg} = \frac{\left\langle e\right| \mu \cdot B_0 \left|g\right\rangle}{\hbar}. \tag{2.19}$$

The theoretical treatment of Rabi and Ramsey oscillations remains the same with these minor modifications.

2.3 Rubidium Level Structure

A key element used in many laser cooling experiments is rubidium. Two isotopes of this element occur naturally, ^{85}Rb and ^{87}Rb in a relative abundance of 72.17% and 27.83% respectively.[14,20] One major practical benefit to using Rb in cold atom experiments is that the wavelengths of the primary Rb absorption lines, known as D_1 (795 nm) and D_2 (780 nm), are accessible to relatively inexpensive diode lasers.[21] It is also easy to trap a high number of atoms from a background vapour and cool the sample to a few μK using sub-Doppler cooling techniques (Sec.2.4.1) due to the well-resolved hyperfine structure of the excited state.

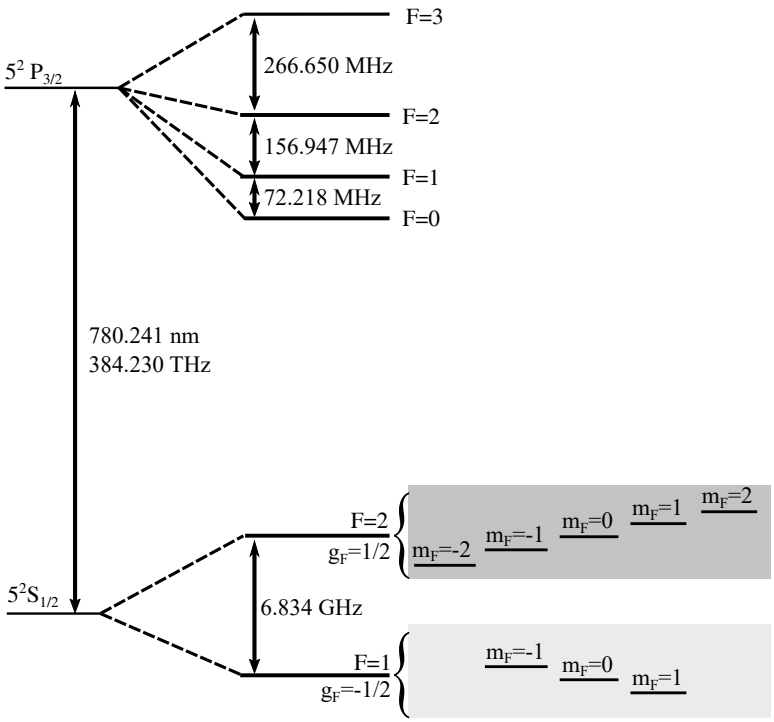

Figure 2.7: Left: ^{87}Rb D_2 line level structure, frequencies taken from Ref.[14]

Throughout the course of this work only ^{87}Rb will be considered. Although this isotope has a lower natural abundance than its ^{85}Rb counterpart, corresponding to a lower trapped atom number for the same experimental conditions, the groundstate-splitting in ^{87}Rb is larger by a factor of $\approx$2.[14,20] This fact becomes an important consideration for the creation of microwave atomic clocks probing the ground-state-splitting, as larger clock transition frequencies result in a higher relative accuracy. This is also one of the primary reasons that optical clocks now demonstrate the highest achievable relative accuracies of any frequency reference by probing transitions in the THz regime. Figure 2.7 shows the fine, hyperfine

and Zeeman energy level structure for the ^{87}Rb D_2 line.

2.4 Laser Cooling

The velocity distribution of a thermal cloud of atoms is given by the Maxwell-Boltzmann distribution. The most probable velocity of an atom of mass m and temperature T in this distribution is given by:

$$\bar{v} = \sqrt{\frac{2k_B T}{m}}, \tag{2.20}$$

where k_B is the Boltzmann constant. A room temperature ensemble of Rb atoms therefore has a velocity of around 200 m/s. By contrast, atoms cooled to 3 μK only travel at around 2 cm/s. Reducing the atomic velocity correspondingly increases the average time interval for an atom to collide with either the cell wall or another atom, drastically increasing the coherence lifetime. This is the core reason laser cooling has become so widespread in atomic physics and has allowed truly remarkable improvements in metrology.

The groundwork for laser cooling was largely laid in the 1970s and 1980s with seminal works on the deceleration of an atomic beam,[22] optical molasses[23] and magneto-optical traps.[24] Informative overviews of the history of laser cooling and the general ideas behind it can be found in the Nobel Prize lectures of W. Phillips,[25] S. Chu[26] and C. Cohen-Tannoudji.[27] Many in-depth reviews are also available on the subject such as Ref.[28,29]

2.4.1 Optical Molasses

When a photon of momentum p is absorbed by an atom, the atom recoils with a momentum equal to that of the absorbed photon,

$$p = mv_{recoil} = \hbar k, \tag{2.21}$$

where v_{recoil} is the atom recoil velocity and k is the wave number of the light. This transfer of momentum is the origin of the optical molasses and the basis of laser cooling. When the photon is re-emitted another small recoil of the atom occurs. Due to the isotropic nature of this spontaneous process however, over many absorption cycles the atom recoil due to photon emission sums to zero and does not contribute to a momentum change of the atom. When considering an

atom travelling anti-parallel to a beam of photons from a laser, it is clear to see that over many photon scattering events enough momentum will be transferred to the atom to slow it down, eventually stopping the atom all together and then accelerating it in the opposite direction. The key step towards making this momentum transfer useful for laser cooling is the introduction of a second overlapping counter-propagating beam and the red detuning of both beams ($\Delta < 0$). Assuming a two level atom in steady state, the scattering rate for a single beam of intensity I is given by

$$R_{\text{sc}}(I, \Delta) = \frac{\Gamma}{2} \frac{I/I_S}{1 + I/I_S + (2\Delta/\Gamma)^2}, \tag{2.22}$$

where I is the light intensity, I_S is the saturation intensity of the transition and Γ is the natural linewidth of the excited state. I_S is defined such that $I/I_S = 2(\frac{\Omega}{\Gamma})^2$ and can be calculated or looked up for different transitions in Ref.[14] The force on the atom from one beam can then be expressed by

$$F = \frac{dp}{dt} = R_{\text{sc}}(I, \Delta)\hbar k. \tag{2.23}$$

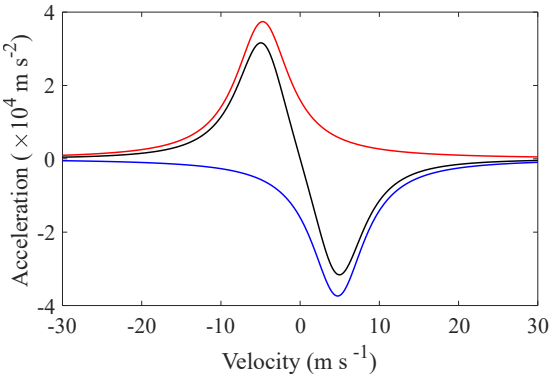

Figure 2.8: Acceleration experienced by atoms in a 1D optical molasses as a function of their velocity. The red and blue lines indicate the acceleration due to each counter-propagating laser. The black line shows the total acceleration as a result of the two lasers. Plotted for ^{87}Rb where $I = I_S = 1.67\,\text{mWcm}^{-2}$, $I_T = 2I$, $\Delta = -\Gamma$.

Due to the Doppler effect an atom moving at some velocity, v, will observe the light to be shifted in frequency compared to if it were at rest; with a shift given by $\omega' = \omega - \vec{k} \cdot \vec{v}$ where ω is the light angular frequency in the resting frame and v is the atom velocity. As an atom moves towards one of the beams the photon frequency observed by the atom will be blue shifted towards resonance while the

light from the other beam will be further red-shifted away from resonance. This results in the atom scattering many more photons from the beam it is propagating towards, resulting in a higher force opposing the direction of travel of the atom. The total force from the two beams is the sum of the independent contributions from each beam:

$$F = \frac{\hbar k \Gamma}{2}\left(\frac{I/I_S}{1 + I_T/I_S + (\frac{2\Delta - 2kv}{\Gamma})^2} - \frac{I/I_S}{1 + I_T/I_S + (\frac{2\Delta + 2kv}{\Gamma})^2}\right), \tag{2.24}$$

where I_T is the total light intensity. The acceleration, a, from the two beams is found to be balanced for atoms with zero velocity component in the laser axis (shown in Figure 2.8). When generalised to 3D using three orthogonal, counter-propagating pairs of lasers, this effect is known as 'optical molasses' due to the atoms experiencing a decelerating force proportional to velocity in all directions, similar to a viscous fluid.[29,30]

Atoms in the velocity class $v < v(a_{max})$ are able to be slowed using this technique, giving a minimum stopping distance of $x = v^2/2a_{max}$, this relation can be seen as the origin of the coupling of trapped atom number to optical overlap volume discussed in detail in Sec 4.1.3.

Although able to cool atoms to very low temperatures (discussed in detail in Sec 2.4.4 onward), an optical molasses is not, however, a trap as the slow moving atoms are able to diffuse out of the beam overlap region via Brownian motion and are thus not spatially localised. To achieve spatial localisation of the atoms one final ingredient is required.

2.4.2 Magneto-Optical Traps

By combining optical molasses and a spatially varying magnetic field, a position dependent force can be applied to the atoms, allowing both cooling and trapping of dense atomic clouds. Due to the Zeeman effect when an atom is placed in a magnetic field its hyperfine energy levels split into m_F sublevels with a splitting (to first order) proportional to the magnitude of the field, given by Eq 2.3. Here we consider the 1D case of a red detuned counter-propagating pair of beams of the same circular polarisation, passing through the zero B field centre point of a linear magnetic field gradient, shown in Figure 2.9. When parallel with the magnetic field these lasers drive σ^+ transitions in the atoms, simultaneously driving σ^- transitions in the anti-parallel case. As a result, as an atom moves from the

zero field centre point it experiences a larger Zeeman shift in its energy sublevels, bringing the transition frequency into resonance with the light. Therefore as an atom moves further from the centre point the probability of scattering a photon and being pushed back towards the centre where the forces are balanced is greater, resulting in a position dependent force on the atoms. This 1D case can be extended to 3D using the quadrupole field generated by an anti-Helmholtz coil pair and the overlap volume of three pairs of counter-propagating orthogonal lasers of appropriate circular polarisation for each trap axis, as set by the direction of the magnetic field.

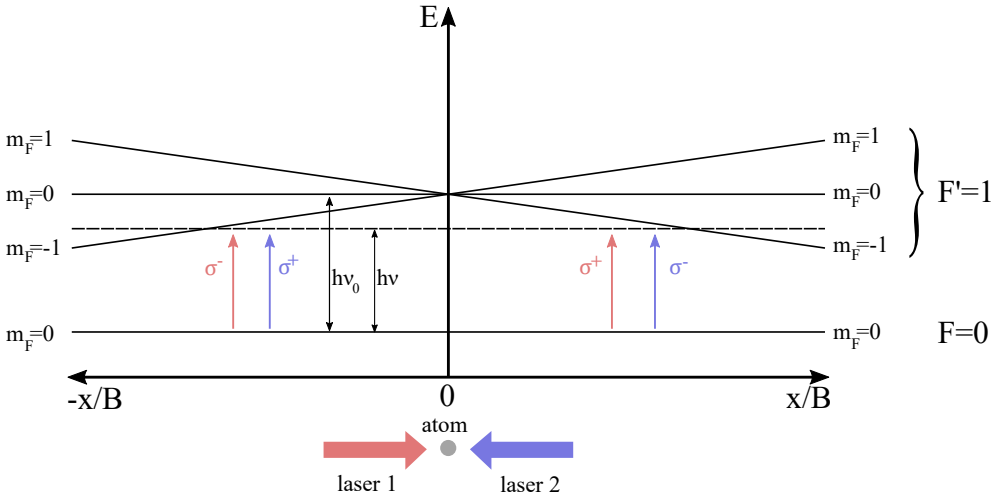

Figure 2.9: Energy levels involved in 1D MOT scheme when driving the transition $F = 0 \rightarrow F' = 1$. The dashed horizontal line represents the energy of the red detuned laser of frequency ν, while the energy level at $h\nu_0$ is the transition's resonance frequency, ν_0. If an atom moves in the $-x$ direction the energy splitting of the excited state and increasing B-field bring laser 1 closer to resonance, causing an increased force from laser 1 pushing the atom back towards the origin and visa versa for an atom moving in the $+x$ direction.

2.4.3 Grating Magneto-Optical Traps

Since the invention of the 6-beam MOT several other optical geometries have been demonstrated,[31–36] the most common of which are highlighted in Figure 2.10.

The geometry of particular interest in this work is the grating magneto-optical trap (GMOT),[34,37–39] used in all the cold-atom experiments discussed herein. This configuration makes use of the fact that the minimum number of MOT beams

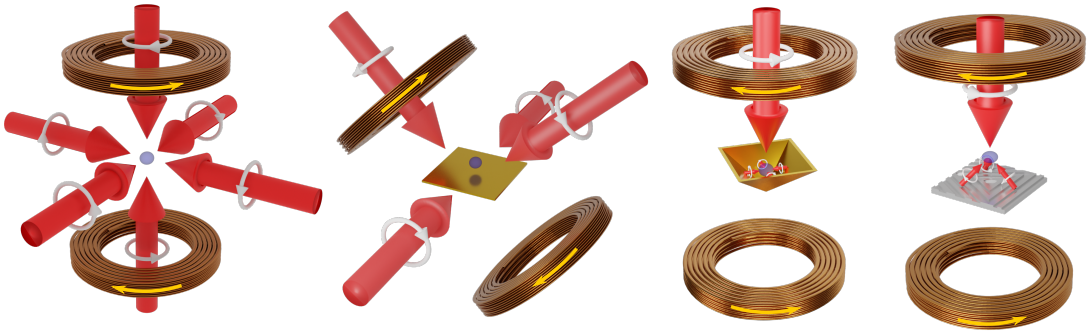

Figure 2.10: Comparison of different laser cooling geometries indicating cooling beam and trapping coil configurations. Left to right: 6-beam MOT, Mirror MOT, Pyramid MOT, GMOT. White arrows indicate light polarisation handedness. Orange arrows indicate direction of current flow in MOT coils.

required to trap in N dimensions is in fact $N+1$,[33,40] as opposed to the $2N$ of the original laser cooling schemes.[25,26]

GMOTs operate with a very similar arrangement to the tetrahedral MOT,[33] replacing the free space optics of the four beams with a single trapping beam incident on a microfabricated grating structure patterned on a silicon chip. The first order diffracted beams from the grating chip allow the balance of radiation pressure from the input beam for laser cooling in three dimensions. This concept is illustrated in two dimensions in Figure 2.11(a). The optimum balance in radiation pressure from n diffracted beams is found when the first order diffraction efficiency, η, is[41]

$$\eta = \frac{1}{n}. \tag{2.25}$$

Several different GMOT geometries have been demonstrated, including tri-segment gratings, quad-segment gratings, and checkerboard gratings.[34] More details on the working principle of GMOTs can be found in Ref[42] while details on grating design and MOT characterisation are found in Ref.[43] Throughout this thesis various gratings have been used, all of which utilised the tri-segment geometry as shown in Figure 2.11(b). These tri gratings have grating regions of 20×20 mm which are broken into three distinct sections of binary patterned grating structures. This arrangement ensures that a cooling force can be applied in three dimensions for atom trapping.

The primary benefit to using a GMOT is the compact form factor achievable when compared to traditional 6-beam MOTs or even mirror MOTs. This is of

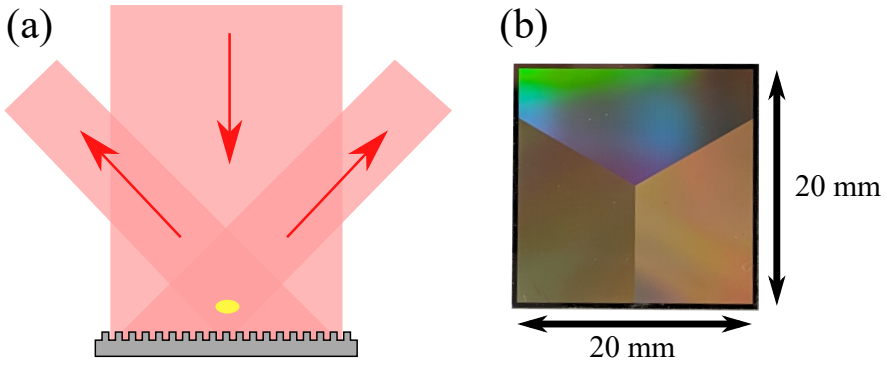

Figure 2.11: (a) Schematic of GMOT cooling geometry, shown in two dimensions. Darker red diamond shaped region indicates the cooling overlap volume where atoms can be trapped and cooled into the MOT (shown in yellow). (b) Image of typical "tri-grating" as used throughout this thesis, three grating regions are clearly visible.

particular interest for compact cold-atom sensors, the development of which is the focus of this thesis. By using a single cooling beam the number of optics can be reduced drastically while maintaining high trapped atom numbers at low temperatures. This has the additional benefit of simplifying optical alignment as only a single beam is utilised. A simplified alignment procedure may also prove beneficial when taking devices out of the lab with the fewer beam paths improving device robustness. MOTs of $\sim 6 \times 10^7$ atoms have been demonstrated (recently improved to 1×10^9 by loading from a $2D^+$ MOT[44]),[34] with temperatures as low as 3 μK.[39] In recent years GMOT technology has also been extended to the alkaline earths, namely strontium.[45–47] Working with strontium adds significant complexity to the design of the grating chips due to the multi-wavelength cooling strategies required to reach atomic temperatures in the μK regime. Despite the additional complexity of the grating design, these works help set the foundations for more simplified and compact strontium optical clocks. As these types of clock currently exhibit the lowest systematic uncertainties of any clock,[7] they are an appealing line of inquiry towards more compact optical standards.

2.4.4 Doppler Limit

During the first rigorous investigations into the laser cooling of neutral atoms, researchers were surprised to observe sodium atoms cooled to 40 μK, significantly below the so-called "Doppler Limit",[25,48] the theoretical minimum temperature achievable by the radiative scattering force detailed above.

The origins of this limit lie in the stochastic nature of absorbed and emitted photons from the atom giving some heating rate arising from the random walk of the atom. This heating rate is balanced against the cooling force, which given the approximation $|kv| << \Gamma$ and $|kv| << |\Delta|$ gives[30]

$$T_D = \frac{\hbar\Gamma}{4k_B}\frac{1 + I_T/I_S + (\frac{2\Delta}{\Gamma})^2}{-2\Delta/\Gamma}. \tag{2.26}$$

In the low intensity limit and substituting $\Delta = \Gamma/2$ this expression is simplified to:

$$T_D = \frac{\hbar\Gamma}{2k_B}. \tag{2.27}$$

For sodium this corresponds to a Doppler limit of 240 μK (a Doppler limit of 145 μK is expected for ^{87}Rb). After significant work verifying the result,[25,26] new theories considering multiple energy levels of the atom were proposed to explain this rare case of experiment outperforming theory. One convenient and widely used explanation of sub-Doppler cooling is known as polarisation gradient cooling, or Sisyphus cooling.[28,29,49]

2.4.5 Sisyphus Cooling

Two counter-propagating, linearly polarised red detuned ($\Delta < 0$) laser beams with orthogonal polarisation vectors (Lin$\perp$Lin) are considered. The interference of the two beams creates a standing polarisation wave that varies between right hand circular (σ^+), linear and left hand circular (σ^-) over a distance $\lambda/2$, shown in Figure 2.12. An atom with a ground state $J = 1/2$ and excited state $J' = J+1 = 3/2$ moving through this potential will experience a polarisation dependent AC Stark shift of its m_J sublevels,[13,29]

$$\Delta_{AC-Stark} = \frac{\Omega^2}{4\Delta} = \frac{\Gamma^2}{8\Delta}\frac{I}{I_{sat}}, \tag{2.28}$$

where Ω is the Rabi frequency and I_{sat} is the saturation intensity for the given transition at a particular polarisation. In the case of σ^+ light this shifts the $m_J = 1/2$ ground state more than the $m_J = -1/2$, with the converse being true for σ^- light.

As an atom climbs the polarisation gradient, kinetic energy is converted into potential energy. When it nears the top of the hill it is more likely to undergo a transition to the excited state, driving $\Delta m_J = +1$ ($\Delta m_J = -1$) transitions in a

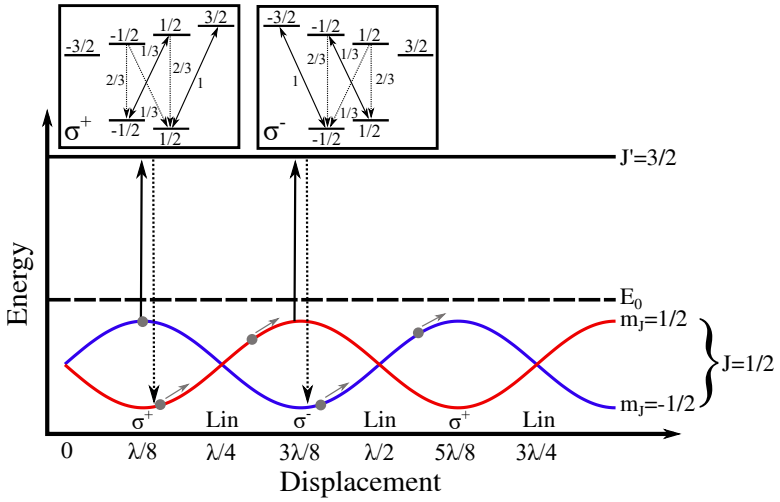

Figure 2.12: Sisyphus cooling mechanism in 1D for counter-propagating Lin⊥Lin polarised light. Dashed line indicates the un-shifted ground state energy level. Red (Blue) line shows AC Stark shifted energy level of the $m_J = +1/2$ ($m_J = -1/2$) energy level. Inset boxes: optical pumping scheme for σ^+ and σ^- light. Numbers indicate the relative probability of decaying from the excited state into a given ground state sublevel.[49]

region of σ^+ (σ^-) polarisation. This absorbed photon is then emitted after a time in the excited state $\approx 1/\Gamma$ with the atom having a higher probability of decaying into the most AC Stark shifted, and therefore lowest in energy, state due to optical pumping and the square of the Clebsch-Gordan coefficient of each transition (see Figure 2.12 insets). The difference in energy between the two ground states is carried away by the spontaneously emitted photon, causing a net reduction in the atom's kinetic energy over repeated cycles through the polarisation gradient.

The minimum temperature achievable with optical molasses is limited by the energy shift of the two ground states,

$$T_{min} \propto \frac{I}{\Delta}, \tag{2.29}$$

suggesting that as $\Delta \to \infty$ or $I \to 0$, $T_{min} \to 0$. This is not the case as Sisyphus cooling can no longer remove energy from the system when the loss in energy from the cooling mechanism is equal to the recoil energy from spontaneous emission. This leads to a new theoretical minimum temperature, known as the recoil limit where the atomic velocity is equal to the recoil velocity:

$$k_B T_{recoil} = \frac{\hbar^2 k^2}{m} = 2E_{recoil}, \tag{2.30}$$

where m is the atomic mass and E_{recoil} is the recoil energy. For ^{87}Rb this corresponds to a recoil limited temperature of 362 nK. Experimentally, temperatures $>1\mu$K are commonly achieved.

While convenient and widely used to explain sub-Doppler cooling, real atoms cannot be explained fully by this rather simplified system. In addition, expansion of this explanation to three dimensions remains complex and well outwith the scope of this thesis due to the complexity of multiple fields driving transitions defined by different quantisation axes. The Sisyphus cooling mechanism does however remain the most widespread explanation of laser cooling, offering good insight into the processes of sub-Doppler cooling.

2.4.6 Grey Molasses

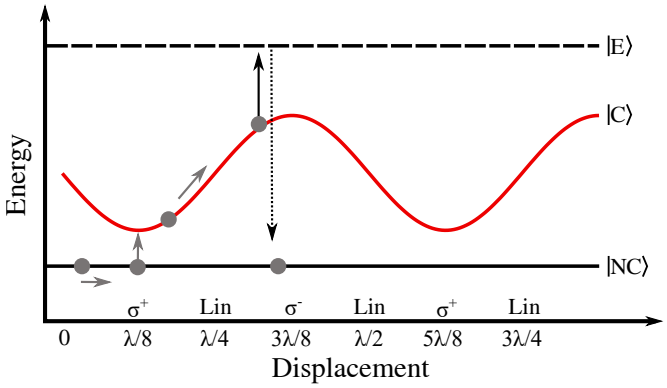

Figure 2.13: Grey molasses cooling mechanism. Moving atom (grey circle) is motionally coupled from $|NC\rangle$ (solid black line) to $|C\rangle$ (red line) from here it can be excited to $|E\rangle$ (dashed black line) from which it can decay back into lowest energy state, $|NC\rangle$.

Grey molasses cooling is functionally very similar to Sisyphus cooling, enhanced by an additional "dark state" where cold atoms can collect. While in this dark state the atomic scattering rate is much reduced, hence the name grey molasses as it is neither totally bright nor totally dark. Due to the reduced scattering rate, the atom heating rate is also much reduced, consequentially reducing the atomic temperature.

In addition to lower temperatures, the phase space density (PSD), defined as

$$PSD = n\lambda_{dB}^3 = n\left(\frac{h}{\sqrt{2\pi m k_B T}}\right), \tag{2.31}$$

where n is the atomic density and λ_{dB} is the de Broglie wavelength, is often much higher than that of traditional red molasses.[50,51] Atomic density here is given by[52]

$$n = \frac{N}{(2\pi)^{3/2}\sigma^3}, \tag{2.32}$$

with N being the trapped atom number and σ the standard deviation of the cloud's Gaussian width. This increased PSD is largely due to the reduced scattering rate causing lower inter-atomic repulsive forces, allowing the atomic density to increase without increasing temperature.[53]

The details of the dark state formation are beyond the scope of this work and therefore will not be detailed here. In brief, this state comes about when two coherent light fields couple three electronic states of an atom, causing a superposition of the ground states that it decoupled from either of the fields. This effect is known as coherent population trapping, more details of which can be found in Ref.[43]

Taking the same counterpropagating Lin⊥Lin beam configuration from above, this time with *blue* detuned ($\Delta > 0$) light. We now have a configuration giving a non-coupling state, $|NC\rangle$, lower in energy than the coupling, $|C\rangle$, state. As before $|C\rangle$ varies spatially due to a spatially varying AC Stark shift.

The phase of a slowly moving atom in $|NC\rangle$ can adiabatically adjust to the changing polarisation, however if the atom moves with some larger velocity it is motionally coupled to $|C\rangle$. It can be shown that this motional transfer is most likely at the bottom of the light-shifted potential of $|C\rangle$.[54] From here the atom begins to climb the potential gradient before being excited to the upper energy state $|E\rangle$. As with Sisyphus cooling, spontaneous emission then carries away some of the atom's kinetic energy and it can decay back down to $|NC\rangle$. This process is repeated until almost all the atoms are pumped to the dark state where the heating is minimal.

Chapter 3

Preparation of Cold Atoms

Several different experimental set-ups were used to carry out the work detailed in this thesis, as multiple descriptions of very similar set-ups would become tedious for both the reader and writer, a general description of the creation of cold atoms is included here. Experiment-specific details are included in the following chapters where necessary.

3.1 Experimental Set-up

3.1.1 Optical Requirements

When setting up a cold-atom experiment one of the first considerations is the trapping laser. Ref[55] contains a useful table of many of the requirements of laser cooling, including those needed from the laser. Firstly, the laser should exhibit a linewidth lower than the natural linewidth of the transition, Γ ($\Gamma = 2\pi \times 6$ MHz for ^{87}Rb[14]). Several different lasers were used throughout the course of this work: homebuilt[56] and commercial extended cavity diode lasers (ECDLs), a volume Bragg grating (VBG) and a frequency doubled telecomms laser. The choice of laser for a specific lab-based experiment is primarily a function of how much optical power is required (assuming the laser meets the linewidth and frequency stability requirements). The more complicated experiments involving multiple beam paths such as the clock investigation in Chapter 6-7 require more power from the laser which helps inform the decision.

Saturated absorption spectroscopy[57] was used to stabilise both the ECDL and VBG. This technique (explained in detail in Ref[43]) is relatively simple to set up and provides a sufficiently good frequency stability for the purpose of

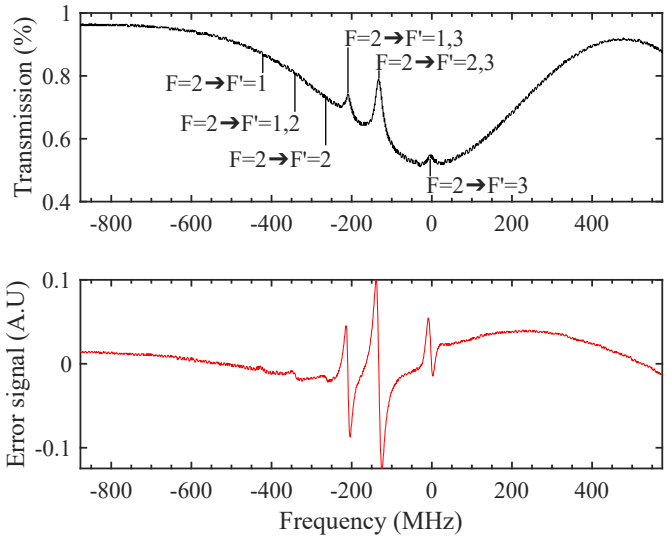

Figure 3.1: Top: Saturated absorption spectroscopy of ^{87}Rb $F = 2 \rightarrow F'$. Bottom: Demodulated saturated absorption spectroscopy error signal.

these experiments. In general, locking to the atomic line via saturated absorption spectroscopy was accomplished by modulating the current driving the laser, the demodulated signal providing the feedback lock point. While modulation of the laser frequency is acceptable for the investigations presented in Chapter 4, any laser frequency modulation during the clock investigations of Chapter 6 is undesirable. In this case, the atomic spectrum itself is modulated via the first order Zeeman effect. This is accomplished by modulating the linear magnetic bias field provided by a solenoid, wrapped around the atomic reference cell. An example saturated absorption spectrum, obtained by Zeeman modulating the atomic spectrum, with a demodulated error signal is presented in Figure 3.1.

A commercial Muquans ILS780 laser was used for the results collected in Chapter 5-7. This system operates with a master laser locked to a transition in ^{85}Rb via saturated absorption spectroscopy with a slave laser offset locked from the master.[58] Offset locking is achieved by measuring the frequency difference between the master and slave laser via an optical beat note. The frequency of the beat note, and therefore slave laser frequency, is then stabilised to an external frequency reference.[59] This reference is provided by the user and facilitates dynamic control of the laser frequency. Offset locking in this manner makes the slave laser very agile, capable of performing frequency jumps from a previous lock point of up to 1 GHz in <600 μs, a very useful attribute during the grey molasses investigation (see Sec 3.5). A commercial Moglabs EDCL laser with a built-in

tapered amplifier (TA) was used to create the 3D optical lattices described in Chapter 5. Finally, a ytterbium fibre laser operating at 1070 nm was used for the 1D lattice also presented in Chapter 5. A look-up table summarising the different lasers and their use cases is presented in Table 3.1 for convenience.

Laser	Use Case	Thesis chapter/ Section	Wavelength (nm)	Linewidth	Max Power	Locking method
Home built ECDL 1	MOT, Red molasses	6	780.24	$\approx$ 0.6 MHz	1 W	Sat Spec
Home built ECDL 2	Hyperfine repump painting	4.2	780.24	$\approx$ 0.6 MHz	60 mW	Sat Spec
VBG	MOT	4.1	780.24	$\approx$1 MHz	150 mW	Sat Spec
Muquans ILS780	MOT, Red/Grey molasses	3.5, 5, 6, 7	780.24	<0.05 MHz[58]	600 mW	Internal offset
Moglabs ECDL +TA	3D lattice	5	780.24$\pm$0.16	$<$ 0.1 MHz[60]	1.7 W	Free running
Ytterbium	1D lattice	5	1070	1.5 nm[61]	15 W	Free running

Table 3.1: Table of lasers used throughout thesis.

To laser cool ^{87}Rb, the D_2 $F = 2 \rightarrow F' = 3$ cycling transition is driven. While selection rules forbid decay into the $F = 1$ ground state, off-resonant scattering means the $F = 2 \rightarrow F' = 2$ transition can simultaneously be driven (at a much lower rate), allowing decay into the $F = 1$ ground state where eventually all the atoms are shelved and lost to the cooling process. A second "repumping frequency" is therefore introduced, driving the $F = 1 \rightarrow F' = 2$ transition and recycling shelved atoms back into the cooling cycle. Unless otherwise stated, in the following chapters repump light was derived from an electro-optic modulator (EOM) that places frequency sidebands at $\pm f_{\text{Drive}}$ on the carrier frequency. Only one of the created frequency sidebands is required for repumping the atoms, the other unused sideband being sufficiently detuned from resonance as to be neglected. While performing a standard MOT and red molasses sequence $f_{\text{drive}} =$ 6.57 GHz (see Figure 2.7). Repumping cannot be performed by setting $f_{\text{drive}} =$ 6.83 GHz during standard MOT and red molasses cooling as this frequency would address the $F = 1 \rightarrow F' = 3$ transition, forbidden due to selection rules.

The amount of light in each sidband can be quantified with a Fabry-Perot cavity and is often expressed as a percentage of the total power. The sideband amplitude can be controlled by the RF drive power applied to the device. In the case of large RF drive powers, 2nd order sidebands at $\pm 2 \times f_{Drive}$ will also appear in the frequency spectrum. For the creation of MOTs a sideband amplitude of $\approx$5% is sufficient.[55] An example plot of the sideband amplitude with respect to the total power is shown in Figure 3.2 as a function of the RF drive power.

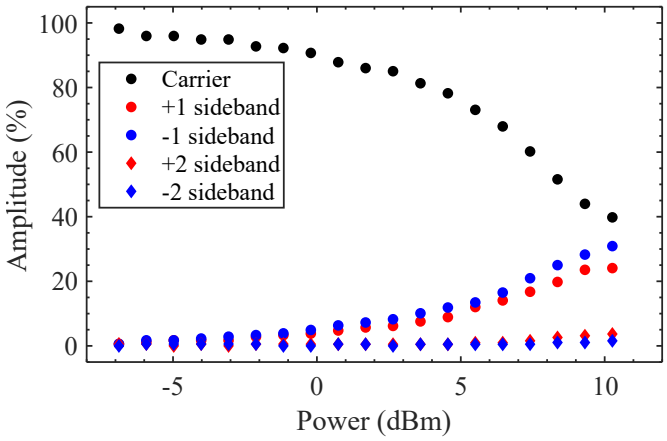

Figure 3.2: EOM generated frequency sideband amplitude with respect to the total power. These data were taken using the Muquans laser with its inbuilt EOM.

In terms of total optical power, typically >30 mW is required to trap $> 10^6$ atoms in a GMOT.[55] Dynamic power control for an optical molasses stage is achieved using double-pass acousto-optic modulators (AOM).[62] Arbitrary optical power ramps can be created by modulating the AOM RF drive power. Beam shuttering can also be achieved using AOMs when necessary, i.e. during a clock sequence. Similarly, the light frequency can be dynamically controlled in the experimental cycle when required using AOMs.

One final optical requirement for laser cooling that is especially important to the GMOT configuration is the cooling beam profile. In order to get good cooling the radiation pressure from each cooling beam must be well-balanced.[41] When illuminating the grating chip with Gaussian beams this can become problematic as low intensity light from the extremes of the Gaussian profile is diffracted up to balance the radiation pressure at the top of the overlap volume, derived from the high intensity centre of the beam (see Figure 2.11). This imbalance in forces reduces the effective overlap volume (V) of the GMOT, reducing the maximal trapped atom number, N, through the relation[34]

$$N \propto V^{1.2}. \tag{3.1}$$

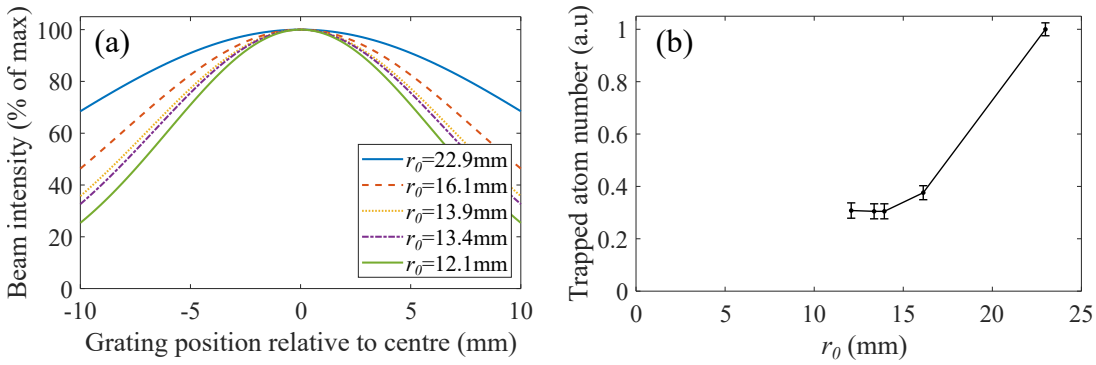

Figure 3.3: (a) Gaussian beam intensity profile across grating chip surface, plotted for different $1/e^2$ radii. (b) Normalised maximum trapped atom number as a function of trap beam $1/e^2$ radius. A solid line is added to help guide the eye.

While this effect has been recognised since the first demonstrations of GMOTs[37] it has been quantified here by measuring the maximum trapped atom number for different $1/e^2$ beam radii (r_0), incident on a 20×20 mm^2 grating chip. To change r_0 (and therefore the intensity gradient across the grating surface) the trapping beam was expanded from a fibre in a test set-up and collimated using different

focal length lenses. The peak trap light intensity was kept constant across the data set to ensure a fair comparison and the maximum trapped atom number recorded. These data are presented in Figure 3.3. It was found that as r_0 becomes smaller than the dimensions of the grating chip the maximum trapped atom number drops off sharply. This study and the data presented in Figure 3.3(b) reinforces that for the highest trapped atom number in a GMOT a low intensity gradient across the trapping beam is desirable, independently demonstrated in Ref.[63] This can be achieved with commercial "flat-top" beam shapers or simply by overexpanding and clipping the beam as is the case here. While easy and effective, overexpanding the beam does waste a significant portion of the available optical power, something that must be considered when developing low size weight and power (SWaP) systems.

3.1.2 Magnetic Field Generation for Trapping

The generation of a quadrupole magnetic field for the MOT is accomplished by a pair of circular coils (labelled Coil_1 and Coil_2 in the following), of radius R with n_t number of turns. In the ideal anti-Helmholtz configuration current (i) is run in opposite directions through the two coils which are separated by a distance $R/2$. The magnetic field generated by the coil pair is calculated by the Biot-Savart law and results in the magnetic field shown in Figure 3.4(a).

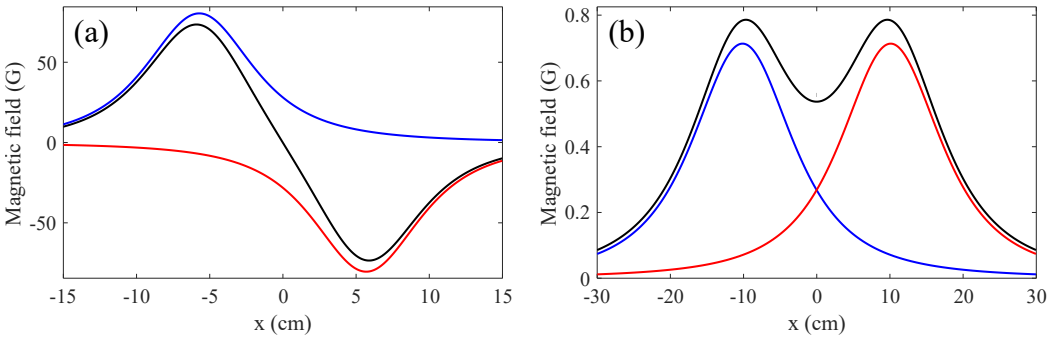

Figure 3.4: Magnetic fields for trapping and cooling. Red: Coil_1, Blue: Coil_2, Black: Total field. (a) Quadrupole magnetic field from anti-Helmholtz pair. i=5.5 A, n_t=132, R=5 cm. (b) DC magnetic field from Helmholtz pair. i=0.4 A, n_t=30, R=10 cm.

Similarly, a DC magnetic field can be produced with the same geometry by flipping the polarity of one of the coils to produce a Helmholtz coil pair. These additional coils must be included in each geometric axis in order to cancel out

both the earth's magnetic field (< 1 G) and any stray fields present in the lab. Without careful cancellation of the magnetic field it is not possible to reach sub-Doppler temperatures. Figure 3.4(b) shows the field generated by a Helmholtz coil pair. These additional coils are also used in Chapter 6-7 to create a small bias field to lift the atomic degeneracy.

3.1.3 Vacuum Requirements

Laser cooling is only achievable in very low-pressure environments due to thermal background collisions ejecting atoms from any trap. To that end, several different vacuum chambers have been used or built during the course of this work. The low pressures required ($\leq 10^{-7}$ mbar[55]) necessitate careful construction of these chambers to reduce both outgassing of materials within the chamber and the leaking of gases into the chamber.

One gas species of particular concern is helium (He). Due to its low atomic cross section and relatively high natural atmospheric abundance of 5ppm[64] He naturally migrates into these chambers over time, requiring constant active pumping by an ion pump. These pumps typically have quite a large SWaP budget and are one of the major limitations to making truly compact field-deployable cold-atom sensors (discussed in detail in Chapter 4). In addition to this they contain permanent magnets which can cause magnetic field gradients, a major problem when working with cold atoms. To minimise these gradients the ion pump must either be placed a reasonable distance from where the MOT forms or be magnetically shielded with mu-metal to levels low enough to be cancelled by the Helmholtz shim coils.

After all the components have been assembled for the desired chamber geometry they are cleaned in an ultra-sonic bath, firstly in acetone and then in methanol or isopropyl alcohol. Optionally, the components can also first be cleaned in a de-greasing detergent, effective at removing layers of oil deposited on the components. This step can be beneficial when re-purposing parts from previous vacuum chambers where the cleanliness of the parts is not guaranteed

Once clean, the various components are connected together via ConFlat flanges and copper gaskets to provide a seal capable of maintaining ultra-high vacuum (UHV). The chamber is then connected to a pumping station consisting of a roughing pump to reduce the pressure from atmospheric pressure to $< 10^{-2}$ mbar. Once the pressure has been reduced to this level a turbo pump can engage, bring-

ing the chamber down to UHV over time. The chamber can be leak checked with helium and a residual gas analyser or simply by depositing a small amount of isopropyl alcohol onto each of the joints in turn and monitoring the pressure measured in the system.

To aid the process of outgassing the internal walls of the chamber, along with increasing the diffusion of contaminants out of the bulk material, the temperature of the whole system is elevated to ≈100 °C. The whole system, including the ion pump, is then baked for at least a day. At these elevated temperatures much of the contaminants on the chamber walls are able to evaporate off before being pumped away by the turbo pump. This process predominantly reduces the amount of water molecules on the surface of the walls, though longer bakes do help reduce the hydrogen content dissolved in the metallic crystalline structure if lower pressures are required. While still at elevated temperatures the ion pump is turned on, this helps de-gas any contaminants deposited on the ion pump itself which are then removed from the system by the turbo pump. Rubidium is sourced from commercial SAES alkali dispensers[65] which are turned on at this stage to remove their passivisation layer and de-gas them. Finally, the temperature is brought back down and the pumping station is isolated from the chamber by a gate valve and disconnected.

3.2 Atom Detection

3.2.1 Fluorescence Detection

Photodiode detection

The simplest method of atom detection is by collecting atomic fluorescence onto a photodiode, using the trapping light tuned near to resonance to drive the atomic transition and generate fluorescence. Photodiodes have the advantage of being experimentally much more compact and simple to operate compared to a camera. The measured photodiode voltage is related to the trapped atom number by considering the current measured by the photodiode (i), detection efficiency (as specified by the photodiode manufacturer), η ($\eta = i/W$, where W is the optical power), photon scattering rate (R_{sc}), the energy per photon ($E = hc/\lambda$) and the solid angle of the imaging system ($\Omega_d = \frac{\pi}{4}\left(\frac{f}{f_\# d_0}\right)^2$[14]). Here f is the focal length of the imaging system, d_0 is the distance to the object and $f_\#$ is the imaging system f-number. The inclusion of Ω_d describes how many photons, assumed to

be emitted isotropically, are collected by the imaging system. Finally, this leads to an expression for the atom number given by

$$N = \frac{4\pi}{\Omega_d}\frac{\lambda}{hc}\frac{i}{R_{sc}\eta}. \tag{3.2}$$

An experimental MOT "rise curve" showing the measured fluorescence as a function of load time is shown in Figure 3.5. In addition to indicating the trapped atom number, these rise curves can also give an extremely useful measure of the vacuum pressure, measured at the atom location.[66,67] This provides a very useful diagnostic tool for cold-atom systems as ion pump pressure readings are notoriously unreliable without calibration and only indicate the pressure at the pump, often very different to what the atom cloud experiences. This pressure reading is calculated by first fitting a damped exponential to the rise curve of form:

$$V(t) = V_0(1 - e^{-t/\tau}) + C. \tag{3.3}$$

Here V_0 is the amplitude, τ is the loading time constant and C is a vertical offset to account for background light picked up by the photodiode. Arpornthip *et al.* find that the time constant is then related to pressure by $P = 2.67 \times 10^{-8}$ mbar$/\tau$.[66] This empirical calibration factor was found to be valid within a factor of two over a wide range of trap parameters and background gas composition, extending to pressures $< 1 \times 10^{-9}$ mbar.[66]

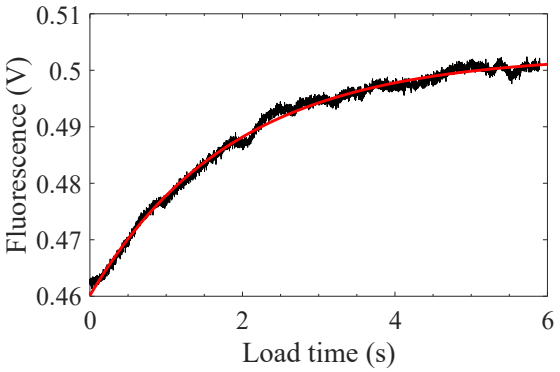

Figure 3.5: Fluorescence rise curve as atoms are loaded into the GMOT. Red curve shows a fit to the data of form Eq.3.3 with fit parameters V_0=0.043 V, $\tau = 1.86$ s, C =0.46 V.

Camera imaging

When imaging the MOT in fluorescence onto a camera, two images are taken; one with the atom cloud present and a second image after it has dispersed. Subtracting the second image from the first leads to a final background-subtracted image that can then be analysed.

GMOTs typically form ≈5 mm from the surface of the grating, in some situations such as the lattice experiment described in Chapter 5 and the chip-scale vacuum cell described in Sec 4.1, scattered light can cause difficulties with high contrast fluorescence imaging, saturating regions of the sensor. To ameliorate this effect, a spatially selective focal imaging system, shown in Figure 3.6, was employed during these investigations. Light not originating from the imaging plane of L_1 is largely filtered out by Iris_1 while light originating from the MOT is focused through Iris_1 and thus able to pass through without clipping. An optional non-polarising beam splitter (NPBS) and photodiode was used for the results collected in Sec 4.1, allowing MOT rise curves and vacuum pressure to be extracted simultaneously. The magnification of the imaging system is experimentally determined to account for imperfections in lens positioning by imaging a ruler and calculating the number of pixels/mm.

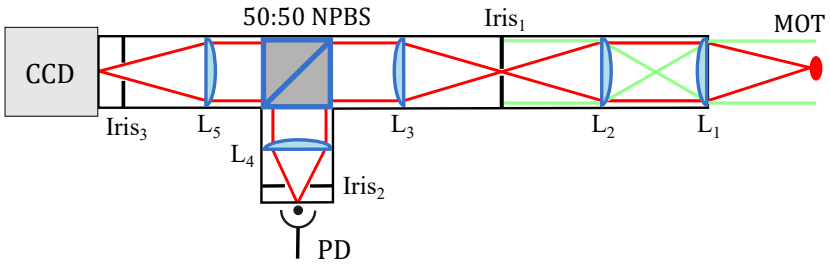

Figure 3.6: Schematic of the spatially selective focal plane fluorescence imaging system. Red ray trace indicates light emitted by the MOT. Green ray trace indicates background and scattered light.

Similarly to the photodiode method, the atom number as measured by a camera can be calculated by considering the total pixel counts (C), the camera exposure time (τ_{exp}), sensor quantum efficiency (η_{sensor}), R_{sc} and Ω_d. This leads to an atom number calculated by

$$N = \frac{4\pi}{\Omega_d} \frac{\Sigma C}{R_{\text{sc}} \tau_{\text{exp}} \eta_{\text{sensor}}}. \tag{3.4}$$

Generally, the imaged atomic clouds can be well described by a Gaussian distri-

bution in each Cartesian axis (practically only two are visible due to the single imaging axis):

$$C(x) = C_0 \ \exp\left[-\frac{(x-x_0)^2}{2\sigma^2}\right], \tag{3.5}$$

where C_0 is the peak pixel count, x_0 is the Gaussian peak centre point and σ is the cloud width. In most cases the atom number is calculated by integrating the final image in each axis, fitting Eq 3.5 and integrating this fit to find the total pixel count. This method assumes that the images of the atom cloud has been re-scaled to account for the magnification of the imaging system used.

3.2.2 Absorption Imaging

As photons from a low intensity, near resonant probe beam pass through an atom cloud of diameter x, the atoms absorb photons according to the Beer-Lambert law, $I(x) = I_0 e^{(-\alpha x)}$, with an absorption coefficient, α, dependent on atomic density. The shadow left in the probe beam from these absorbed photons therefore gives an indication as to the size and density distribution of the atom cloud.

To accurately detect the atom cloud three separate images are typically acquired: I_{atoms} (image of the probe beam with the atom cloud present), I_{beam} (image after allowing the atom cloud to fully disperse) and I_{BG} (image with the probe beam extinguished to assess the background pixel counts of the system). These three images can then be processed to give an image of the atom cloud in terms of optical depth using the following:

$$OD = -ln\left(\frac{I_{beam} - I_{BG}}{I_{atoms} - I_{BG}}\right). \tag{3.6}$$

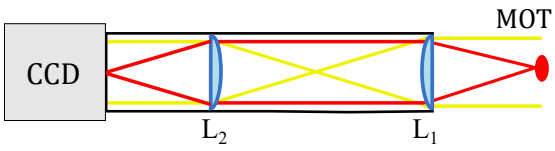

Figure 3.7: Schematic of absorption imaging system. Red ray trace indicates light emitted by the MOT. Yellow ray trace indicates the resonant probe beam.

A diagram of the optical system used for absorption imaging is shown in Figure 3.7. This basic 4f imaging system was used in the chip-scale vacuum cell investigation to image the atoms through a hole in the grating (see Sec. 4).

To calculate the number of trapped atoms the image is integrated in each axis and Eq 3.5 fitted. The atom number is then given by

$$N = \frac{A_{\text{pixel}}}{\sigma_L} \int OD, \tag{3.7}$$

where A_{pixel} is the area of a single pixel, and σ_L is the scattering cross section. As with the fluorescence imaging detailed above, this method requires the images to be re-scaled to account for the magnification of the imaging system so A_{pixel} is accurate.

3.3 Measuring Temperature

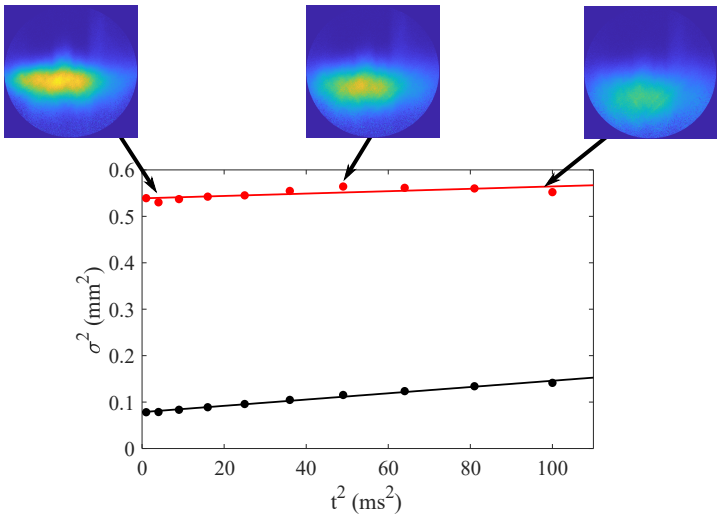

Figure 3.8: Time of flight plot. Red data: Cloud width parallel to the grating surface. Black data: Cloud width orthogonal to the grating surface. Insets show MOT image for a given drop time, taken through the sidehole in the microwave cavity experiment. Measured temperature is $T_{\parallel}$=3 μK, $T_{\perp}$=7 μK. Images shown with circular mask to remove scatter from sidehole aperture.

Atomic temperature is determined by the time of flight method (TOF). Here the trapping coils are turned off and the atom cloud is allowed to freely expand in the dark. Expansion of the cloud is tracked as a function of the drop time, t, by fitting Eq 3.5 and extracting the cloud width, σ. This is repeated over the course of several increasingly long time of flights, each given the index i. The expansion rate depends on the atomic velocity, thus temperature can be extracted by considering the Maxwell-Boltzmann distribution,

$$\sigma_i^2(t) = \sigma_{i-1}^2 + \frac{k_B T}{m} t^2, \tag{3.8}$$

where k_B is the Boltzmann constant, m the atomic mass and T the atomic temperature. Practically the extraction of temperature is achieved by plotting σ_i^2 vs t^2. Fitting the gradient of this line, $\frac{k_B T}{m}$, allows easy calculation of the temperature.

A TOF plot is shown in Figure 3.8 with linear fits applied to measure T. Care must be taken to tailor the chosen drop times depending on the temperature of the atoms. Initially during a molasses optimisation the cloud temperature is of order 1 mK, the typical temperature of a MOT. Short drop times are therefore necessary as the rate of expansion is high and the cloud quickly dissipates. Figure 3.8 shows the radial ($\parallel$) and axial ($\perp$) temperature to be slightly different. This is often the case due to the GMOT geometry where the cooling force is weaker in the axial direction, leading to a higher temperature in that axis by a factor of around two.[37]

3.4 Red Molasses

Several different experimental set-ups have been used throughout this work with subtly different timing sequences, each optimised for a given experiment. A typical sequence with red molasses cooling and TOF measurement is included for context here though the specific timing, detuning and intensity ramps are individually optimised for a given set-up.

After loading the MOT at maximum intensity with a detuning roughly -2Γ from the $F = 2 \rightarrow F' = 3$ transition, the trapping coils are turned off to initiate the molasses sequence. Γ here is the transition's natural linewidth of 6.07 MHz.[14] Typically a 10 ms molasses has been used. This is broken into two sub routines; first the carrier light frequency detuning is swept to be further red detuned from the cooling transition to -25Γ. Subsequently to this the light intensity is swept from the maximum trapping intensity to around $2I_{sat}$.

The EOM RF modulation frequency is kept constant at 6.57 GHz to allow the +1 frequency sideband to drive the $F = 1 \rightarrow F' = 2$ transition (see Figure 2.7). Once the red molasses sequence is finished the light is fully extinguished using an AOM and the atoms are allowed to ballistically expand in the dark. During TOF the light detuning is brought to resonance with the cooling transition, ready

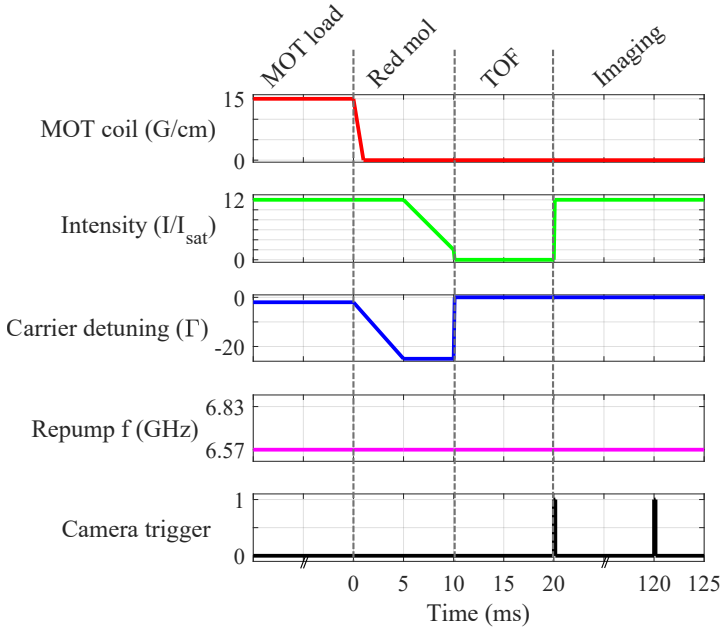

Figure 3.9: Typical experimental sequence for red molasses cooling. Carrier detuning is given with respect to the $F = 2 \rightarrow F' = 3$ transition in terms of the natural linewidth of the transition. Sequence for fluorescence imaging using a camera is shown as this detection scheme was most commonly used.

for fluorescence imaging as discussed in Sec 3.2.1. The high intensity used for fluorescence imaging is largely due to the practicality of not requiring any additional intensity ramps after imaging and before a new experimental sequence is initiated. This sequence is shown in Figure 3.9. Rigorous characterisation of red molasses cooling of ^{87}Rb in GMOTs has previously been published in Refs[37,43] consequentially no data on the subject will be presented here. Temperatures of 10 μK with several million atoms were achieved in most cases during the experiments detailed in this thesis. This was slightly improved upon in the lattice experiment of Chapter 5 with 3 μK and $8{\times}10^6$ routinely measured.

3.5 Grey Molasses

The grey molasses cooling sequence begins in a similar manner. A shorter 6 ms red molasses stage (broken into two subroutines as before) is used here to precool the atoms to around 30μK before grey molasses. This was found to greatly increase the number of atoms retained during the grey molasses cooling. At the beginning of the grey molasses sequence the light detuning is jumped to around 5Γ blue detuned from the $F = 2 \rightarrow F' = 2$ transition (see Figure 2.7).

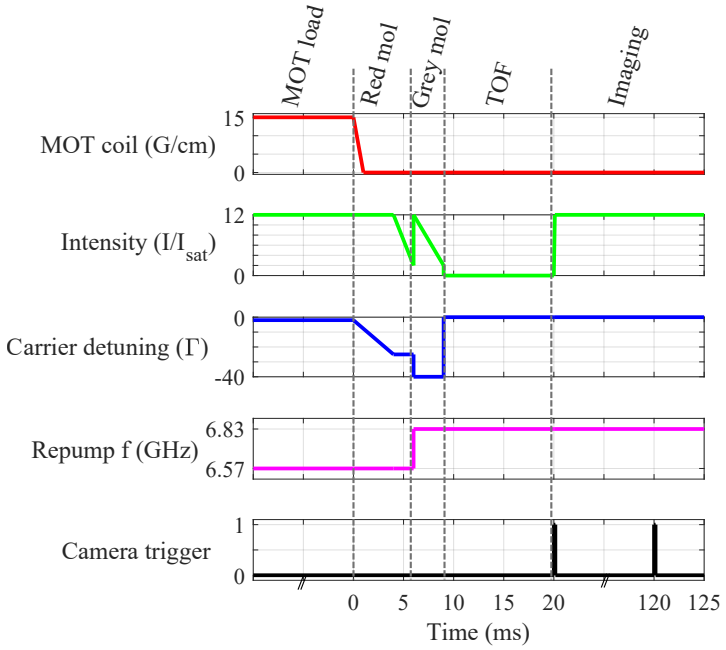

Figure 3.10: Typical experimental sequence for grey molasses cooling. Carrier detuning is given with respect to the $F = 2 \rightarrow F' = 3$ transition in terms of the natural linewidth of the transition. Sequence for fluorescence imaging using a camera is shown as this detection scheme was most commonly used.

Simultaneously the EOM drive frequency is changed to the ground state splitting of 6.834 GHz so as to drive the $F = 1 \rightarrow F' = 2$ transition (see Figure 2.7). The light intensity is then swept down in a similar manner as with red molasses before being extinguished for TOF measurements.

Grey molasses has been demonstrated to work in GMOTs with ^{7}Li[68] and ^{85}Rb,[69] to our knowledge no results on ^{87}Rb have thus far been presented. Some experimental optimisation curves are therefore included here.

The key metrics used in the optimisation of the grey molasses stage were the final temperature of the cloud and its phase space density (PSD), as given by Eq 2.31. PSD is a convenient metric as it takes into account both the density and temperature of the cloud with a higher PSD generally being desirable for laser cooling experiments. Error bars on all the following data represent the calculated standard deviation around the mean after repeating the experiment under the same conditions five times.

Similar to previous work in 6-beam MOTs and GMOTs we find a relatively short grey molasses sequence is sufficient to cool the atoms to a minimum temperature[51,68,70] and maximal PSD. From Figure 3.11 we see that past 3 ms no

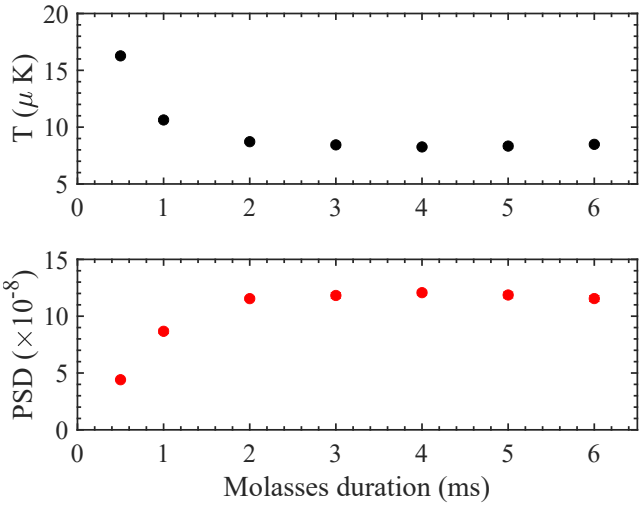

Figure 3.11: Grey molasses varying molasses duration. The error bars in this case are smaller than the size of the data points.

improvement in either metric is evident. 3 ms was therefore selected as the optimum molasses time.

A plot of T and PSD as a function of the one-photon detuning ($\Delta_{2,2}$) is shown in Figure 3.12. The best cooling is observed at $\Delta_{2,2} > 3.5\Gamma$ with a flat dependence past this point. This is somewhat lower than the $\geq 5\Gamma$ observed in 6-beam MOTs.[51] A slightly lower optimum detuning is consistent with the GMOT results presented by Barker *et al.*,[68] albeit in Li. A final one-photon detuning of $\Delta_{2,2} = 4\Gamma$ was selected to ensure the best cooling and highest PSD.

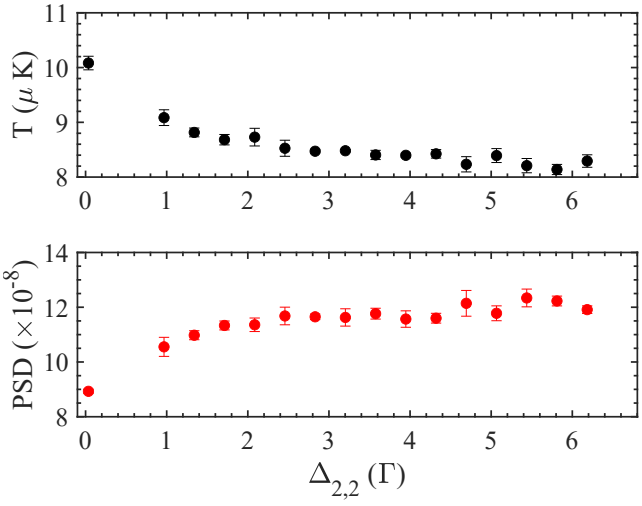

Figure 3.12: Grey molasses varying the one-photon carrier detuning. Detuning is given with respect to the $F = 2 \rightarrow F' = 2$ transition in terms of the natural linewidth.

Finally, the coherent repump frequency and amplitude is optimised using the EOM. Amplitude optimisation is shown in Figure 3.13, with an optimum T and PSD at a repumper amplitude of 25% the carrier. This is significantly higher than the optimum repump intensity quoted in Ref[51] for ^{87}Rb in a 6-beam MOT of around 10% the carrier intensity, the reasons for which are not well understood.

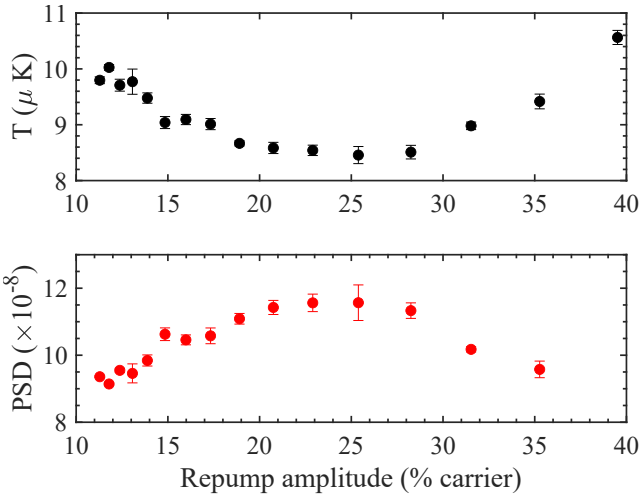

Figure 3.13: Grey molasses varying repump light amplitude. Amplitude is given with respect to the the carrier.

Repump frequency optimisation is shown in Figure 3.14. Repump detuning is defined such that $\delta_R = (f_R - f_{hfs})/\Gamma$ where f_R is the repump frequency and f_{hfs} is the hyperfine ground state splitting of 6834.68 MHz. In agreement with previous investigations of grey molasses in ^{87}Rb Ref[51,70] we find a small offset of the optimum two-photon detuning from the Raman condition ($\delta_R = 0$) of $\delta_R = -0.02\Gamma$. Curiously this offset was not observed or predicted by theoretical simulations of grey molasses cooling of Li in a GMOT.[68] This offset is not currently fully understood, though Ref[70] attributes it to light-shift effects.

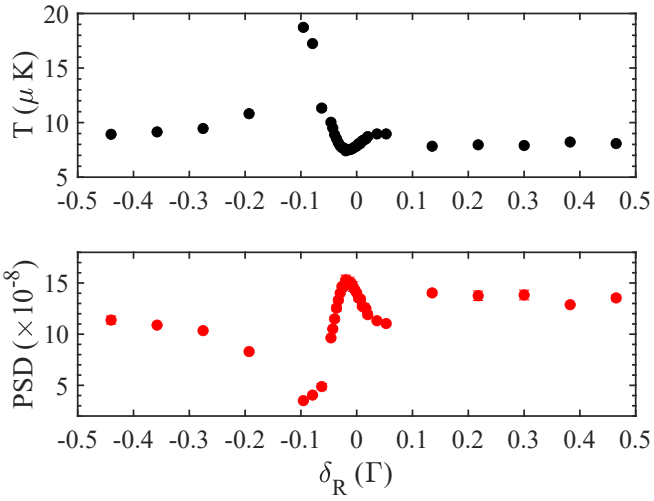

Figure 3.14: Grey molasses varying the two-photon repump detuning. δ_R is given in terms of the natural linewidth.

After optimising the grey molasses sequence and careful cancellation of all stray magnetic fields, an optimum final temperature of $T = (3.0 \pm 0.2)\mu$K and a phase space density of $PSD = (3.7 \pm 0.4) \times 10^{-7}$ is achieved (these data are not shown here).

Chapter 4

Microfabricated components for cold atom experiments

The development of atomic cooling has revolutionised precision measurements. The transition of these high performing cold-atom sensors out of the laboratory environment however remains largely elusive. In recent years, a large focus has been placed on micro-fabrication techniques to help with this transition.[31,55,63,71–73]

The crucial metrics of a successful sensor that is both portable and practical can largely be summarised by the size weight and power (SWaP) and ultimately the cost of the final device. This chapter covers two investigations into the use of microfabrication techniques to help reduce the SWaP budget of laser cooling experiments. The first half of the chapter covers work on a compact UHV vacuum chamber, constructed from silicon and glass bonded together using a micro-electromechanical system (MEMS) architecture. The second half of the chapter covers work using silicon MEMS scanning mirrors for the localised addressing of cold-atom clouds in a controllable fashion.

The entirety of this chapter is based on the published works of Ref[74] (Sec 4.1) and Ref[75] (Sec 4.2) with almost all the presented data also found in these publications. All experimental data was produced and analysed by the author. The chip-scale cell was designed and constructed by Dr James P. McGilligan while the optical set-up and integration of the cell into the cooling system was contributed to equally by the author and Dr James P. McGilligan. Theoretical analysis of the MOT overlap volume and expected trapped atom numbers were carried out by Dr Aidan Arnold with assistance from Dr James P. McGilligan. The MEMS scanning mirrors were designed and characterised by Dr Paul Janin and Dr Ralf

Bauer.

4.1 Chip-Scale Vacuum Cells

Since its first demonstration, laser cooling platforms have been pushed to ever more compact footprints. By utilising compact cooling geometries such as GMOTs or atom chips,[31,32,34] the optical requirements for laser cooling are no longer prohibitively large for portable applications. As a result, one of the main limiting factors to field-deployable cold atom sensors is now the vacuum chamber required to maintain the UHV pressures necessary for laser cooling.

In the past few years several groups have developed highly compact, portable vacuum chambers, with realisations now demonstrated in titanium,[76,77] ceramic,[78] and silicon MEMS cells.[79,80] Helium permeation rates through silicon and metal are low enough as to be neglected when considering helium permeation into the vacuum cell[71]. Steps must however be taken in these systems to carefully choose the viewport material such that helium permeation rates remain low, allowing operation under passive pumping alone for extended periods.[71] Both sapphire[77] and aluminosilicate glass[81] exhibit low helium permeation and are well suited to these applications. Vacuum cells made in titanium and ceramic have now demonstrated the conditions for atom trapping for 200[77] and 500[78] days respectively (at the time of publishing) via passive pumping with non-evaporable getters (NEGs) alone. Silicon based MEMS cell architectures however remain an enticing alternative in this field[55,71]

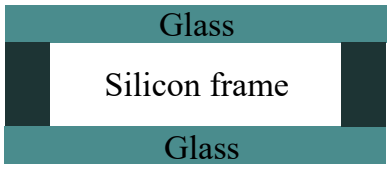

Figure 4.1: Side view of the basic MEMS cell architecture, showing the anodically bonded glass-silicon-glass stack. Aluminosilicate glass is used in the vacuum cell presented here due to its low helium permeation rate.

Due to the silicon chip industry many well understood and highly scalable foundry processes are available when working with silicon,[55] making them well suited to the potential mass production of cold-atom sensors. The basic architecture of an actively pumped silicon UHV vacuum cell was first demonstrated at NIST, consisting of a silicon frame with aluminosilicate glass anodically bonded

either side to provide optical access.[79] This basic architecture is shown in Figure 4.1. Subsequently to this, passive pumping by NEGs alone in a He permeable borosilicate cell was demonstrated to allow atom trapping for four days, an increase of almost five orders of magnitude when compared to the cell with no activated NEGs.[80] This architecture is also of particular interest because if combined with emerging integrated photonics the final physics package could feasibly be assembled autonomously simply by stacking components,[55,71] reducing cost and broadening the device market.

One major drawback to silicon MEMS-architecture cells is the difficulty of atom detection when used in conjunction with a GMOT. Silicon is opaque to 780 nm light, making atom detection orthogonal to the trap beam impossible, while the increased scatter from the grating surface also makes detection along the trap beam axis difficult. To overcome this, the first demonstration used a non-trivial two-photon spectroscopy scheme where the MOT was excited with 776 nm light to fluoresce at 420 nm, a band-pass filter in the detection system then allows the filtering out of any scattered cooling light revealing the MOT.[79] While effective, this scheme significantly increases the size of the system and exact knowledge of the atom number is difficult to extract due to the complexity of the two-photon excitation process.

To negate these limitations and simplify the set-ups required of MEMS-architecture cells when used with GMOTs, the feasibility of performing absorption imaging through a hole in the grating chip was investigated. While holes in the centre of grating chips have been used previously to reduce surface reflections,[82] as a source of cold-electrons[83] for Zeeman slowing[45,84] and to allow two-colour GMOTs for the trapping of alkali-earth elements[45,46] the impact of the hole on the attainable MOT number has not yet been quantified, this was investigated here. Finally the impact of the cell thickness on the GMOT optical overlap volume was investigated with a view to optimise this to allow a maximal trapped atom number in these systems while remaining scalable and compact.

4.1.1 Impact of Grating Hole

As a first step towards imaging through the grating hole, the effect the hole diameter has on the maximum trapped atom number was investigated. This was done in a standard cuvette-based vacuum cell, measuring atom number orthogonally to the trap beam with the fluorescence imaging system described in Sec.3.2.1.

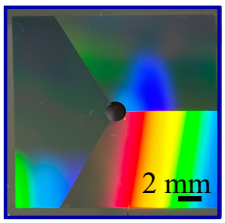

Figure 4.2: Image of grating chip with laser etched central hole. Figure adapted from Ref[75].

Five identical Tri-grating chips with central holes laser cut with diameters ranging from 1-5 mm (an example of which is shown in Figure 4.2) were fabricated for testing. For each subsequent measurement a grating was swapped into the system with identical experimental conditions. Some optimisation of the trap beam was performed for each chip to account for small variations in grating mount position.

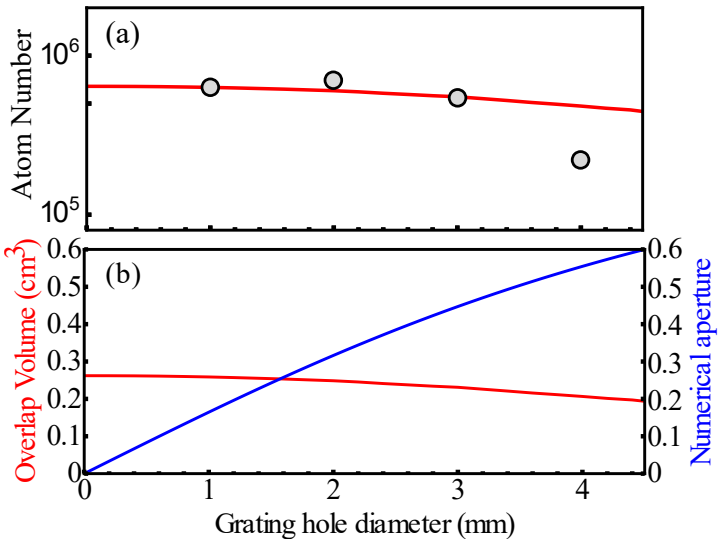

Figure 4.3: Critical parameters as a function of the grating centre hole diameter for an incident 2 cm beam diameter. (a): The measured atom number from orthogonal fluorescence imaging in the conventional glass cell. The measured error bars are smaller than the shown data points. The red curve shows $N \propto V^{1.2}$,[34] normalised to the first data point, for the overlap volume shown in (b). (b): Theoretically calculated optical overlap volume and numerical aperture from the grating chip assuming that the grating hole is the aperture stop of the imaging system. Figure reproduced from Ref.[74]

Results from this study are shown in Figure 4.3(a). The errorbars associated with all measured trapped atom numbers in the following chapter represent the standard deviation from the mean measured atom number after repeating the

same experiment around five times. It was found that as the hole diameter was increased up to 3 mm there was minimal impact on trapped atom number. In fact, hole diameters up to 2 mm indicated a slight improvement of the atom number. This is attributed to the minimal reduction in optical overlap volume and the reduced zeroth-order light from the grating interacting with the atoms. This light causes an imbalance in the optical intensities, causing a slight degradation in the atom number. Although steps are taken to minimise this zero-order light during the grating design process, up to around 5% still remains,[38] this study indicates that for a maximum trapped atom number it may be advantageous to have the addition of a central grating hole in some cases. Figure 4.3(b) emphasises the minimal impact grating holes up to 3 mm have on the optical overlap volume, while the improvements to the imaging system's numerical aperture are also clear. The theoretical optical overlap volume shown in Figure 4.3(b) is numerically integrated for a 2 cm beam diameter incident upon a 1100 nm period tri-segmented grating with a central hole of varying diameter. As the grating hole is increased beyond 3 mm the atom number decreases sharply, with no visible MOT for a hole of 5 mm diameter. The drop in atom number for increasing hole diameter is more severe than would be expected from the drop in overlap volume alone, likely due to the additional sensitivity of the radiation pressure balance from the chip. This is highlighted by the red curve in Figure 4.3, showing the overlap volume scaled to the atom number through the relation $N \propto V^{1.2}$,[34] normalised to the first experimental data point. As a trade off between a high imaging numerical aperture, useful for measuring low atom numbers, and an optimised trapped atom number a grating with a 3 mm hole was selected for the remainder of the study.

4.1.2 Through-Hole MOT Imaging

The simplified experimental set-up for the through-hole atom detection is shown in Figure.4.4. This set-up was built in a dedicated cooling platform that allowed the easy transition from a larger cuvette-based vacuum chamber for system characterisation to the chip-scale cell. The cooling system was based around a single volume-Bragg-grating laser (VBG) with frequency and intensity control provided by a double-pass AOM. An EOM provides repump light before the beam is fibre coupled, providing ≈30 mW of light at the atoms. This system allows for the trapping of up to 10^6 atoms in the standard cuvette vacuum chamber.

The chip-scale cell consisted of two 0.7 mm thick aluminosilicate glass wafers

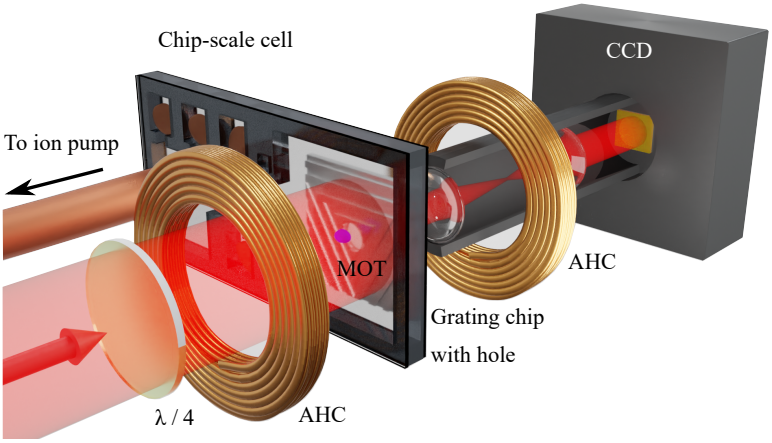

Figure 4.4: Simplified schematic of the through-grating hole absorption imaging set up. CCD: charge coupled device, AHC: anti-Helmholtz coils, $\lambda/4$: quarter wave plate. Figure adapted from Ref.[74]

anodically bonded in-house either side of a 3 mm thick silicon frame. The silicon frame was fabricated with a central square region of 25×25 mm^2 to allow good optical access to the 20×20 mm^2 grating chip. This first generation chip-scale cell at Strathclyde was actively pumped by an ion pump (though NEGs are included in the design for future passive pumping tests). A mechanically drilled 5 mm diameter hole was cut into one of the glass wafers before bonding, allowing a copper pinch-off tube to connect the ion pump to the cell. Rb was provided by a pair of SAES dispensers[65] outwith the cell, with the Rb migrating down the copper tube. A base vacuum pressure of 10^{-8} mbar as measured by the ion pump was recorded, this was later verified using MOT loading curves.

The through-hole imaging system is the same as that shown in Figure 3.7 using an objective lens of focal length 15 mm, placed directly behind the grating hole and an imaging lens with focal length 30 mm. Simultaneously to extracting the atom number with the through-hole imaging fluorescence measurements from MOT loading curves were also taken with the imaging system described in Figure 3.6 at an angle of 30° to the grating surface. These loading curves were used to verify the validity of the through-hole imaging and extract the vacuum pressure. An average ratio of calculated atom number of 1.6±0.4 was observed between the two methods, showing reasonable agreement. The complexities in aligning the camera at a position and angle such that the impact of surface scatter and diffracted beams from the grating are minimised however does not meet the needs of a simple mass-producible device.

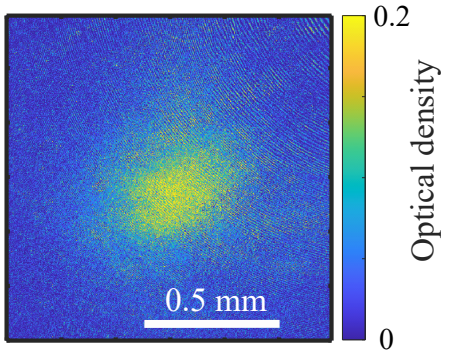

Figure 4.5: On-axis, through-hole absorption image of $\approx 2 \times 10^5$ atoms trapped in the chip-scale platform. Image taken with a 3 mm grating hole. Figure adapted from Ref.[74]

Atoms are loaded into the MOT in the usual manner, with a trap beam peak intensity of 8 mW/cm^2 for 500 ms. The relatively low peak intensity used here was limited by losses in the optical system and the comparatively low peak output power of the VBG laser used. The MOT coils are then turned off and the trapping beam intensity reduced to 115 μW/cm^2 and its frequency detuning brought to 0 MHz. Reducing the beam intensity and detuning serves the dual purpose of reducing image distortion due to diffraction effects within the atom cloud while also maximising the signal contrast. It is noted that the signal contrast was not improved by the addition of a static magnetic field along the imaging axis to aid the optical pumping of the atoms. A standard absorption imaging sequence (see Sec 3.2.2) with an exposure time of 25 μs is then performed and an image of the atom cloud extracted.

A saturation intensity of I_{sat}=1.67 mW/cm^2[14] was used in the calculation of trapped atom number for both imaging methods, consistent with previous works from our group.[34] This also gave a better agreement between the methods than when the saturation intensity averaged over all polarisations and magnetic sub-levels, I_{sat}=3.57 mW/cm^2[14] was used.

A saturation parameter, $S = \frac{I}{I_{\text{sat}}}$, sums over the intensities of the single input trap beam and the three diffracted beams from the grating, accounting for the total intensity the atoms experience. This modifies S to give $S = (1 + n\eta_1 \sec\theta)\frac{I_{im}}{I_{sat}} \approx \frac{2.4I_{im}}{I_{sat}}$, where I_{im} is the imaging light intensity, n is the number of diffracted first orders interacting with the atoms, η_1 is the efficiency of the first diffracted order, and θ is the angle of diffraction.[74]

4.1.3 Investigation of Reduced Atom Number

It was noted that the maximum trapped atom number in the chip-scale cell was an order of magnitude lower than that observed in the traditional glass cell with the same trapping parameters and grating chip. Consistent with previous measurements at a similar trap beam intensity,[37] the glass cell reached trapped atom numbers up to 10^6. To investigate the cause of the atom number degradation, the diameter of the trap beam, d, incident on the grating was varied using an iris in both the traditional glass cell and the chip-scale cell. This provides information on how the reduced vacuum volume overlap with the grating's optical overlap volume effects the trapping process. Results from this study are presented in Figure 4.6(a). A comparable background vapour density of approximately 3.1×10^6 cm^{-3} and total pressure of approximately 3×10^{-7} mbar was maintained in both vacuum systems. In all cases atomic density was calculated by measuring the relative absorption of a low intensity probe beam, scanned over the D_2 line resonance.

From Figure 4.6 we see the maximum atom number in the chip-scale cell is around 10^5. As d is reduced from the maximum 20 mm there is initially no change in the trapped atom number, down to a diameter of 17 mm. This can be understood since the majority of the optical overlap volume is actually outside of the cell at the higher beam diameters and therefore plays no part in the trapping of atoms. When d is reduced below 17 mm, however, the optical overlap volume contained within the vacuum volume is reduced, hence the degradation in the atom number. To emphasise this point, theoretical atom number as a function of d curves are also plotted. This atom number, N, is derived from the numerically integrated optical overlap volume, V, calculated for the 1100 nm period tri-segmented grating with a 3 mm central hole used here. From previous work it is known that atom number in a GMOT scales as $N \propto V^{1.2} \propto d^{3.6}$.[34] Finally, this normalised theoretical curve is scaled to the largest experimental atom number in the glass cell.

The numerically integrated optical overlap volume's coincidence with the 3 mm thick vacuum cell mounted 1 mm away is illustrated in Figure 4.6(b-d), highlighting the optical overlap volume clipping effect present in the chip-cale cell for a 20 mm diameter beam. Under the same conditions in the thicker glass cell the optical overlap volume is is 0.23 cm^3, only 21% of which exists within the 3 mm chip-scale cell.

The dashed line in Figure 4.6(a) shows a $d^{3.6}$ scaling of the atom number that can be expected from a beam that expands in three dimensions with no clipping.[85,86] Previous studies have shown that for significantly smaller overlap volumes in 6-beam[87] and pyramid[88] MOTs exhibit a d^6 scaling, as the atom number is instead limited by the stopping distance of the overlap volume rather than the cooling light intensity that dominates for larger beam diameters. It is noted that the measured atom number in the chip-scale cell is lower than the $V^{1.2}$ scaling of the red curve, the reasons for which are not currently understood.

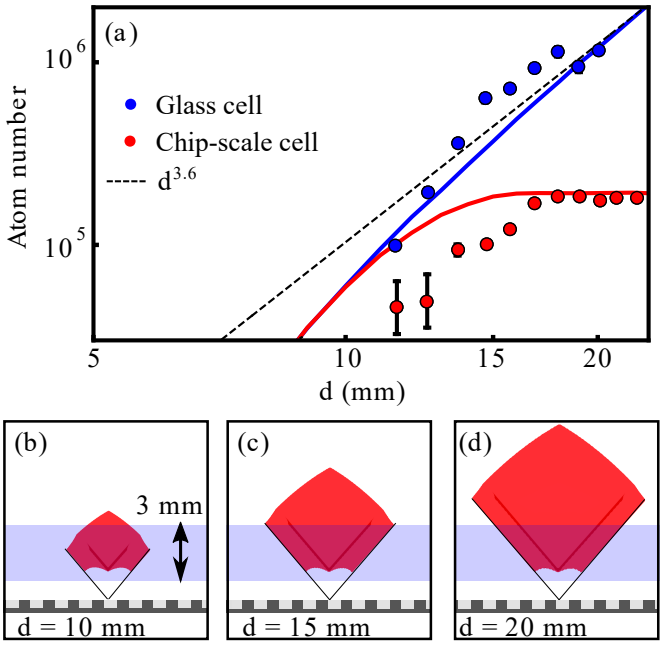

Figure 4.6: (a): Atom number measured from absorption imaging as a function of the incident beam diameter, d. Blue/red data points represent measurements made in a glass/chip-scale cell. Error bars were calculated from the standard deviation of 5 subsequent atom number measurements at each beam diameter. Where error bars are not visible they are smaller than the data point. The error bars at lower values of d are noticeably larger due to the atom number approaching the detection noise floor. Solid curves are theoretical expectations of the atom number, determined from numerical integration of the optical overlap volume from the grating chip as a function of d. The normalised theoretical atom number is pinned to the maximum measured atom number for the glass cell. The red curve shows an overlap volume that is restricted to a 3 mm height due to the vacuum volume of the chip-scale cell. The dashed line represents a $d^{3.6}$ fit to the atom number in the glass cell. (b)-(d) illustrate the optical overlap volume of the grating chip as a function of d with a highlighted 3 mm height of the chip-scale cell. The grey line highlights the grating chip position. Figure reproduced from Ref.[74]

4.1.4 Passive Pumping in a Chip-Scale Cell

As a final study with the chip-scale cell, passive pumping using non-evaporable getter pills was briefly investigated. Unfortunately at this point the dispensers used to source Rb were running out, necessitating the heating of the cell's copper stem in order to create a high enough vapour density to trap a significant number of atoms. This heating of the cell likely increased the non-rubidium vapour pressure within the cell, a non-ideal situation in a study on vacuum pressure.

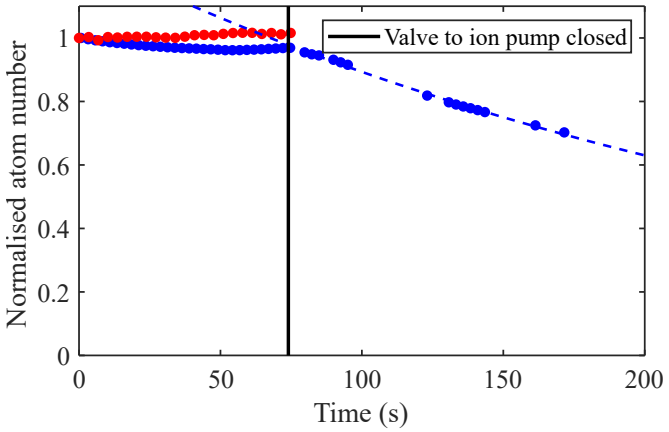

Figure 4.7: Initial passive pumping of chip-scale cell study. Red data: 0 activated NEGs. Blue data: 4 activated NEGs. Blue dashed line: fit to data, $N(t) = 1.27e^{(-t/286\ s)}$. Black vertical line shows time the cell was isolated from the ion pump. Gaps in data correspond to bad data points that have been omitted.

Four NEGs of 4 mm diameter (SAES ST172) were included in the cell design. These were then activated post-sealing of the cell using a 1070 nm laser capable of providing up to 20 W of optical power. As a baseline measurement of the time the cell can sustain pressures low enough for atom trapping, the cell was isolated from the vacuum pump using a gate valve while recording the trapped atom number which is measured for a newly loaded MOT approximately every three seconds. This cycle rate is a result of the time required to load a MOT in addition to imaging and computer processing time. With no NEG activation the MOT survival time is < 3 s, as shown in Figure 4.7. After acquiring this baseline, each of the four NEGs was heated by the activation laser in turn while the valve to the ion pump was open. This initial heating removes the passivation layer around the outside of the NEG consisting of pre-reacted NEG compound due to storage in atmosphere. After an inital spike of pressure within the cell, the

laser intensity is reduced to maintain a pressure $< 10^6$ mbar (measured by the ion pump) so as not to flood the chamber. This process was repeated several times until a drop in pressure while heating was observed, indicating the passivisation layer had been completely removed.

Once all 4 four NEGs had been activated, the valve to the ion pump was again closed and the MOT number measured continuously, results of which are also shown in Figure 4.7. In this case the MOT was observable for as long as 100 s after isolation before the atom number dropped below measurable levels, an increase of 33×. Previous studies of passive pumping using NEGs reported a sharp initial drop in atom number before stabilising at a new level around an order of magnitude lower than the initial atom number.[80] Assuming a similar dynamic in this cell we can expect a much improved vacuum lifetime than measured here due to the atom number decaying quickly below measurable levels.

4.1.5 Conclusion and Future Work

To conclude, a simple imaging solution for the measurement of trapped atom number in a chip-scale cooling platform has been developed. The introduction of the central hole in the grating chip, used to provide an imaging axis, shows negligible atom number degradation while providing enough numerical aperture for the imaging of small atom numbers. The 3 mm height of the micro-fabricated chip-scale cell has been found to reduce the maximum atom number due to a spatial mismatch between the grating optical overlap volume and the vacuum volume, calculated at 21% overlap. Through the machining of thicker silicon wafers this overlap can be increased significantly. Recent demonstrations of thick silicon machining with a waterjet cutter[89] within the Experimental Quantum Optics and Photonics group have since allowed a 6 mm thick cold-atom cell to be constructed.[90] This cell allows 93% of the optical overlap volume to exist within the cell and demonstrated a trapped atom number of 4×10^6, inline with traditional vacuum cells.

The larger initial atom number present in the thicker cell will also facilitate a more robust and comprehensive study of passive pumping in silicon chip-scale cells. This will hopefully lead to fully sealed off high vacuum cells, suitable for portable cold-atom applications, created in a much more scalable manner than has previously been demonstrated.

It may be advantageous to apply an anti-reflection coating to the cell windows

during fabrication due to the increased etaloning observed in the through-hole images. While the effect of these fringes on the images was minimal, especially for larger MOTs, and can be mitigated through alignment, there are also several fringe removal algorithms that can be applied in post-processing to further reduce their impact.[91,92]

4.2 MEMS Scanning Mirrors

One outstanding challenge in the miniaturisation of atomic based quantum sensors is that of dynamic manipulation of cold-atom ensembles. Fine control of atom distributions by optical means is well established and used extensively throughout quantum optic experiments, from simple dipole traps[93] and optical tweezers,[94] whose position is typically controlled by 1D or 2D AOM devices, to more complex arbitrary atom arrays formed by spatial light modulators (SLMs) or digital micro-mirror devices (DMDs).[95,96] These techniques also allow for shaping of time averaged potentials, for example by scanning orthogonal AOM pairs[97,98] while simultaneously providing a means to optically shutter the incident light. However, AOMs typically require RF signals in the 100-MHz range with 1 W of power, and need extended optical paths to allow spatial separation of diffracted orders. Application of SLMs and DMDs in cold-atom systems is continually advancing, yet these remain expensive, and also require similar optical footprints as AOM devices. With the goal of transitioning towards complete devices, these solutions for optical manipulation remain non-ideal.

Previous research has demonstrated the suitability of scanning MEMS micro-mirrors as an alternative method of dynamically manipulating laser beams to enable addressing of neutral atom or ions with single-particle resolution. Work reported in literature has used two orthogonally scanning MEMS mirrors to provide two-dimensional (2D) control of beam position.[99–101] In collaboration with Strathclyde's Electronic and Electrical Engineering department, a proof-of-principle experiment using 2D time-averaged painted light potentials in an ensemble of cold atoms was investigated.

The atomic cloud is first shelved in the $|F = 1\rangle$ ground state, a dark state to the imaging light that is tuned to the $|F = 2\rangle \rightarrow |F = 3\rangle$ transition. By selectively "painting" hyperfine-repumping light onto the cold atom ensemble using two silicon-on-insulator MEMS micro-mirrors and independently controlling each mirror we locally excite and image fluorescence within the atom cloud. The

quality of these images can be used to assess the applicability of this technique in cold-atom applications.

This technique is highly scalable, low SWaP, and offers the opportunity for simultaneous control of multiple wavelengths of light; typically more difficult to achieve with AOM control.[102]

4.2.1 Cold-Atom Shaping with MEMS Mirrors

To investigate the MEMS mirrors a cloud of cold atoms is prepared in the usual manner using a 2 cm × 2 cm "tri" grating[34] as discussed in Chapter 3. During the MOT load and molasses stages repump light is derived from an EOM. This is extinguished during the MEMS beam addressing. A cloud of $\approx 2\times10^6$ atoms were prepared and cooled to 50 μK using 10 ms of red molasses and a further 3 ms of grey molasses. This rather modest temperature was due to difficulties with the shim coils used in the test setup to cancel stray magnetic fields and does not pose an issue in this case. The second molasses stage was utilised due to the higher atomic densities typical of grey molasses,[51] giving a higher signal to noise ratio in the resulting MEMS re-pump addressing images. In addition to this, the grey molasses efficiently pumps the atoms into the dark $|F = 1\rangle$ ground state,[51] helping to prepare them for the MEMS addressing stage. Once the atom cloud has been prepared in the $|F = 1\rangle$ ground state the main re-pump light derived from the EOM is turned off with an extinction of 65 dB to ensure that the only re-pump light incident on the atoms originates from the MEMS addressing. We then wait 1 ms with the cooling beam on to ensure as many atoms as possible are shelved in the $|F = 1\rangle$ ground state before turning the MEMS addressing beam on.

The MEMS addressing beam is derived from an extended cavity diode laser (ECDL)[56] locked via saturated absorption spectroscopy. The power level of this light is controlled using a single pass AOM that can be rapidly turned on and off. This light, now resonant with the D_2 $|F = 1\rangle \rightarrow |F' = 2\rangle$ transition, is then fibre coupled and passed to the MEMS mirror scanning system.

The scanning system was constructed by Paul Janin[103] and is based on a pair of MEMS scanners that are used to steer the MEMS addressing beam in two dimensions onto the cold atom cloud. Each scan axis is driven near the respective mirror's resonance frequency, which for one of the mirrors can be thermally tuned to create the desired scan profiles. The fibre-coupled laser beam is collimated

into free space with a waist of 1 mm and focused to a point roughly 30 mm before the surface of the first MEMS scanner ($MEMS_1$) by a 150 mm focal length achromatic lens. The beam reflected from $MEMS_1$ is imaged onto $MEMS_2$ by a matched achromatic doublet pair with 100 mm focal length, ensuring that beam steering deflections originate from the same point on the optical axis. The MEMS mirrors are positioned to align their scan axes orthogonally. The scanner image is then relayed through a 30 mm focal length achromat followed by a 200 mm plano-convex lens, such that the final scanner image is placed in the object plane of the final focusing lens.

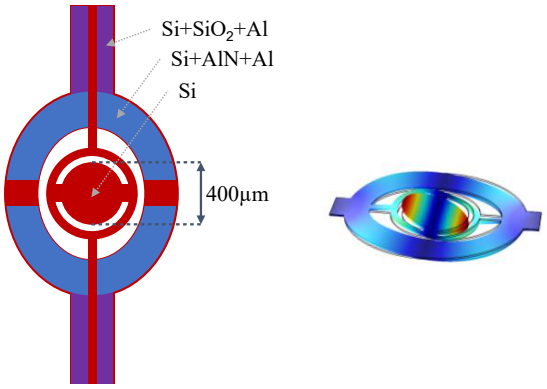

Figure 4.8: Left: Schematic of the 400μm diameter mirror. Right: Schematic showing the out of plane rotation of the mirror surface. Figures reproduced from Ref.[75]

Details on the scanners themselves can be found in Refs,[75,103] a diagram of the mirrors is shown in Figure 4.8 . In brief: the mirrors are resonant piezo-electric MEMS with a 400 μm mirror aperture fabricated using a commercial multiuser process (MEMSCAP PiezoMUMPS).[104] Each mirror consists of an outer frame connected via suspension beams to the inner mirror surface. By actuating the mirrors at their resonance frequencies, out of plane rotation of the mirror surface is observed along the suspension beams. The resonant frequency of the mirrors is around 90 kHz with a maximum optical scan angles of 25° and 12° for each mirror (labelled $MEMS_1$ and $MEMS_2$ respectively).

In order to compensate for discrepancies in resonance frequencies between the two scanners resulting from variations and tolerances during the fabrication process, $MEMS_2$ can be tuned by localized heating of the device through three on-chip thermal actuators. This concept is described in detail in Ref.[104] Through thermal tuning, the resonance frequency can be reduced by around 1.5 kHz, from

91.5 to 90 kHz, making actuation at 90 kHz possible with a sufficient optical scan amplitude for synchronised scanning purposes.

Imaging of the atom cloud was preformed by standard fluorescence detection on a CCD camera with the imaging axis offset by 12° from the addressing axis due to optical access.

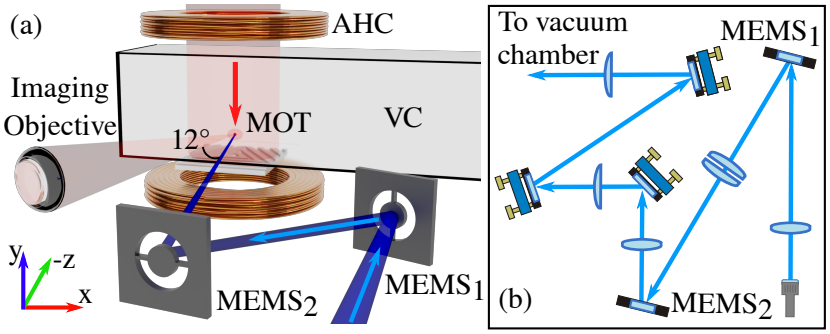

Figure 4.9: (a) Simplified experimental set-up. Single trap beam (red) is aligned onto grating chip mounted externally to vacuum cell (VC) also shown are the anti-Helmholtz trapping coils (AHC). MEMS addressing beam (blue) is shown aligned into the MOT region with two orthogonally scanning MEMS mirrors $MEMS_1$ scans the x-axis while $MEMS_2$ scans the y-axis. The imaging axis is shown rotated by ≈12° from the MEMS addressing axis. (b) Overview of full MEMS scanning system, showing the re-pump beam preparation and alignment using two MEMS scanners. Figure reproduced from Ref.[75]

An image of the whole atom cloud after optical molasses is shown in Figure 4.10 (a). This image was taken with the main experimental re-pump light, derived from the EOM, incident on the atoms and shows the extent of the atom cloud to be roughly 3 mm in the horizontal axis and 1.6 mm in the vertical axis. Figure 4.10 (b) shows an image of the atom cloud after extinguishing the main re-pump light and turning the MEMS addressing beam on with no MEMS mirror scanning present. When a Gaussian distribution is fitted to the vertical axis of the image in Figure 4.10 (b) a waist of 300 μm is calculated. This differs to measurements of the MEMS addressing beam giving a beam waist of 40 μm. The apparent broadening is largely attributed to the relatively long exposure time of the fluorescence images of 1 ms and heating of atomic cloud during near-resonant imaging, resulting in the motion of atoms within this time window. These parameters were required to optimise signal to noise in our imaging system. This broadening of the resolution could be reduced by a higher-collection efficiency imaging or by absorption imaging.

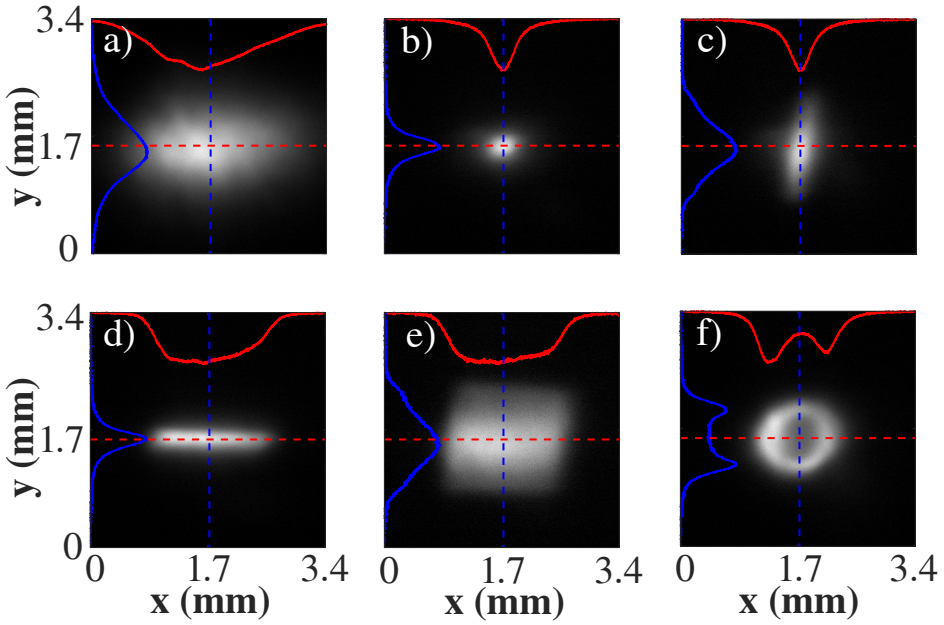

Figure 4.10: (a) Images of atomic fluorescence for $\approx 2 \times 10^6$ atoms loaded into the standard GMOT. (b) Region of atom cloud illuminated by MEMS addressing beam with no MEMS scanning. (c) Vertical MEMS mirror scan. (d) Horizontal MEMS mirror scan. (e) Square scan using both MEMS with Lissajous scanning. (f) Circular scan driving both MEMS with the same frequency and pi/2 phase shift. All images are individually normalised to the maximum recorded pixel count of the respective image. Figure adapted from Ref[75].

By actuating each MEMS mirror individually we can create single line scans in the vertical and horizontal axis, as shown in Figure 4.10 (c) and (d) respectively. These narrow line potentials are again broadened with respect to the incident beam, giving waists of 260 μm for the horizontal scan and 380 μm for the vertical scan, with a scan length of 2 mm and 1.4 mm respectively. The additional broadening of the vertically scanned beam is likely due to the imaging axis being rotated with respect to the incident beam. When the 2D scan line is projected onto the 3D MOT, the resulting distribution of bright atoms is a plane through the centre of the MOT. When this plane is viewed at an angle with respect to the scanning beam some of the bright atoms from the back of the plane are projected onto the imaging plane.

Line profiles showing the intensity profiles through the centre of the cloud are shown by the red and blue overlays in Figure 4.10 (a)-(f). Local fluorescence within the atom cloud results from a combination of the local atomic density and

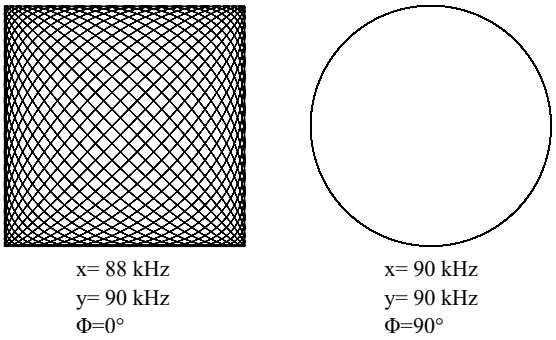

Figure 4.11: 2D profiles of the Lissajous scans.

the time averaged beam intensity at each location along the scan axis. Due to the rotation of the mirrors around their fundamental tipping mode, the addressing beam spends more time interacting with atoms at the extremes of the scan. By contrast however there is a lower atomic density at the edges of the scans due to the MOT's Gaussian profile. The combination of these effects in the ideal case leads to a flattened intensity profile around the centre of the MOT with Gaussian edges originating from the Gaussian addressing beam as shown in Figure 4.10 (d). When scanning vertically as in Figure 4.10 (c) the intensity profile can be seen to diverge significantly from the ideal square case. This discrepancy between the horizontal and vertical scans is due to the characteristic "pancake" shape of GMOTs, where slightly larger axial trapping forces compared to radial trapping cause the MOT to be compressed in the vertical axis.[37] When the scan length is of the same order as the atom cloud's dimension in that axis the larger variation in atomic density across the scan length causes this deviation in the scan profiles.

Next the mirrors were simultaneously driven around their respective resonance frequencies (87.6 kHz for $MEMS_1$ and 90.4 kHz for $MEMS_2$), producing a time averaged square light potential within the cloud, shown in Figure 4.10 (e). This results from the Lissajous scan pattern with 1.97×10^5 cross-over points per axis, generated by the precise frequency spacing between both base resonances. This concept is illustrated in Figure 4.11. Line profiles through each axis of this image once again show a good approximation to a square profile in the horizontal axis with the vertical axis deviating significantly from the ideal square potential.

A circular scan, shown in Figure 4.10 (f), is generated when the resonance frequencies of both MEMS mirrors are identical, with a 90° phase shift between their movements. To achieve this the frequency tuning actuation of $MEMS_2$ was utilised, with a 7.5 V_{DC} tuning voltage applied to one of the thermal tuning

actuators and 10 V_{DC} to the other two, while $MEMS_1$ was left at its original resonance. This led to a matched resonance frequency and therefore circular scan frequency of 90 kHz, with the scanning beams creating a trace for a ring potential. One requirement for optical ring potentials within BECs for interferometry is that the light potential is smooth across the whole profile of the ring. While Figure 4.10 (f) shows a clear imbalance in intensity of the left hand side of the ring compared to the right, this effect is primarily due to the 12° rotation in the imaging axis with respect to the MEMS addressing beam. This rotation means the three-dimensional hollow cylinder of bright atoms is projected into the imaging plane at an angle. The pixel counts measured by the CCD are proportional to both the atomic scattering rate and density of atoms, taking into account the three dimensional nature of the hollow cylinder of bright atoms. As highlighted in Figure 4.12 one side of the image will be integrated over a higher density of atoms than the other, resulting in the intensity imbalance observed in Figure 4.10 (f). Another contributor to this intensity imbalance is local variations in atomic density, visible in Figure 4.10 (a). Previous demonstrations of ring potentials have accounted for these local variations in density by modulating the light intensity as it is scanned with orthogonal AOMs.[98] Implementing some feedback on light intensity the 2D MEMS mirror scanner would also serve to create smoother potentials for use in portable quantum optic experiments, with required modulation frequencies of 90 kHz within easy reach of direct diode modulation schemes.

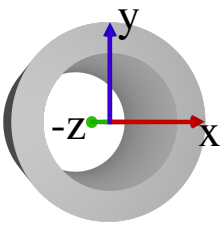

Figure 4.12: A pictorial representation of the 2D circular scan, projected into three dimensions, observed at 12° with respect to the MEMS addressing beam propagating along the z-axis. Figure adapted from Ref[75].

4.2.2 Conclusion and Future Work

To summarise, time-averaged light potentials in cold atom ensembles have been created using MEMS mirrors. By independently driving two orthogonally scanning MEMS mirrors with resonance frequencies above 90 kHz line, circle, and

filled-square profiles of bright fluorescing atoms within a larger dark atom have been created. This technique further demonstrates the applicability of MEMS microfabrication techniques for replacing high SWaP lab-based equipment, building on previous research towards the miniaturisation of cold atom experiments for the realisation of truly portable cold atom sensors.

The wide bandwidth of available reflection coatings on the MEMS mirrors make this technique ideal for simultaneous control of multiple wavelengths of light, typically more difficult to achieve using AOM control.[102] The technique could be extended to dynamic beam shuttering. More dynamic control of the scan amplitude and phase would make it possible to form more complex geometries opening the technique to more applications such as the storing of images for quantum information processing,[105] selection of individual layers of optical lattices,[106] generation of arbitrary geometry matterwave circuits[107] and all-optical adaptable atomtronics[108]

Chapter 5

On-Chip Optical Lattice

This chapter discusses a proof-of-principle experiment in ^{87}Rb where the possibility of loading atoms from a GMOT directly into an optical lattice formed using the same chip is investigated. Depending on the wavelength of light relative to the grating period and the number of grating segments the lattice beam is aligned onto, it should be possible to form 1D, 2D and 3D optical lattice geometries using the same grating chip. As each beam originates from a single input beam, phase noise should be common to all beams, improving the phase stability of the created lattice structures.

5.1 Motivation

Optical lattices, formed by the standing wave of two or more interfering laser beams offer a convenient platform for many quantum-optics experiments.[10,93,109] The extremely long atomic coherence lifetimes possible in such optical traps[12] have been used extensively in some of the most sensitive measurements to date, notably allowing optical atomic clocks to reach fractional frequency accuracies at the 10^{-18} level.[7,110]

Optical-lattice-based devices generally occupy a large experimental footprint and are notoriously difficult to make portable due to the many highly sensitive components and requirement for high optical access with multiple distinct beam paths, intersecting at the atom location.[110,111] In a typical alkaline-earth lattice clock experiment, for example, upwards of seven distinct wavelengths of light can be required for broadband cooling, narrow-line cooling, various repump frequencies, optical pumping, lattice formation and finally the optical clock transition.[10] It is clear that any simplification to the optical system required to trap atoms

in a MOT and cool them to low enough temperatures to load into the optical lattice will be of great help in creating more portable optical lattice clocks and interferometers.

Several groups, including the University of Strathclyde, are currently investigating methods of extending compact laser cooling experiments to the alkaline-earth metals with a view towards the goal of reducing both the size and complexity of the next generation of atomic sensors. Various distinct approaches are currently being taken towards this goal with pyramid MOTs,[112] metasurface MOTs,[113] new Fresnel-reflector MOTs[36] and notably GMOTs[45–47] all being the subject of investigation. As the implementation of cooling using these compact techniques is well in hand, we turn our attention to the integration of the optical lattice in a compact and robust fashion.

In most cases the integration of a simplified and robust optical lattice has as yet gone uninvestigated, although Bowden *et al.* have made efforts towards integrating an optical lattice with a compact pyramid MOT.[112] An optical lattice formed using a beam reflected from an atom chip has previously been demonstrated.[114] Here the atoms were loaded from a Mirror MOT into a magnetic trap and sequentially into the lattice potentials. Additionally, a 3D lattice, again loaded from an atom chip was demonstrated by Straatsma *et al.*[115] In this case the authors created an on-chip BEC and subsequently loaded it into the lattice formed by microfabricated mirrors bonded to the chip surface.

Another issue in lattice experiments is the fact that if the lattice laser phase changes, perhaps due to a mechanically vibrating mirror, the light interference pattern is modulated. In a 1D lattice this effect translates the interference pattern along the beam axis and the lattice structure is preserved. In the case of 2D and 3D lattices however the entire lattice geometry is modulated; in the worse case scenario washing out the interference pattern all together.[116] One solution to this issue is to create a "folded" lattice geometry where a single beam is reflected multiple times so as to address each Cartesian axis.[117] While this ensures laser phase fluctuations are common to all beams and individual beam phase differences can be compensated for, it does significantly increase the size and complexity of the optics required. Another potential solution is to detune beams directed along each orthogonal trapping axis relative to each other. This ensures that the intensity interference pattern between standing waves in each orthogonal axis oscillates rapidly, averaging to zero.[118] Phase fluctuations therefore do not modulate the lattice trap depth at the timescales of interest to the atom be-

haviour. This increased resilience to phase fluctuations comes at the expense of a more complex system, requiring the light for each lattice axis to be frequency shifted.

By forming multi-dimensional lattices from the diffracted beams created by a single optic, all beams share a common phase pinned to the grating surface. The silicon GMOT chip is sufficiently stiff that surface vibration modes are negligible and only centre of mass motion of the chip need be considered. Any change in the laser phase due to mechanical vibrations or laser phase noise will consequentially be common to all beams. This configuration produces phase-stable lattices without the need for mechanical feedback onto mirror positions or the more complex optical schemes that are employed currently. We anticipate that this highly stable optical lattice geometry will prove more robust to the demanding environments of portable quantum-optic experiments in addition to simplifying current lab-based lattice experiments. While this investigation was carried out in ^{87}Rb due to available equipment, the concept is readily transferable to other elements.

5.2 The Dipole Force

The dipole force arises due to the induced dipole moment, $\vec{d}$, of an atom when placed in an electric field, $\vec{E}$. The induced dipole moment oscillates at the driving field and is given by

$$\vec{d} = \alpha(\omega)\vec{E}, \tag{5.1}$$

where α is the real part of the complex polarisability. The instantaneous dipole potential from this interaction is then given by

$$\begin{aligned} V_{\text{inst}} &= \int_0^E -\vec{d}(E) \cdot dE \\ &= -\frac{1}{2}\vec{d} \cdot \vec{E}. \end{aligned} \tag{5.2}$$

The intensity of the light field is expressed as

$$I = \frac{1}{2}\epsilon_0 c|E|^2, \tag{5.3}$$

where ϵ_0 is the permittivity of free space. Rearranging Eq 5.3, taking the time average and substituting into Eq 5.2 along with Eq 5.1 gives the time averaged dipole potential, equivalent to the atomic light-shift,

$$V_{\text{dipole}} = -\frac{1}{2\epsilon_0 c}\alpha I. \tag{5.4}$$

The dipole force itself arises due to gradients in the light field,

$$\begin{aligned} F_{\text{dipole}} &= -\nabla V_{\text{dipole}} \\ &= \frac{1}{2\epsilon_0 c}\alpha \nabla I. \end{aligned} \tag{5.5}$$

When an atom is placed in a light field that is red detuned from an atomic transition, the polarisability is positive and an attractive force is applied to the atom. Resulting in the atom being attracted to regions of high intensity. The converse is true of blue detuned light, with the atom attracted to regions of low intensity light. Blue detuned traps typically offer a higher trap lifetime as photon scattering in the low intensity regions is reduced, thus reducing the atomic heating rate.[93]

5.2.1 Polarisability

The real part of the atomic polarisability is calculated following the derivation in Ref.[119] This calculation considers the AC Stark energy shift, Eq 2.28, with a Rabi frequency defined by Eq 2.11. The total energy shift is then found by staking the sum over the contributions of each transition,

$$\Delta E_i = \frac{3\pi c^2 I}{2} \sum_{f \neq i} \frac{A_{if}}{\omega_{if}^3} \left(\frac{1}{\omega_{if} - \omega} + \frac{1}{\omega_{if} + \omega} \right), \tag{5.6}$$

where ω_{if} is the angular frequency of the transition between the levels i and f and A_{if} is the transition's Einstein A coefficient. The real part of the polarisability can then be expressed by equating to Eq 5.4,

$$\alpha = -3\pi e_0 c^3 \sum_{f \neq i} \frac{A_{if}}{\omega_{if}^3} \left(\frac{1}{\omega_{if} - \omega} + \frac{1}{\omega_{if} + \omega} \right). \tag{5.7}$$

A plot of the polarisability as a function of wavelength is shown in Figure 5.1, calculated with respect to the D_1 and D_2 line. Other transitions are sufficiently detuned as to play little role in the total polarisability at the wavelengths of interest. This plot clearly shows the difference in polarisability from red and blue detuned light, indicating the importance the detuning will have on trap dynamics. This plot also shows the calculated polarisability, and therefore trap

depth, increases dramatically when lower detunings are utilised. As will be shown in the following sections, this has the adverse effect of a much increased photon scattering rate in the trap. When operating with a fairly limited optical power as with the 3D lattice created here, lower detunings allow the formation of a deep enough trapping potential to localise atoms.

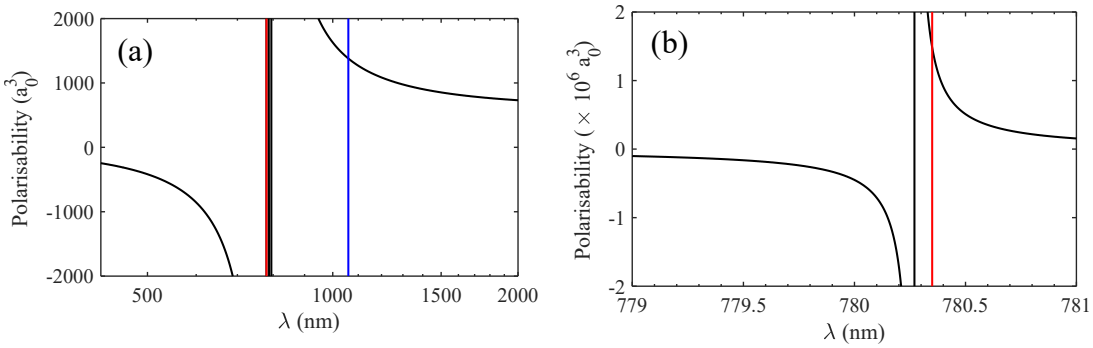

Figure 5.1: Black line: Scalar atomic polarisability, calculated relative to the ^{87}Rb D_1 and D_2 line. Red line: Wavelength used for creation of the 3D lattices. Blue line: Wavelength used for creation of the 1D lattice. (b) shows polarisability around the 3D lattice wavelength for clarity.

5.3 Lattice Potentials

The simplest form of trap via the optical dipole potential utilises a focused Gaussian beam that is red detuned from a strong atomic transition. Axial trapping along the beam propagation axis is provided by focusing the beam to provide an intensity gradient, while radial trapping is provided by the Gaussian profile of the beam. This concept was first proposed by A. Ashkin.[120] The first optical trap for neutral atoms was subsequently demonstrated using sodium atoms by S. Chu *et al.*[121]

The trap depth is calculated by first considering the electric field strength of a Gaussian beam propagating along the z-axis and described by[119]

$$E(r,z) = E_0 \frac{w_0}{w(z)} e^{-r^2/w(z)^2} e^{i(kz-\omega t)} e^{ikr^2/2R(z)} e^{-i\Phi_G(z)}. \tag{5.8}$$

Here $w(z)$ is the beam radius at position z, w_0 is the minimum beam radius, $R(z) = z + (z_R^2/z)$ is the beam's radius of curvature with z_R the Rayleigh range ($z_R = \pi w_0^2/\lambda$) and k is the wavenumber ($2\pi/\lambda$) of the light. Finally, ϕ_G is the Gouy phase due to the Gaussian nature of the beam, defined as $\tan^{-1}(z/z_R)$. For

the case of optical lattices, multiple beams described by Eq 5.8 are used, each with the same wavelength but different wave vectors. The total electric field is simply the sum of the individual fields, the resulting interference pattern allows atoms to be localised at the intensity maxima. Once the electric field strength is known, the trap depth is calculated using Eq 5.3 and Eq 5.6. This trap depth in energy units can then be related to a temperature by $\Delta E_i/k_B$.

5.3.1 Heating Rate

It is useful to have some idea of the atom heating rate within the lattice as a result of photon scattering events. In the near-detuned optical lattices described in the following sections, photon scattering is likely to be an important limiting factor to the lattice lifetime. When an atom scatters a photon it recoils with energy $2E_{\text{recoil}}$, previously defined by Eq 2.30. The heating rate is therefore given as[93]

$$\frac{dT}{dt} = \frac{2}{3}\frac{E_{\text{recoil}}}{k_B}\Gamma_{sc}. \tag{5.9}$$

The additional factor of a third here is a result of the three degrees of freedom available to the atom in the harmonic trap. The scattering rate, Γ_{sc}, in the case of far detuned light, is defined as[93]

$$\Gamma_{sc} = \frac{3\pi c^2 I}{2\hbar}\sum_{f\neq i}\frac{1}{\omega_{if}^3}\left(\frac{\omega}{\omega_{if}}\right)^3\left(\frac{A_{if}}{\omega_{if}-\omega}+\frac{A_{if}}{\omega_{if}+\omega}\right)^2. \tag{5.10}$$

5.3.2 Trap Oscillation Frequencies

At the bottom of each trap site, the trapping potential can be considered harmonic. This allows the trap oscillation frequencies to be estimated using the Taylor expansion of the trapping potential in either the radial (r) or axial direction (z) and Hooke's law,

$$U(r,z) = \frac{1}{2}kx^2. \tag{5.11}$$

First consider the radial axis where the potential varies as the square of the first exponential term in Eq 5.8,

$$U(r) = U_0 e^{-\frac{2r^2}{w_0^2}} \equiv U_0\left(1-\frac{2r^2}{w_0^2}+...\right). \tag{5.12}$$

Equating the second order term of Eq 5.12 to Eq 5.11 with the spring constant given by $k = \omega_{r,z}^2 m$ where m is the atomic mass. The radial trapping frequency, $\nu_r = \omega_r/2\pi$, is then found to be

$$\nu_r = \frac{1}{2\pi}\sqrt{\frac{4U_0}{mw_0^2}}. \tag{5.13}$$

In a similar fashion the trapping frequency in the axial direction can also be found (for the well defined 1D case). In this case the potential varies sinusoidally due to the multiple beam interference, resulting in a potential that is well described by

$$U(z) = U_0 \cos^2\left(\frac{2\pi z}{\lambda}\right) \equiv U_0\left(1 - \frac{4\pi^2 z^2}{\lambda^2} + ...\right), \tag{5.14}$$

where U_0 is now the peak intensity resulting from the two beam interference. Following the same steps above the axial trap frequency is found to be

$$\nu_z = \frac{1}{2\pi}\sqrt{\frac{8\pi^2 U_0}{m\lambda^2}}. \tag{5.15}$$

For the slightly more complex 2D and 3D case (Sec 5.3.5) the curvature in potential is not fully described by a simple sinusoid. In these cases the curvature of the trapping potential can be found numerically.

For completeness the axial trapping frequency for a *single* beam dipole trap is calculated from the Taylor expansion of $U_0\frac{w_0^2}{w(z)^2}$, giving a trap frequency of

$$\nu_z = \frac{1}{2\pi}\sqrt{\frac{2U_0}{mz_R^2}}. \tag{5.16}$$

5.3.3 Grating Lattice Geometries

By selecting an appropriate lattice wavelength and beam alignment onto the grating it is possible to form 1D, 2D and 3D lattices using a single grating chip. A tri-segmented binary grating coated in 100 nm of aluminium is used throughout the work described in this chapter, an image of which is presented in Figure 5.2. This grating has dimensions 2 cm×2 cm and a period of d =1080 nm. The angle of diffraction of an incoming beam with normal incidence to the grating surface is described by the well-known grating equation,

$$m\lambda = d\sin(\theta), \tag{5.17}$$

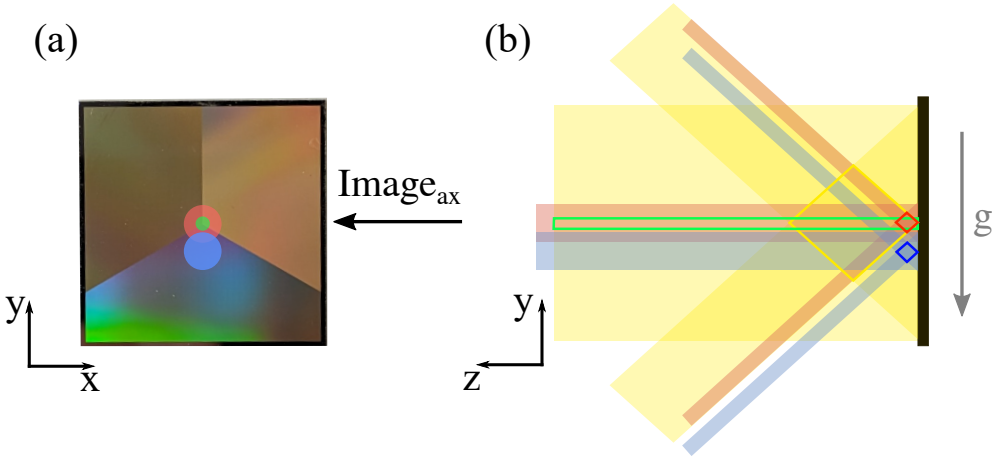

Figure 5.2: (a) Image of tri-segment binary grating. The red circle indicates beam position for 3D lattice. The blue circle indicates beam position for 2D lattice. The green circle indicates beam position for 1D lattice. (b) Input and diffracted beam configurations for both MOT and lattice beams, shown in 2D. Optical overlap volumes are highlighted as coloured diamond shaped regions. Direction of gravity in experiment is also shown along with the imaging axis (Image$_{ax}$), which is directed along the x-axis.

where m is the order of diffraction, λ is the light wavelength and θ is the angle of diffraction.

1D Lattice Geometry

From Eq 5.17 we see that if the wavelength is chosen such that $\lambda > d$ the 1st order diffraction angle becomes non-physical. As a result, all the light is contained in the $m = 0$ diffracted order (or lost due to effects such as absorption by the grating) and the grating acts as a retro-reflecting mirror. This ideal configuration provides a simple way to form a 1D lattice using the grating chip. The 1D lattice optical overlap region (marked in Figure 5.2(b)) is not defined by the diffraction angle, this means the beam can be aligned at any point on the grating chip and still form the same lattice structure. Due to the MOT optimally forming in the centre of the grating chip however, the best loading efficiency into the 1D lattice potentials is achieved when the lattice beam is also aligned to the centre of the grating. As interference occurs along the entire length of the 1D lattice beam, the height the lattice forms above the grating chip is not defined by the diffraction angle. A relatively small beam with a $1/e^2$ radius of 80 μm can therefore be used, allowing for a high intensity and therefore lattice trap depth.

Available laser sources during the investigation meant that a 1070 nm laser was used for the 1D lattice. This produces some diffraction from the grating with a 1st order diffraction angle of 82°. While this angle is high enough that the light does not interact with the atoms, it does reduce the power in the retro-reflected beam, modifying the lattice depth. This effect is measured and taken into account during the theoretical treatment in the following section.

3D Lattice Geometry

The 3D lattice optical overlap volume forms in exactly the same way as the MOT optical overlap volume with the beam aligned onto all three grating segments. Three diffracted beams, in addition to the input beam, interfere to form standing waves in three dimensions where atoms can be trapped. Unlike the 1D case the maximum height above the grating the lattice can form is now defined by the angle of diffraction of the light (see Figure 5.2). The 3D lattice was investigated at 780.30 nm – 780.40 nm, resulting in a $m = \pm 1$ order diffraction angle of θ=46°. To ensure a good overlap between the MOT and lattice potentials a beam with a $1/e^2$ radius of 2.5 mm was used. The top of the 3D lattice structure is therefore around 2.6 mm above the grating, allowing easy loading directly from the MOT.

2D Lattice Geometry

Formation of a 2D grating-lattice is possible by aligning the lattice beam to a single region of the grating chip (highlighted in Figure 5.2(a)). Here the $m = \pm 1$ diffracted orders interfere with the input beam to form cigar shaped optical potentials, parallel to the grating surface. One unfortunate feature of this configuration is the fact the lattice forms below the MOT optical overlap volume (at the currently available wavelengths of light), highlighted in Figure 5.2. While direct lattice loading from the MOT is not feasible for this lattice geometry and wavelength, indirect loading is still possible. By initially loading the atom cloud into a magnetic trap and shifting the trap centre to coincide with the optical potential, efficient loading of the 2D lattice should be possible. This will necessarily add complexity to both the experimental set-up and sequence, however, magnetic trapping could feasibly be accomplished by microfabricating current carrying wires below the grating structure. Patterning wires onto the grating chip for on-chip magnetic trapping is actively under investigation both within the University of Strathclyde and by collaborators at Leibniz University Hannover.[44]

Although this would provide an ideal means of loading into the 2D lattice, loading could also feasibly be accomplished by increasing the lattice wavelength with respect to the grating period. The resulting increase in lattice beam diffraction angle could then facilitate a high enough overlap between the MOT and lattice optical overlap volumes.

5.3.4 Theoretical 1D Lattice

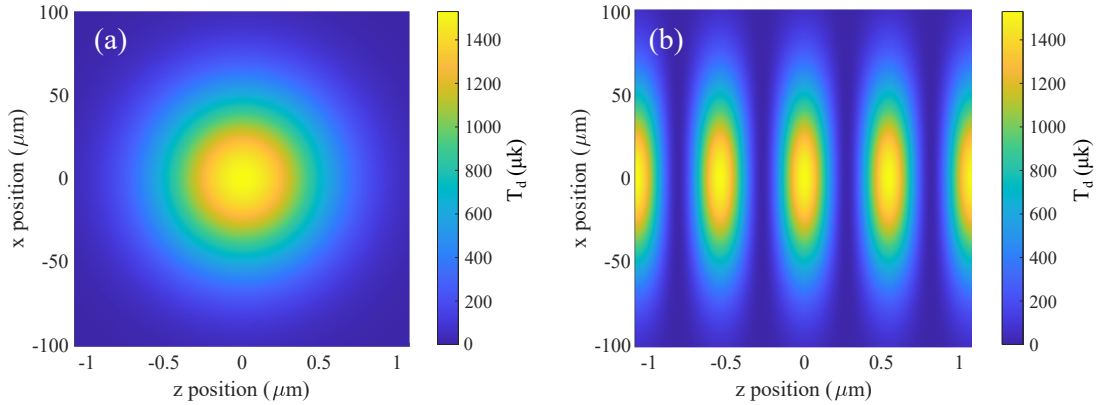

Figure 5.3: Theoretical 1D lattice trap depth for Rb, shown in the radial direction (a) and axial direction (b). Note the different axis scales in (b). Plotted for λ=1070 nm, $w_0 = 80\ \mu m$, P=10 W, with $P_{\mathrm{m}=0} = 0.7P$.

Due to the simplicity of the retroreflected 1070 nm geometry, modelling the 1D lattice in three dimensions is relatively easy. To do this, the workflow laid out in Ref[119] by K. Weatherill is followed.

Gaussian beams, defined by Eq 5.8, counter-propagating along the z-axis are considered. To model the interference of the two beams a grid of points in the labframe is first defined. The electric field at each point in the space is then calculated for each beam separately and the contribution of each beam summed. Eq 5.3 and Eq 5.6 are then used to calculate the trap depth at each point in the grid. Slices can then be taken through the space defined in 3D to find information on the lattice trap depth and shape at various locations.

As noted in Sec 5.3.3 the grating does not act as a perfect reflector for 1070 nm light. Some diffraction along with a 95% reflectivity of the aluminium coating[122] results in approximately 70% of the light incident on the grating being retroreflected. This imperfect reflection is taken into account by introducing an additional variable $P_{\mathrm{m}=0}$, where $P_{\mathrm{m}=0}$ is some fraction of the incident light power,

P. A plot of the theoretical trap depth as a function of position, accounting for optical losses, is shown in Figure 5.3.

The effect optical losses in the reflected beam has on the lattice trapping parameters is summarised in Table 5.1. A comparison is also drawn to the trapping parameters if a simple dipole trap, with no lattice structure, was instead formed for the same experimental conditions. This comparison is used in Sec 5.7 as additional proof of the lattice formation.

	Dipole trap	1D ($P_{m=0} = P$)	1D ($P_{m=0} = 0.7P$)
T_d (μK)	453	1806	1523
Γ_{sc} (s^{-1})	1.07	4.28	3.61
ν_r (kHz)	0.67	1.35	1.24
ν_z (kHz)	2.03 (Hz)	449	411

Table 5.1: Theoretical trapping parameters for a dipole trap and the 1D lattice. Comparison is also made between a 1D lattice formed from a perfectly reflected beam and with 70% reflection from the grating as in the experiment. Calculated for: $w_0 = 80$ μm, P=10 W, λ=1070 nm. Lattice spacing= $\lambda/2$.

5.3.5 Theoretical 3D Lattice

Due to time constraints and the additional complexity of modelling the 3D optical lattice in three dimensions, it was not possible to extend the model presented above for a 1D lattice to higher dimensional lattices. While the basic theoretical description of the 3D lattice remain the same as that presented above, modelling the interference of the various beams becomes more difficult due to the more complex geometry of diffracted beams which are rotated with respect to each other and angled with respect to the input beam.

The following theoretical lattice trapping parameters are therefore based on theoretical simulations by Dr Aidan Arnold who kindly provided the code to do so. These expected values provide context for many of the experimental results presented in the following sections.

Calculation of the trapping parameters is carried out relative to the ^{87}Rb D_2 line. This is justified as the polarisability at the wavelengths in question is dominated by the D_2 line, not the case for the 1070 nm 1D lattice. The 1st order diffracted beam efficiency is taken to be 35% with a small 4% zeroth or-

λ (nm)	780.30		780.35		780.40	
	Bottom of overlap	Atom Location	Bottom of overlap	Atom Location	Bottom of overlap	Atom Location
T_d (μK)	149	108	81	60	56	41
Γ_{sc} (Hz)	11844	8618	3524	2564	1666	1212
ν_r (kHz)	149	121	110	90	91	74
ν_z (kHz)	299	266	221	197	184	164

Table 5.2: Theoretical trapping parameters for a 3D lattice. Comparison between the bottom of the lattice optical overlap volume (high intensity region) and the atom location nearer the top of the overlap volume (low intensity region) is made. Calculated for P=0.9 W, w_0=2.5 mm.

der reflection from the grating surface[38] also accounted for. Theoretical trapping parameters for the 2D and 3D lattice are presented in Table 5.2. This table also draws attention to the fact that the lattice structure, and therefore trapping parameters are not the same across its entire volume. To form the lattice a Gaussian input beam is diffracted upwards by the grating. The low intensity wings of the beam therefore form the top of the optical overlap volume. Conversely, the high intensity centre of the lattice beam is diffracted upwards, forming the bottom of the lattice optical overlap volume (see Figure 5.2). This results in a spread of trap depths across the size of the atom cloud. This spread can be reduced somewhat by using larger lattice beams, motivating the decision to use a beam with a $1/e^2$ radius of 2.5 mm in the following investigations.

To rule out the possibility that the observed atom clouds are in fact a far-detuned optical molasses held against gravity, a simple calculation of the optical molasses force is carried out. A 1D optical molasses consisting of a pair of retro-reflected beams of equal power, aligned in the gravity axis (see Figure 5.2) is modelled. This simplification overestimates the molasses force, providing additional confidence that the atoms are indeed localised due to the dipole force. For this calculation, each beam is assumed to have P =0.9 W, w_0=2.5 mm and a wavelength of 780.30 nm ($\Delta = -30$ GHz), the lowest detuning used throughout the lattice investigation. As the peak optical molasses force is a function of atom velocity (see Sec 2.4.1), an appropriate choice of the maximum atom velocity is required. For this calculation, a peak velocity of 0.2 m/s is selected. This is justified as this corresponds to the maximum velocity of an atom, initially at rest at the top of the MOT, reaches as it falls the e^{-2} diameter of the MOT (approximately 1.6 mm). Using Eq 2.24, the maximum acceleration provided by the optical molasses force is calculated to be 4×10^4 times lower than the accel-

eration due to gravity. This ratio increases to $8{\times}10^5$ for the farthest detuned lattice wavelength used in the experiment of 780.40 nm ($\Delta = -80$ GHz). Sub-Doppler cooling mechanisms can enhance the optical molasses force, however, this enhancement is not enough to explain the large discrepancy between the acceleration due to gravity and the peak acceleration from the optical molasses force. This can be seen by considering that the final temperature in an optical molasses arises due to a balance between heating and damping rates. The final temperature of atoms that have undergone sub-Doppler cooling is approximately two orders of magnitude lower than for Doppler cooling, while the heating rate due to scattering remains relatively constant. The damping rate, and therefore acceleration due to sub-Doppler cooling mechanisms must therefore similarly be around two orders of magnitude higher.

5.4 Experimental Realisation

As a basis for loading the optical lattice, 8×10^6 ^{87}Rb atoms are loaded into a GMOT and cooled to approximately 3 μK using a red molasses cooling stage, during which the MOT coils are tuned off. The MOT light intensity is stabilised with a PID system feeding back onto an AOM using a small pick-off of light so the MOT number remains constant shot to shot. A constant MOT atom number is of particular importance when performing the long modulation frequency scans when finding the lattice parametric resonances in Sec 5.7.

The chip is bonded to the open end facet of a rectangular cuvette vacuum cell using a UHV compatible epoxy (Epotek 353NDPK). Once the grating is in place, the epoxy is cured in an oven at 100°C for several hours before the cell is attached to the vacuum chamber, pumped down and baked overnight. This allows a base vacuum pressure at the 4×10^{-8} mbar level, as measured by MOT load curves. There was some concern during the pump down process that the pressure differential within and outwith the cell would lead to bowing of the 500μm thick silicon chip, affecting the diffracted beams or in a worst case scenario leading to failure of the vacuum. This effect was observed by Squires *et al.*,[123] however no deformation of the grating was observed here due to the grating chip having a much lower surface area and slightly increased thickness over that used by Squires *et al.* No degradation of the 100 nm aluminium grating coating was observed due to thermal effects of the high-power lattice beams, with up to 15 W of 1070 nm light with a spot size <1 mm incident on the chip for several seconds.

The decision to mount the chip in-vacuum was made to allow the lattice to form as close to the chip surface as possible with no glass interface. As the height the lattice forms above the chip is dictated by the beam diameter and diffraction angle, this allows a smaller beam waist to be used, relaxing the power constraints on the lattice beam. The location the MOT forms with respect to the chip can be controlled within the optical overlap volume of the grating by varying the null field position of the quadrupole magnetic field. This control is used to obtain good overlap between the MOT and optical lattice for a maximum number of atoms trapped in the lattice. It is worth noting that the weak trapping axis of the 1D lattice (i.e. radial direction) is aligned along the same axis as gravity, the trapping potential being high enough to support against this force.

Atom detection is achieved via fluorescence imaging onto a CCD camera sensor. The imaging system is aligned orthogonally to both the MOT/lattice beam and gravity (See Figure 5.2). An imaging system with a spatially selective focal plane, similar to Figure 3.6, is utilised to reduce background noise originating from scattered light. Additionally, a notch filter with a peak transmission centered around 780 nm is used when investigating the 1D 1070 nm lattice. For both the 1D and 3D lattice geometries fluorescence images are acquired after a short 1 ms time of flight following the extinction of the lattice beam. Unless otherwise stated, the presented error bars in the following data sets are standard deviations from a mean calculated by running the same experiment several times, typically around five.

5.5 Near-Resonant 3D

Due to available light sources during the investigation, a near-resonant cateye laser at 780 nm, amplified by a tapered amplifier is utilised throughout the 3D lattice studies. Wavelength tuning of this laser is possible over around ± 1 nm, allowing fine tuning of the lattice trapping parameters. A single-pass AOM is used for power modulation and beam shuttering, allowing up to ≈ 0.9 W at the atomic sample. Out of the tapered amplifier the laser beam is elliptical, with an aspect ratio of roughly 3:1. To correct this, two cylindrical lenses, L_1 and L_2, of focal length 50 mm and 100 mm respectively are used. A diagram of the 3D lattice beam optical set-up is shown in Figure 5.4.

After correction of the ellipticity the roughly collimated lattice beam is expanded by a factor of two using a Galilean beam expander to a final beam $1/e^2$

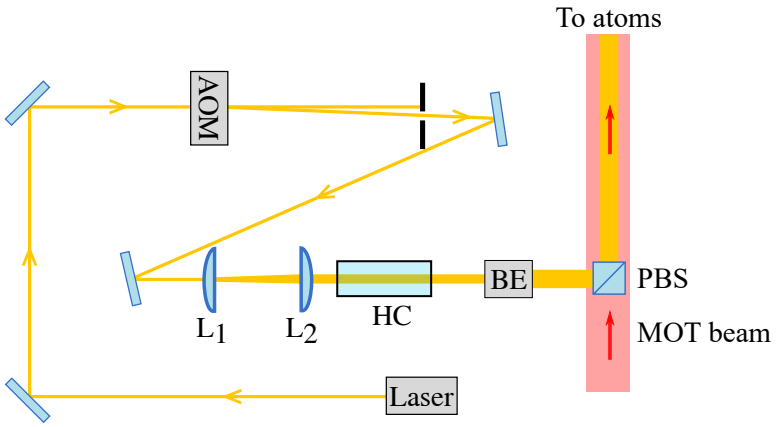

Figure 5.4: Simplified schematic of the 3D lattice optics set-up. HC: hot cell (discussed in Sec 5.5.1), BE: Beam expander PBS: polarising beam splitter. L_1 and L_2 are cylindrical lenses with focal lengths of 50 mm and 100 mm respectivley.

radius of $w_0 \approx 2.5$ mm. Images of the beam profile before and after the ellipticity correction and expansion are shown in Figure 5.5. This measurement of the beam profile was performed as close to the atomic sample as possible to ensure the measured profile is a good representation of that observed by the atoms.

The lattice beam is then combined with the MOT beam on a polarising beam splitter (PBS) and aligned onto all three regions of the grating chip in order to form the 3D lattice potentials (see Figure 5.2 (b)).

5.5.1 Optimising Near-Resonant Lattice

Atoms are loaded into the lattice by simply rapidly turning the lattice beam on while concurrently switching the molasses light off. Fluorescence images of the atoms after being held in the 3D lattice for various times are shown in Figure 5.6. As mentioned previously, all fluorescence images are taken after a short 1 ms time of flight with the lattice light extinguished. For lattice hold times <30 ms atoms that were not trapped in the lattice potentials are still within the image region of interest as they fall under gravity. These atoms are clearly visible in the long tail in integrated fluorescence in the y-axis of Figure 5.6. When no lattice beam is present the atomic cloud entirely leaves the imaging region after 40 ms, the presence of atoms after this time therefore is a clear indication of the formation of an optical trap.

One disadvantage of the ECDL lattice laser is the rather broadband amplified

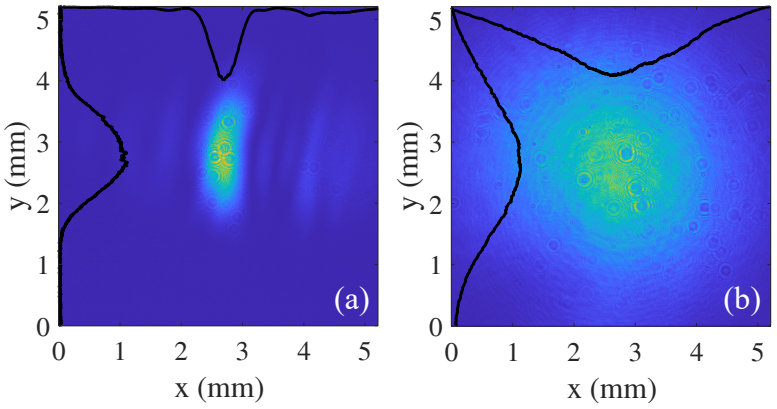

Figure 5.5: (a) 3D lattice beam profile before correction. (b) Final beam after expansion by telescope and ellipticity correction. Line profile through centre of beam is shown as black trace inset.

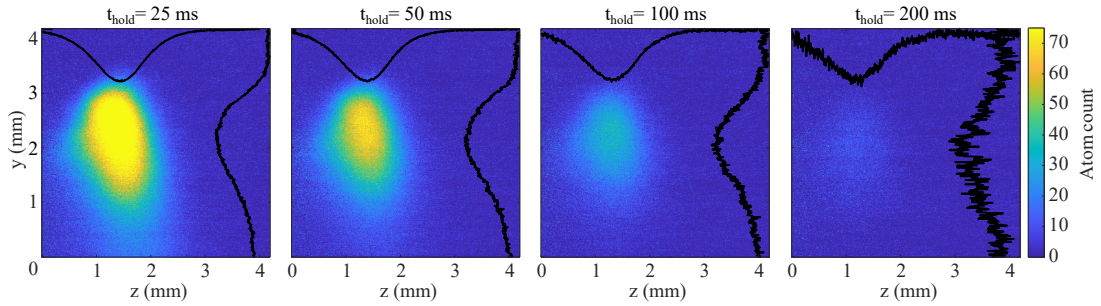

Figure 5.6: Fluorescence images taken after holding the atoms in the optical lattice for various times. Left to right t_{hold}={25, 50, 100, 200} ms, with corresponding atom numbers N={7.53, 4.73, 2.13, 0.69}$\times 10^6$. Black line profile insets indicate integrated fluorescence in each imaging axis. Data taken for 3D geometry, λ =780.30 nm (Δ=29 GHz), P=0.9 W, w_0 = 2.5 mm.

spontaneous emission (ASE) pedestal of the laser spectrum. Any light resonant with an atomic transition will result in photon scattering and a corresponding increase in the temperature of the atom, given by Eq 5.9. Due to the relatively shallow lattice potentials created here, this serves to "boil" hot atoms out of the trap. To reduce this effect, we spectrally filter the lattice beam through a 7.5 cm long Rb vapour cell[124] heated to approximately 70 C°. At this elevated temperature the high rubidium vapour pressure corresponds to a high absorption of light around resonance frequencies. As the ASE pedestal is several orders of magnitude lower in terms of optical power than the lasing mode, the ASE is largely removed while light at the frequency of interest is transmitted.

The ASE filtering using the hot Rb vapour cell was investigated by heating

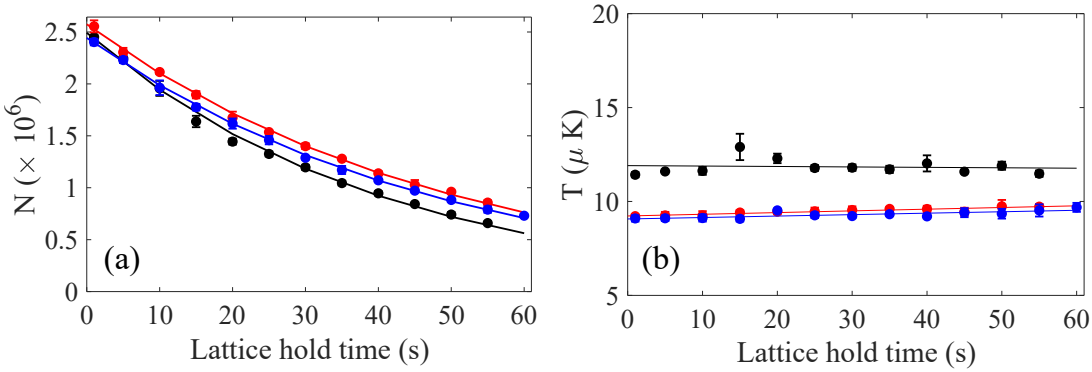

Figure 5.7: Hot cell ASE filtering varying cell temperature. Black data: T_{cell}=21 °C, τ =40 ms, $\frac{dT}{dt}$=-2.3 μK/s. Red data: T_{cell}=65 °C, τ =49 ms, $\frac{dT}{dt}$=9.0 μK/s. Blue data: T_{cell}=105 °C, τ =48 ms, $\frac{dT}{dt}$=7.6 μK/s. Data taken for 3D geometry, λ =780.35 nm (Δ=53 GHz), P=0.9 W and w_0 = 2.5 mm.

the cell to different temperatures and observing the effect on the lattice heating rate and lifetime. Where the lifetime is extracted from the time constant, τ, of a single exponential fit of form:

$$N(t) = N_0 \ \exp\left(-\frac{1}{\tau} \cdot t_{\text{hold}}\right). \tag{5.18}$$

The results of this are shown in Figure 5.7. It was found that the hot cell was effective at increasing the lattice lifetime and reducing the temperature of the atoms in the lattice when the cell is heated. The ASE filtering effectiveness seems to saturate at higher cell temperatures, however, as there is no large improvement in the lattice hold time or temperature when the cell is heated further, within the error of the results. This was taken to indicate the hot cell is working as effectively as possible and there is no additional benefit to heating beyond 65 °C.

Both ramping the lattice on and cooling into the lattice by switching the lattice beam on during molasses were found to have little effect on the temperature and number of atoms trapped in the lattice. This was investigated by varying the time overlap between the lattice and molasses stages as shown in Figure 5.8. From this figure we see a flat dependence on both the number of atoms in the lattice and the atomic temperature after a 35 ms hold time in the lattice. Fitting to the temperature as a function of the lattice-molasses overlap shows no change in temperature over this overlap time. The lack of any increased cooling is likely due to the large light shifts produced by the near-resonant lattice beam, perturbing the atomic energy levels so molasses is less efficient.

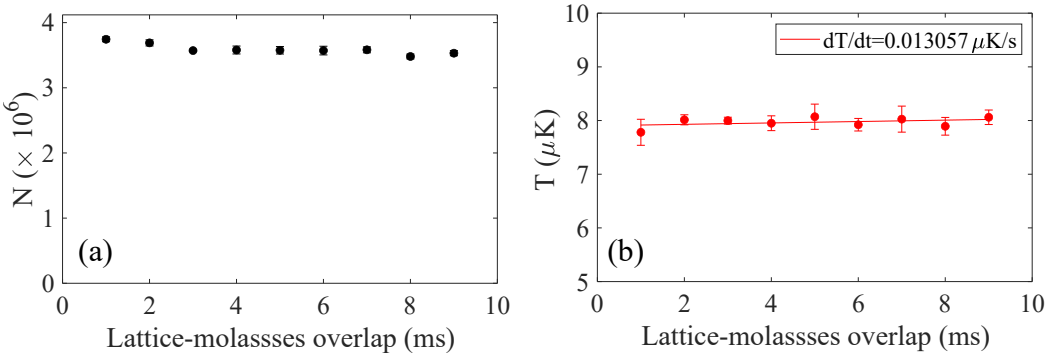

Figure 5.8: Overlapping molasses and lattice sequence. Data taken after a constant 35 ms total lattice time and 1 ms TOF. (a) Atom number as a function of the time overlap. (b) Atom temperature as a function of the time overlap. Red line is linear fit to data. Data taken for 3D geometry, λ =780.35 nm (Δ=53 GHz), P=0.9 W and w_0 = 2.5 mm.

5.5.2 Near-Resonant Lattice Lifetime

After optimisation of the experimental sequence, the lattice lifetime is measured as a function of the lattice wavelength, excluding points where $t_{\text{hold}} < 0.15$ s. This exclusion is justified by observing the change in slope in Figure 5.9 around this time and corresponds to the thermalisation of atoms within the potentials with atoms hotter than the trap depth being ejected from the imaging region over this time scale. Lattice lifetimes extracted from Figure 5.9 are also presented in Table 5.3.

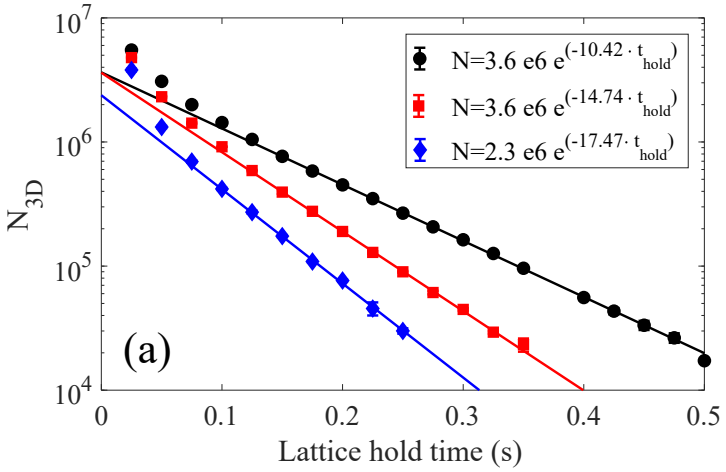

Figure 5.9: 3D lattice lifetime as a function of lattice wavelength, taken for P=0.9 W, w_0 = 2.5 mm. Black circles λ=780.30 nm (Δ=29 GHz), Red squares λ=780.35 nm (Δ=54 GHz), Blue diamonds λ=780.40 nm (Δ=78 GHz).

The atomic scattering rate scales as I/Δ^2, as shown in Eq 5.10, therefore one would expect greater lattice lifetimes the further red-detuned the lattice beam becomes. The data presented in Figure 5.9 shows this is not the case where the best lifetime of 95 ms is observed when $\lambda = 780.30$ nm, i.e. a detuning of 60 pm (29 GHz) from the strongly interacting D_2 line. Shorter lifetime for larger detunings was initially attributed to the decreasing trap depth which scales as I/Δ. Due to the maximum available power from the lattice laser it is not possible to simply increase the power to maintain the same trap depth (see Table 5.2 for calculated scattering rates and trap depths). At large detunings the trap depth decreases, allowing atoms to be ejected from the trap even at relatively low temperatures. This effect becomes evident when plotting atom number and temperature as a function of lattice hold time for the same wavelength, varying the optical power as shown in Figure 5.10. From Figure 5.10 (b) we see that the atomic temperature steadily increases asymptotically up to some value after which the temperature decreases.

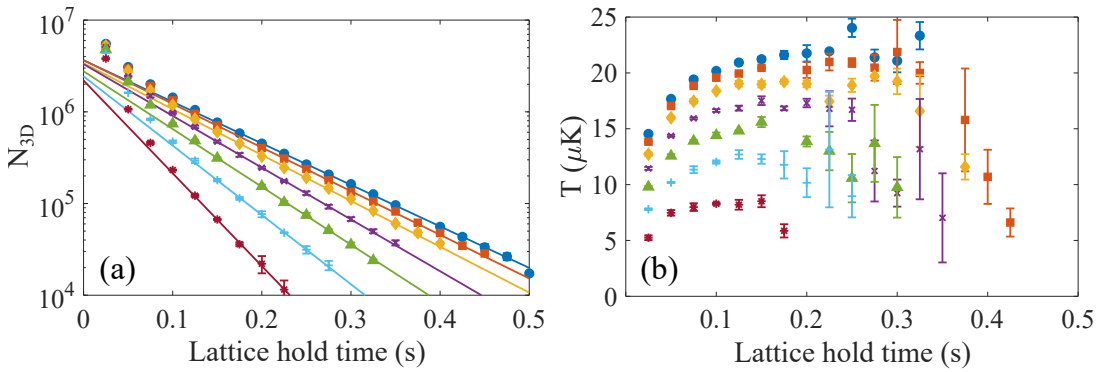

Figure 5.10: Lattice lifetime and temperature varying lattice beam power. Data taken for 3D geometry, λ =780.30 nm (Δ=29 GHz), $w_0 = 2.5$ mm, lattice beam powers top to bottom are P={0.87, 0.81, 0.74, 0.64, 0.52, 0.40, 0.28} W. The corresponding lattice lifetimes are τ={96, 91, 87, 77, 69, 57, 43} ms. For convenience, the theoretical trap depths at the associated lattice beam powers are T_D ={104, 97, 88, 77, 62, 48, 33 } μK.

By comparing to the theoretical trap depth, defined as the lowest potential energy in the lattice, to the asymatotic roll-off temperature taken from Figure 5.10(b), the asymptotic temperature in the lattice is found to be a factor of four smaller than the theoretical trap depth at the atom location near the top of the lattice overlap volume and a factor of six lower than the trap depth at the bottom of the lattice overlap volume. Both the extracted lifetime and this roll-off

as a function of theoretical trap depth are plotted in Figure 5.11.

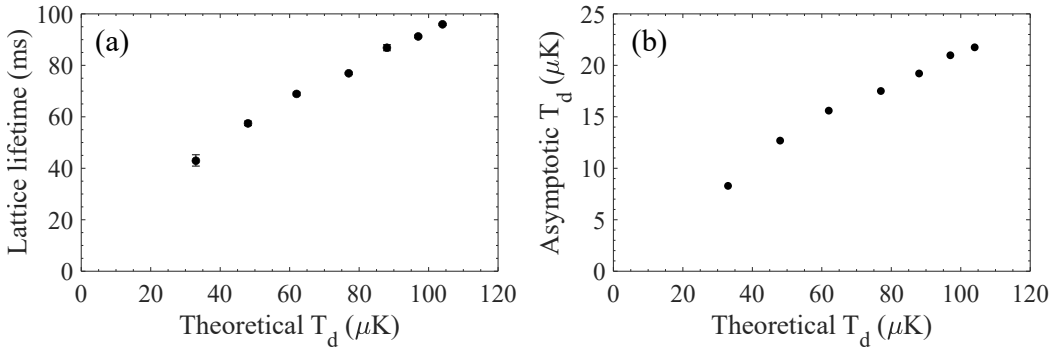

Figure 5.11: (a) Measured lattice lifetime as a function of theoretical trap depth. (b) Asymptotic atom temperature as a function of theoretical trap depth. Theoretical trap depth calculated at the atom location for λ=780.30 nm, P=0.9 W, w_0 =2.5 mm.

This lower maximum measured temperature in the lattice is to be expected as the temperature measured by the TOF imaging is a statistical average of the cloud temperature as given by the Maxwell-Boltzmann velocity distribution,[43]

$$f(v) = 4\pi v^2 \sqrt{\left(\frac{m}{2\pi k_B T}\right)^3} e^{-\frac{mv^2}{2k_B T}}. \tag{5.19}$$

At any given measured temperature therefore, many of the atoms in the lattice potential are actually hotter than the measured temperature, allowing these atoms to escape over the trapping potential. This effect is highlighted in Figure 5.12 where the high velocity tail of the distribution can be seen to be at energies greater than the trap depth, allowing these atoms to escape. The measured difference between the roll-off temperature and the trap depth of 1/4 to 1/6 approximately obeys an often quoted scaling law that estimates the atomic temperature to be $T_d/10$.[125]

The reduction in temperature after reaching the roll-off point is an effect similar to evaporative cooling where the hottest atoms have left the trapping volume. This leaves a truncated portion of the Maxwell-Boltzmann energy distribution, as highlighted in Figure 5.12. When the remaining atoms are imaged, the now truncated velocity distribution is observed as a spatial distribution of fluorescence that can be approximated as a Gaussian with the mean measured temperature shifted slightly due to the missing portion of the distribution. This effect is not evarporative cooling due to the lack of re-thermalisation of the atoms, a result of the lattice occupancy per site being $<< 1$.

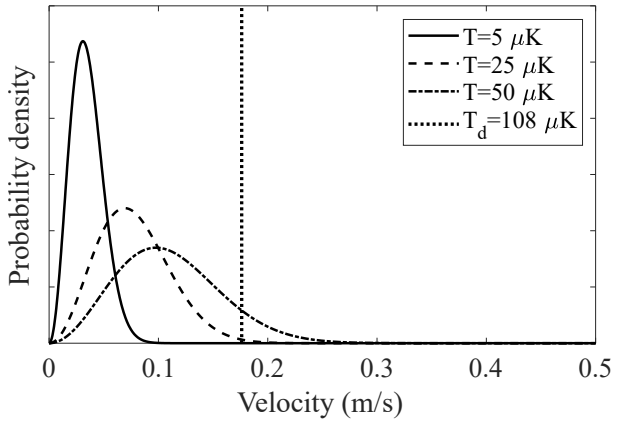

Figure 5.12: Atomic velocity probability distribution for different measured atomic temperatures. Vertical dotted line indicates the velocity associated with a trap depth of 109 μK as for the λ =780.30 nm, P =0.9 W 3D lattice.

An estimation of the theoretical trap lifetime can be made by considering the number of atoms at any particular time with velocities less than the velocity associated with the trap depth. Given an initial atom temperature, $T_0 = 5$ μK, and a linear heating rate given by Eq 5.9, the velocity distribution of the atoms at a particular time, t, can be found using Eq 5.19. By integrating Eq 5.19 between $v = 0$ and $v = v_{trap}$, where v_{trap} is the maximum atomic velocity trappable by the lattice potential, it is possible to find the number of atoms moving with $v \leq v_{trap}$ at any particular time. The 1/e lifetime can then be extracted. A comparison between the theoretical and experimentally measured trap lifetime is made in Table 5.3. From this table we see a reasonable agreement for the lowest lattice detuning at λ=780.30 nm. As the detuning is increased however the lifetime should go up due to the reduced scattering rate. Observations in the experiment indicate this is not the case however, as increased detunings result in lower lifetimes. This was initially attributed to the reduced trap depth; however this effect alone is not enough to account for the reduced lifetime. The reasons for the reduced lifetime are therefore not well understood but could be due to additional heating mechanisms, such as laser intensity noise[126], not accounted for by the scattering rate as calculated by Eq 5.10. As the detuning is increased, decreasing the scattering rate, the unaccounted for heating could begin to dominate, skewing the measured lifetimes.

Wavelength (nm)	Lifetime theory (ms)	Lifetime experiment (ms)
780.30	150	95±1
780.35	270	68±1
780.40	380	57±2

Table 5.3: Theoretical near resonant 3D lattice $1/e$ lifetimes compared to experimentally observed $1/e$ lifetimes. P=0.9 W, w_0=2.5 mm. Errors are calculated from the 1σ confidence level of the exponential fit (Eq 5.18) to the data.

5.6 Far-Detuned 1D

To form the far-detuned 1D lattice a 1070 nm ytterbium fibre laser is used with a single-pass AOM for power modulation and beam shuttering. This provides 10 W of laser light at the atom location. The beam waist is focused to 80 μm using two plano-convex lenses, L_1 and L_2, of focal length 50 mm and 150 mm respectively. The position of the focus along the beam propagation axis is controlled by placing L_1 on a translation stage. Separation of the lenses is optimised such that the minimum beam waist is approximately at the grating location. The linearly polarised light is then combined with the MOT light on a dichroic mirror and aligned onto the grating chip. A simplified schematic of this set-up is shown in Figure 5.13.

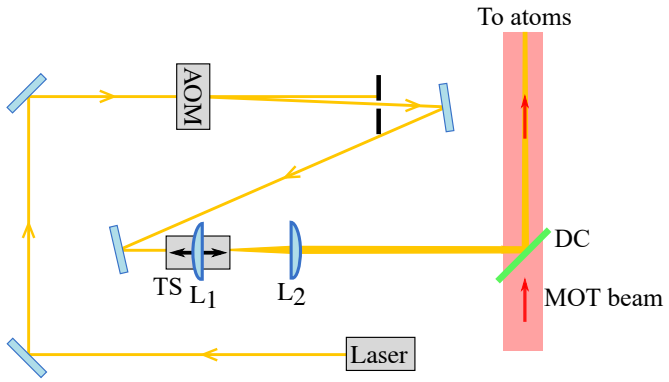

Figure 5.13: Simplified schematic of 1D lattice optics set-up. L_1 and L_2 are plano-convex lenses with focal lengths of 50 mm and 150 mm respectively. L_1 is placed on a translation stage, TS, to control the position of the beam focus. MOT and lattice beams are combined on DC: dichroic mirror.

Atoms are loaded into the 1D lattice by rapidly switching the lattice beam on

at 10 W at the beginning of the red molasses cooling stage. Contrary to the near-resonant lattice this was found to slightly improve the temperature and number of atoms in the lattice as the atoms are being cooled into the lattice potentials. This beam is aligned onto the grating to give the best optical overlap between the lattice and the MOT volume, maximising the number of trapped atoms in the lattice.

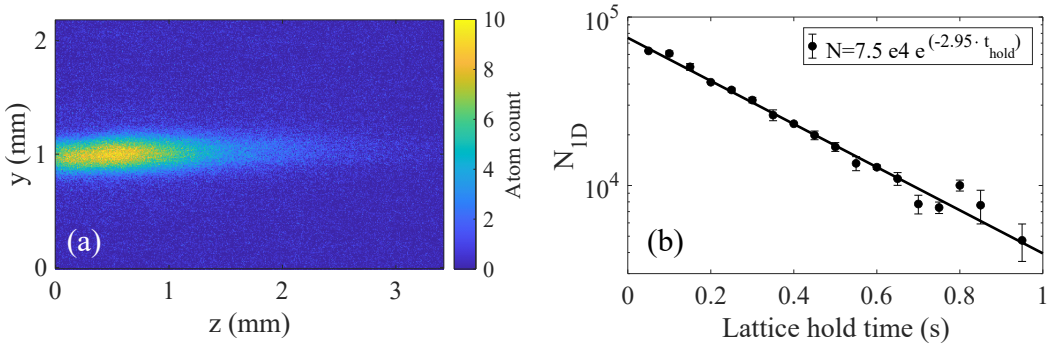

Figure 5.14: (a) Fluorescence image of 1D lattice taken after a lattice hold time of 50 ms. Colour bar is scaled in terms of number of atoms using the calculated atomic scattering rate and collection efficiency of the imaging system. (b) 1D lattice atom number as a function of hold time.

A plot of the 1D lattice lifetime along with an image of the lattice is shown in Figure 5.14. As with the 3D lattice, atoms are visible in the imaging region for times far in excess of that possible if there was no lattice beam present. While direct imaging the lattice sites is not possible due to the lattice spacing and the resolution of the imaging system, the images match well with the expected spatial distribution of atoms. A simple calculation of the expected spatial distribution of atoms in the y-axis is carried out using Eq 3.8. Given the lattice beam $1/e^2$ diameter, atomic temperature and 1 ms time of flight along with the 150 μs imaging time, the expected cloud width in the y-axis is calculated to match well with the experimentally measured cloud width seen in Figure 5.14(a).

From the fit in Figure 5.14(b) we see a lifetime of 340 ms, far in excess of the best near-resonant 3D lattice by a factor of 3.6. Scattering in this far-detuned case is kept to a minimum, calculated at around 4 s^{-1}, resulting in a consequentially low heating rate of 0.7μK/s. Given an initial temperature of 25 μK, atoms could therefore survive in the trap for >1000 s if scattering was the only limit to the lifetime. The initial lattice temperature was estimated by holding the atoms in the lattice for various times and measuring the temperature after the lattice beam

is extinguished via the time of flight method. It is then possible to extrapolate back to a hold time of 0 ms.

In reality, the lattice lifetime is currently limited by collisions with thermal background gasses in the vacuum. This was confirmed by reducing the alkali dispenser current and measuring the lattice lifetime as shown in Figure 5.15. This plot reveals that as the dispenser current, and therefore background vapour density, is dropped the lifetime increases. If cold-atom collisions were the dominating factor to the reduced lifetime, a deviation from the exponential decay shown in Figure 5.14(b) would be apparent as more cold atoms are ejected from the trap. As this deviation is not observed, the limit to the lifetime can be attributed to thermal background atoms. Dropping the dispenser current below the level shown here results in a reduced atom number in the MOT and therefore lattice. It would be possible to increase the lifetime further by reducing the base vacuum pressure. This could be accomplished by several means; the most simple of which being a longer and hotter vacuum bake out to reduce contaminants within the chamber. Alternatively, a more complex loading scheme such as from a 2D MOT[82] or temporarily increasing the alkali density during the MOT load phase using light-induced atomic desorption (LIAD)[127] could be investigated. As this is very much a proof of principle experiment however, this was deemed unnecessary.

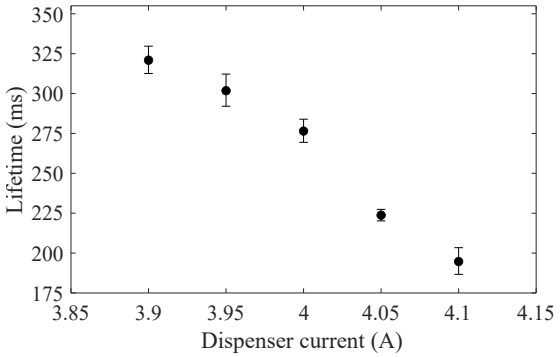

Figure 5.15: Plot of lattice 1/e lifetime varying dispenser current. Error bars show 1σ confidence bound of the exponential fit to lifetime data.

An estimation of the background pressure is made using the known relation between vacuum pressure and trap lifetime of 10 s at a pressure of 7×10^{-10} mbar.[39,128] This yields an estimated vacuum pressure of 2×10^{-8} mbar, consistent with that measured by both MOT load curves (4×10^{-8} mbar) and the ion pump gauge ($\approx 1 \times 10^{-8}$ mbar).

5.7 Parametric Oscillations

While the long hold time of the atoms, far in excess of that possible if they were in free fall is encouraging evidence of the formation of an optical lattice, it is not in and of itself proof. To provide additional evidence, parametric resonances at the lattice trapping frequencies are investigated.[129,130] This technique relies on modulating the lattice potentials; when the frequency of this modulation is equal to $2\nu_{\text{trap}}$, atoms will be excited parametrically to higher vibrational states of the trapping potential. Eventually the atom is excited to such an extent that it is ejected entirely from the trapping potential. This process can be easily observed experimentally by an increase in cloud size, correlating to the atoms entering higher vibrational states, or a drop in atom number as atoms are eventually ejected from the trap. In addition to the fundamental parametric resonance at $2\nu_{\text{trap}}$, sub-harmonics can also be excited at frequencies given by $2\nu_{\text{trap}}/n$, where n is an integer.[129]

Modulation of the trapping potentials can be accomplished in several ways; through modulation of the phase, polarisation or intensity of the lattice beam. Modulation of the intensity was selected in this case as it is trivially accomplished using the AOM already used for beam shuttering. The frequencies of interest are in the regime 100 Hz - 100 kHz, easily achievable with standard AOM crystals. This modulation is applied by modulating the RF drive power of the AOM through a double balanced mixer. A function generator outputting a gated modulation was set up to communicate with the experimental control program based in LabVIEW. This allowed the modulation to be applied for arbitrary times with computer controlled modulation depths. The modulation frequency was also controlled through LabVIEW, allowing large modulation frequency scans to be carried out while searching for the parametric resonances. These scans were randomised to ensure any observed trends were not a result of the experimental conditions drifting during the rather long scan duration.

3D Lattice

A typical parametric resonance plot for the 3D lattice is shown in Figure 5.16 for a single lattice wavelength and optical power. These data were obtained by holding atoms in the lattice with no modulation for 50 ms, followed by 50 ms of gated sinusoidal modulation applied to the lattice beam power with a modulation depth of around 12%. The initial lattice hold time with no modulation allows

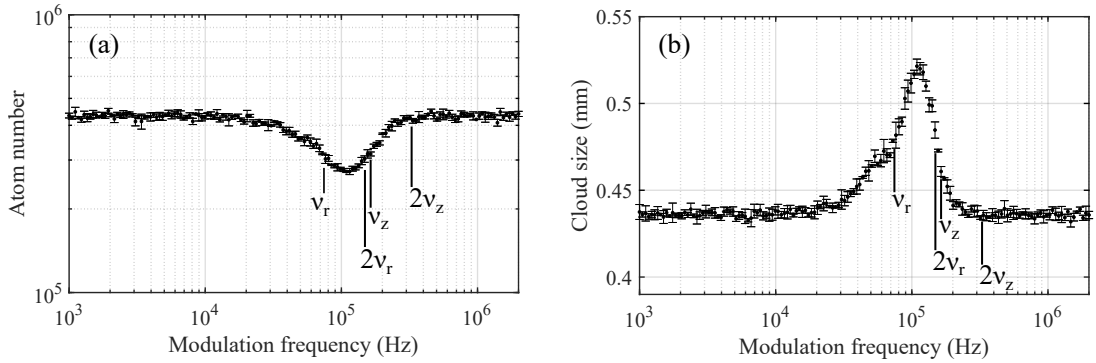

Figure 5.16: Atom number (a) and cloud width (b) as a function of lattice modulation frequency for the 3D geometry. Theoretically calculated trap frequencies are also marked. λ=780.40 nm, P=0.9 W, w_0=2.5 mm.

atoms that are not trapped by the lattice potentials to exit the imaging region in addition to allowing thermalisation of the atoms within the lattice sites. It is possible to observe the resonant heating of the atoms by a change in either the atom number or width of the atomic cloud after time of flight, extracted from the fluorescence images. From Figure 5.16 we see clear peaks in both the atom number and width of the cloud at the same modulation frequency, around 111 kHz. Expected trap frequencies in both the radial and axial direction (quoted in Table 5.2) are also marked on this figure, calculated at the MOT location in the lattice overlap volume.

The plots in Figure 5.16 show a broadening of the resonance, biased towards lower frequencies. This is to be expected as the calculated trap frequencies are based on the peak trap beam powers. Broadening in this manner is due to the Gaussian nature of the input and diffracted beams causing a spread of light intensities across the lattice structure. As a result, many of the trapping potentials formed are shallower than the peak depth seen at the centre of the beams. As $\nu_{\text{trap}} \propto \sqrt{\Delta E_i}$ this creates a broadening of the resonance biased towards lower frequencies. This effect is especially apparent when looking at the cloud width, seen in Figure 5.16 (b), where a sharp drop in cloud width at higher modulation frequencies and a long decaying tail towards the low frequencies is observed.

Another interesting feature of this plot is the distinct shoulder on the resonance peak at the low end of the frequency spectrum. This shoulder was found to resolve into a second resonance peak when the trap depth was lowered, shown in Figure 5.17. The modulation time and depth were kept constant throughout to ensure a fair comparison. Once resolved, the second peak can be seen to occur at

half the frequency of the main peak and corresponds to the parametric excitation subharmonic at the resonant trap frequency,[129] i.e. ν_{trap}. The resolution of the second peak at lower trap depths is attributed to the fact that as the trap depth decreases, atoms at the edges of the Gaussian beam are hot enough to escape the lower lattice potentials. This leaves only atoms in the deepest regions of the lattice, reducing the spread in trapping potential across the atom cloud. The spread in trap resonance frequencies is also therefore reduced and a second peak becomes visible at lower modulation frequencies.

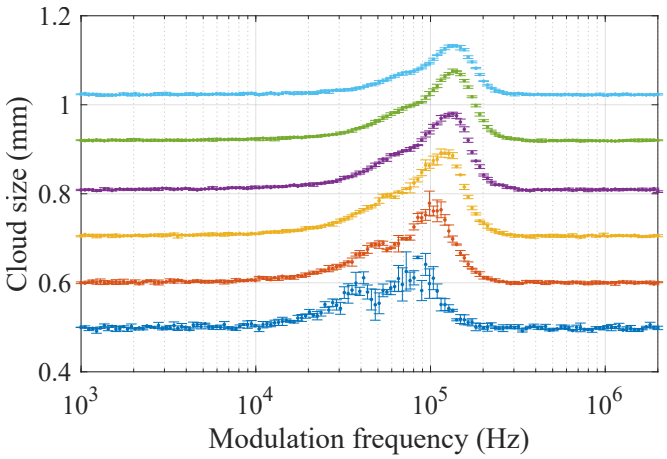

Figure 5.17: Example plot of the subharmonic resonance peak resolving at lower trap depths. Plots are offset vertically for clarity with the deepest trap plotted at the top of the figure. λ =780.35 nm, w_0 =2.5 mm.

A good agreement between the theoretical 3D lattice radial trap frequency at $2\nu_r$ and its subharmonic at ν_r and the observed resonances is found. For the data presented in Figure 5.16 the experiment and theory are found to differ by only a factor of 1.3. Curiously no axial resonance at ν_z and $2\nu_z$ is observed on these resonance plots.

By plotting the measured peak resonance frequency as a function of $P/|\Delta|$ all the lattice parametric resonance data can be analysed as a single trend where $2\nu_r = \sqrt{A\frac{P}{|\Delta|}}$ with A being some constant. The peak resonance frequency was extracted by fitting to the parametric resonance data and extracting the peak frequency from the fit.

When A is extracted from the experimental fit and compared to the theoretically calculated value it is once again found that the experimental data agrees well, within a factor of 1.6. Similar discrepancies between experiment and theory have have been found in previous publications where a ratio between theory and

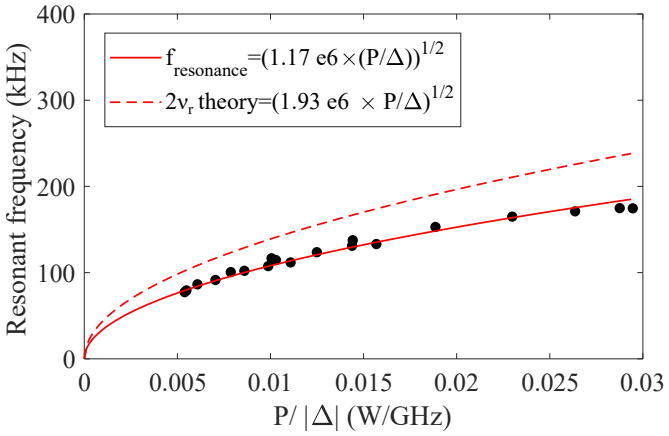

Figure 5.18: Measured trap frequency plotted as a function of $P/|\Delta|$. Black points are experimentally measured data. Solid red curve is experimental fit to the data. Error bars (smaller than shown data points) are extracted from the 1σ confidence bound of the fit to the parametric resonance peak. Dashed red curve indicates the theoretically calculated resonance frequency.

experiment of 1.1 to 1.65 has been quoted, found across several separate experiments.[130] Currently, the theoretical description of the lattice does not include light polarisation of either the input or diffracted beams, a fuller description of the light potentials in the theoretical model could therefore help reconcile the remaining difference between the theory and experiment.

1D Lattice

Figure 5.19(a) shows a plot of the atom number as the trap modulation frequency is scanned. As the initial atom number is significantly lower than the 3D lattice geometry, high SNR measurements of the atom number are made slightly more difficult. The increased lattice lifetime compared to the 3D lattice does however allow the modulation to be applied for longer (100 ms vs 50 ms in the 3D case) after a 50 ms hold with no modulation as before. Shaking the lattice for longer should give a higher resolution on the parametric resonance feature. No cloud width data is presented here due to the increased noise when fitting to the rather small number of atoms present in the 1D lattice, although this could be improved by increasing the collection efficiency of the imaging system. Expected resonance frequencies (summarised in Table 5.1) are also shown on this plot for comparison. Clear features are observed at 500 Hz and 250 kHz, with more subtle features discernible at 1.1 kHz and 600 kHz, corresponding to ν_r, ν_z, $2\nu_r$ and $2\nu_z$ respec-

tively. These features match reasonably well with the theoretically calculated axial resonance features at $2\nu_r$=2.7 kHz and $2\nu_z$=898 kHz. Broadening of the resonances is again observed, biased towards lower modulation frequencies due to the Gaussian nature of the trap beam. This broadening due to a spread in observed trap frequencies by the atoms also explains the rather poor resolution of the two axial resonances in this case.

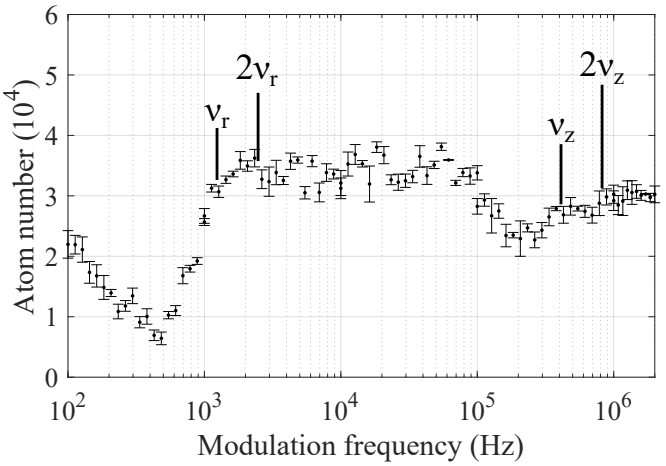

Figure 5.19: Atom number as a function of lattice modulation frequency for 1D lattice geometry showing clear resonances at ≈500 Hz and ≈250 kHz. λ=1070 nm, P=10 W, w_0=80 μm.

The exact beam diameter at the location of the atoms plays a large role in the expected trap depth and resonances. If for example, the resonance frequencies are calculated for the same beam conditions for a 120 μm beam instead of 80 μm, the expected frequencies are ν_r=0.6 kHz and ν_z=275 kHz, matching the experimentally observed resonances extremely well. While precautions were taken to ensure the beam waist at the atoms is known well it cannot be directly measured at the atom location. In place of a direct measurement, the beam diameter is measured several times, translating a beam profiler along the propagation axis. Using Gaussian optics the diameter of the beam at the atom location can be inferred. In addition to this, the beam profile at the same working distance as the atomic sample was measured by altering the beam path. The combination of these measurements gives some confidence in the stated value, however, the exact beam diameter still constitutes a primary source of error when comparing the experiment to theory in the tighter beam geometry of the 1D lattice.

The primary objective in undertaking these resonance scans was to rule out the possibility the atoms are held in place by a simple dipole trap as opposed to

a 1D lattice (the diffracted beam geometry and position of cold atoms precludes the formation of higher dimensional lattices at this wavelength). This experiment has been successful in that regard as clear resonances at frequencies far in excess of a dipole trap are observed, matching reasonably well to those theoretically calculated.

5.8 Conclusions and Outlook

To conclude, a proof-of-principle experiment investigating the loading of optical lattices formed from a single diffractive optic, directly from a GMOT formed from the same optic has been detailed. By aligning to different regions of the grating chip along with selecting an appropriate lattice wavelength with respect to the grating period, a single GMOT chip provides enough flexibility to produce phase-stable 1D, 2D and 3D lattice geometries with a single input beam. This method requires minimal effort and reduced alignment constraints when compared to traditional methods. While it is difficult to categorically prove the presented data are a result of the formation of optical lattices, current evidence points towards the successful demonstration of 1D and 3D optical lattices. Loading into a 2D lattice from the same chip should also be possible if transport of the cold atom cloud from the MOT region to the 2D lattice region is accomplished, perhaps by an intermediate optical trap or more appealingly, an on-chip magnetic trap.

Due to available equipment the 3D lattice geometry is formed using near-resonant, light red detuned by at most 0.16 nm (78 GHz) from the D_2 line. While this near-resonant case is not ideal given the high atomic scattering rate and therefore heating rate at this wavelength, traps with 1/e lifetimes of up to $\approx$100 ms were demonstrated. In addition to this, a far-detuned 1D lattice was also formed using the reflected portion of a 1070 nm beam that due to the period of the grating is minimally diffracted by the grating chip. The much reduced scattering rate of this far-detuned light allows for increased 1/e trap lifetimes of 340 ms, limited by background vacuum pressure which is measured by MOT load curves at the 4×10^{-8} mbar level.

To provide additional evidence of the formation of these optical lattices, parametric resonances at the lattice trapping frequencies have been excited by modulating the lattice depth. Observed resonances agree reasonably well with theoretically calculated values for both the 1D and 3D case.

This experiment has been carried out in ^{87}Rb due to readily available equip-

ment within the department. With an increased focus on portable alkaline-earth optical clocks however, this technique should be readily extendable to other elements such as Sr. Recently S. Bondza *et al.* demonstrated two colour cooling of Sr in a GMOT.[46] To reduce zeroth order diffraction from the grating chip a hole was introduced in the centre of the chip, below the MOT location. If instead the grating hole was replaced by a dielectric reflector tuned to allow the transmission of cooling light (460 nm and 689 nm) and reflect the magic wavelength lattice light (813 nm)[10] for the formation of a 1D lattice, a very compact and mechanically robust optical clock physics package could be created. A similar architecture has been demonstrated using a dielectric patterned on an atom chip, however this system used microfabricated optics bonded to the chip surface to create a 3D lattice.[115] This could similarly be achieved by utilising a grating with a period 689 nm $<$ d $<$ 812 nm if the optical forces generated by the diffracted MOT beams are suitable for the MOT cooling stage.[47]

The lattice structure generated using the grating chip is entirely controlled by the wavelength of lattice light and grating design. This reduces the degrees of freedom available when investigating more complex lattice structures where it may be advantageous to tune the trapping potentials using independent beams. This sacrifice in lattice tunability is a direct consequence of the increased phase stability afforded by each beam originating from a singular input beam. In future it may be interesting to investigate other GMOT chip designs, producing different lattice structures, such as "quad" gratings where the chip is broken into four sections as opposed to three or "checkerboard" gratings where the chip consists of a 2D grating structure.[34] Checkerboard gratings have the advantage that the MOT tends to form with a larger atom number, closer to the chip surface, ideal for loading into the lattice potentials.

Chapter 6

Compact Cold Atom Microwave Clock

The following chapters will discuss the realisation and optimisation of a cold-atom microwave clock. As with the rest of this thesis the focus here is on compact components, allowing a reduced form factor compared to traditional technologies. To that end, we work in collaboration with Gaetano Mileti's group in Neuchâtel University, in particular Etienne Batori, who designed the final compact microwave cavity used throughout this work.[131] In addition to designing the final cavity, Etienne aided with the early characterisation of the clock set-up during a visit to the University of Strathclyde, his advice proving invaluable during this stage.

Work presented in this and the following chapter is largely based on that published in Ref[132] and Ref[133] with much of the data and conclusions drawn also presented in these publications. All data presented was collected by the author, the Zeeman spectroscopy data of Sec 6.4.5 was jointly collected with Etienne Batori. The clock optics and vacuum system were designed and built by Ben Lewis with minor improvements carried out by the author.

6.1 Brief Development of Microwave Clocks

The first atomic frequency standard to outperform traditional quartz oscillators was a caesium (Cs) beam clock developed at NPL.[134,135] While much development of microwave clocks has been undertaken since, the basic principles behind microwave atomic clocks (state selection, microwave interrogation and finally state read out) have remained largely unchanged since their inception.

Atomic beam clocks typically use permanent magnets to only allow atoms in

the correct initial clock state to pass into the microwave cavity region. This is quite a lossy process as most of the atoms are initially in the wrong ground state for clock interrogation and therefore never interact with the microwave field.[135] Lamp pumped rubidium atomic frequency standards (RAFS) offer an advantage over magnetic state selection as the atoms can be actively driven into the correct ground state using a combination of a Rb discharge lamp and a filter cell.[136] State read out is performed by measuring the relative absorption of light from the discharge lamp by a photodetector.

One large fundamental improvement that has allowed the performance of microwave atomic clocks to be pushed to ever increasing stabilities has been the integration of diode lasers for state preparation and read out. Additionally, the preparation of cold, dense atomic clouds is only made possible through laser cooling and has allowed first the development of fountain clocks[11] and more recently optical lattice clocks.[10] Lasers offer a significant advantage over discharge lamps for optical pumping and state read out in that they have very well defined and narrow emission frequencies compared to the rather broadband emission of discharge lamps.[1] Not only does this improve optical pumping for a larger signal but higher signal to noise measurements of the final atomic state are also possible due to the reduced background on the detector from non-resonant light. The photon flux of lasers is also significantly higher, increasing the light-atom interaction, assuming the laser frequency is well locked to the atomic transition.

6.2 Pulsed Optically Pumped Atomic Clocks

To fully leverage the benefits of using lasers in compact microwave clocks the pulsed optically pumped (POP) scheme is often used.[137–139] Here the atomic sample (thermal or cold-atoms) is optically pumped into a single initial atomic ground state by a laser pulse. Typically a Ramsey-type interrogation is then employed, interrogating the atoms with two $\pi/2$ microwave pulses of length t_m separated by a Ramsey time, T_R, while the laser light is off. Finally, the resulting atomic populations are read out optically by another laser pulse and the cycle repeated. This scheme (shown in Figure 6.1) offers significant advantages over CW microwave clocks and coherent population trapping (CPT) clocks as no optical fields interact with the atoms during the microwave interrogation time, ensuring negligible light-shifts on the clock transition and improving the stability of the resulting frequency standard.

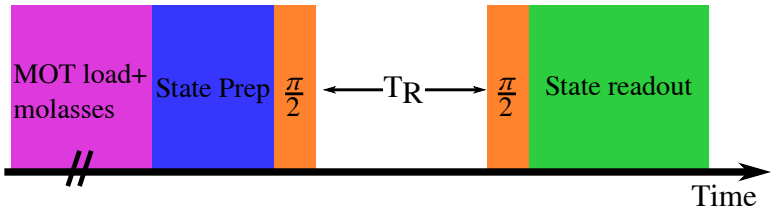

Figure 6.1: Block diagram of basic timing sequence for cold-atom POP clock. Time axis not to scale.

The development in the last decade of pulsed optically pumped (POP) clocks in thermal vapours has driven new research, with state-of-the-art stabilities.[137,139,140] However, these clocks still suffer from buffer gas shifts, providing the ultimate limitation to their long-term stabilities. Achievable Ramsey times within these systems are also limited to a few ms by spin relaxation of the thermal atoms,[137,141] restricting the short-term stability performance.

In an effort to combat these limitations several groups have now developed compact cold atom microwave clocks based on spherical optical-integrating sphere cavities,[142,143] cylindrical cavities[144,145] and more recently loop-gap-resonator cavities.[146] Three examples of cold atom microwave clocks are now even commercially available.[147–149] Different laser cooling schemes with varying optical geometries have been used within these systems, with isotropic cooling of an optical molasses,[142,143,145,147] pyramid MOTs[150] and larger traditional 6-beam MOTs[144,146] all being utilised.

In this project we aim to develop a compact cold-atom POP clock in collaboration with Neuchâtel University who have significant expertise in vapour-cell microwave clocks.[139,151–154] Neuchâtel University have designed and built a custom loop-gap-resonator microwave cavity that will enclose a GMOT chip in order to prepare cold atoms, with the experiment being housed in the University of Strathclyde. The eventual performance goal of this system is to be competitive with commercial MASER stabilities in the short-term and medium-term. Current commercial MASER offerings exhibit a 1 s fractional frequency stability at the 10^{-13} level, averaging down to 10^{-15} after 10,000 s.[155] While exhibiting excellent performance, MASERs tend to drift in the long term. In time it should be possible to drive the stability of our system to MASER levels in the medium-term with improved drift in the long-term in a package of a few litres. As a first proof of principle, no effort was made towards a compact set-up, outwith the design of the cavity itself. In addition to this, generation one of the clock does not include

magnetic shielding, strongly limiting the potential long-term stability. Future generations of the experiment will likely focus on integration of the vacuum system and reducing the size of the optical set-up while also working towards a good long-term performance and improved short-term stability.

6.3 Loop-Gap Resonator Type Cavities

As I played no part in the design of the microwave cavity, its discussion here will be kept brief. In contrast to traditional microwave resonators producing a standing wave with a wavelength largely defined by the internal dimensions of the cavity, a loop-gap-resonator (LGR) type cavity is used here. This structure allows one to create resonators with internal dimensions smaller than the wavelength of the desired microwave field, mainly through manipulation of the electrode geometry.[139,152] A schematic of the LGR cavity is shown in Figure 6.2. The cavity operates in a TE_{011}-like mode along the cylindrical symmetry axis (in the following this is referred to as the cavity axis). Measurements by Neuchâtel collaborators indicate a quality factor of Q≈360[132] with a central frequency tuned around the groundstate splitting of ^{87}Rb. While the quality factor is modest, this actually aids with clock operation by reducing cavity pulling effects which can drag the atomic frequency away from resonance.[156] This reduced cavity pulling can in turn improve the medium to long-term stability of the clock.

When constructing the clock using the cavity provided by Neuchâtel, the main parameters of interest to the operation of the clock are the microwave field homogeneity and field orientation factor. Microwave field homogeneity describes how similar a magnetic field strength the atoms are driven with across the volume enclosed by the atomic cloud. In the case of a low field homogeneity each atom across the cloud will receive slightly different microwave pulse areas. This serves to reduce fringe contrast when performing Ramsey spectroscopy on the atomic sample, thereby impacting the potential clock stability. Field orientation factor meanwhile describes how parallel each magnetic field line is, again assessed within the volume enclosed by the atom cloud. If the microwave field is not parallel with the magnetic bias field, applied to lift the atomic degeneracy, then it is possible to drive $\sigma^{\pm}$ transitions ($\Delta m_F = \pm 1$). This also results in reduced fringe contrast as many of the atoms are not driven between the desired $m_F = 0 \rightarrow m_F = 0$ groundstates in a π transition.

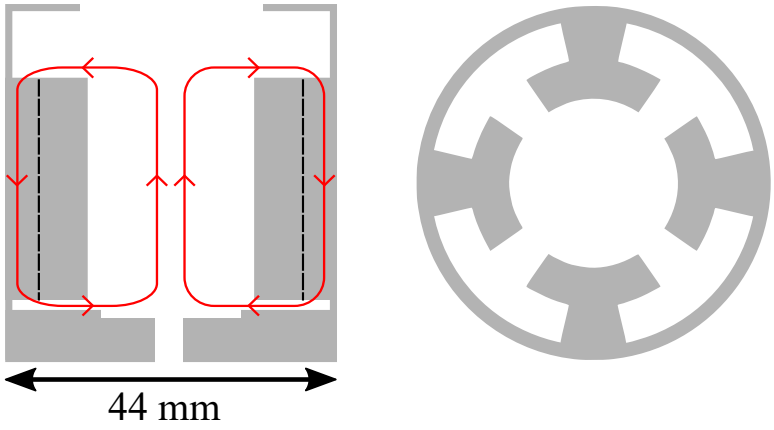

Figure 6.2: Loop-gap-resonator schematic. Left: front elevation, rough visualisation of magnetic field lines and their direction are shown in red. Right: top elevation showing loop-gap electrode geometry encased in the cavity body.

6.3.1 Additively Manufactured Cavity

With the continued rapid expansion of additive manufacturing processes, new applications and a wider array of printable materials are being developed.[157] Two main driving forces behind this development is the ability to rapidly prototype designs and fabricate structures that would be more complex and or time consuming to create by traditional machining. This latter point is of particular interest when aiming to develop a scalable microwave clock based around a LGR, as the manufacturing of the relatively complex electrode geometries becomes trivial. In addition to this, once a design has been finalised it is possible to reliably reprint the same structure. This highly scalable manufacturing process increases the potential commercialisation of the device into a real-world product.

The applicability of using additive manufacturing to manufacture LGR microwave atomic clocks was first investigated by a group led by this project's collaborators at Neuchâtel University.[152,158] Two methods of additively manufacturing the LGR structure were investigated; firstly direct printing of the LGR in an aluminium alloy by selective laser melting and secondly by printing the structure in polymer via the stereolithography method (SLA) and coating this in metal. These LGR structures were used to create vapour-cell based atomic clocks with the SLA cavity going on to demonstrate a highly competitive stability of $2.2 \times 10^{-13}\ \tau^{-1/2}$.[152]

In the current project the selective laser melting method of printing the cavity was opted for due to polymers typically being vacuum incompatible. This method

relies on a bed of powder alloy ($AlSi_{10}Mg$) to be selectively melted using a high powered laser beam in a 2D cross-section of the 3D object. The print bed is then lowered, the powder redistributed over the whole print bed and the process repeated. After many cycles the desired print is built up layer by layer into a 3D object.

A primary concern during the early design stages of this experiment was outgassing of the cavity material which is to be housed in-vacuum. Compared to traditional machining, additive manufacturing leaves a relatively high surface roughness, creating an large surface area and allowing many more potential contaminants to bind to the cavity surface. In addition to surface roughness, the manner in which the 3D structure is built up layer by layer means that small pockets of air are likely to be distributed throughout the entire structure, causing virtual leaks. To quantify the outgassing rate of the print material a dedicated vacuum chamber was constructed.

6.3.2 Cavity Outgassing Measurements

When measuring outgassing rates there are several distinct methods to choose from. Due to already available equipment the "gas accumulation method"[159] was selected for this study. Here a sample of the material to be studied is placed in a vacuum chamber and pumped down to the required vacuum levels. The chamber is then isolated from the pump and the evolution of the chamber pressure is recorded by a vacuum gauge. Ideally this gauge has little to no pumping effects of its own, with spinning rotor gauges being a common choice.[159] Here a Pfeiffer PRK 361 guage was used which has both a pirani and cold cathode method of measuring pressure. This is not ideal as this serves to remove gas from the vacuum environment in order to measure the pressure, likely skewing measured outgassing rates to be slightly lower than the true value. Relative measurements of known materials will still be reliable however, giving a good indication of the cavity materials suitability for vacuum. To measure the outgassing rate the instantaneous rate of rise of pressure (dP/dt) is measured immediately after isolation from the pump. This can then be related to the outgassing rate (q_A) through knowledge of the surface area (A) of the sample and internal volume of the chamber (V):

$$q_A = \left(\frac{dP}{dt}\right)_{t=0} \frac{V}{A}. \tag{6.1}$$

The outgassing test bed itself is shown in Figure 6.3. In the real clock exper-

iment the MOT coils are mounted within vacuum, causing the cavity to heat up to roughly 60°C during prolonged use of the trapping coils. Outgassing rates are highly dependent on temperature so to ensure a fair comparison in the test chamber the samples were also heated to a similar temperature. To achieve this a small resistive heater was embedded in a copper sample mount, supported by ceramic legs to ensure good thermal isolation from the rest of the chamber. A thermistor mounted under the sample was used to measure the temperature, with electrical feedthroughs allowing connection to the temperature logger and current source for the heater.

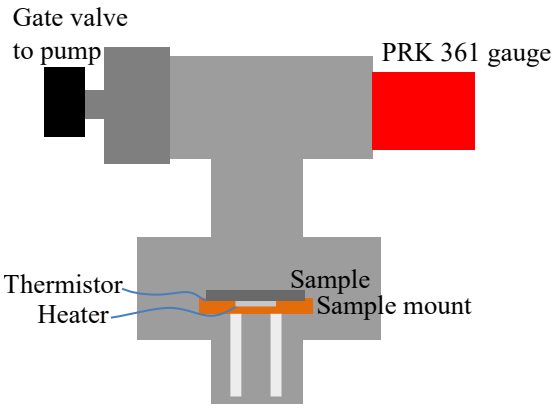

Figure 6.3: Outgassing measurement set-up

Three different metal samples were compared: the additively manufactured aluminium alloy, a bulk sample of aluminium (duralumin, a commonly used aluminium alloy) and 316LN stainless steel (widely used in UHV applications). Images of the metal samples are presented in Figure 6.4. The increased surface roughness of the additively manufactured Al is shown in this figure with the pitted surface clearly visible. Small 5 cm×2.5 cm×2 mm samples were prepared for the test and cleaned in acetone and methanol baths. These samples were then placed in the chamber which was baked at 100°C overnight while attached to a turbo pump. The temperature of the system was then brought back down and the chamber allowed to pump down for a further 24 hours. To measure the rate of pressure rise within the chamber the gate valve was closed and the pressure recorded by the gauge every 1 s (limited by the data logger). The pressure was then allowed to rise for 5 minutes before the valve was opened again with the chamber being pumped back down for an additional 5 minutes. This process was repeated several times in order to place standard deviation error bars on the mean value. A plot of a single pressure rise curve is shown in Figure 6.5.

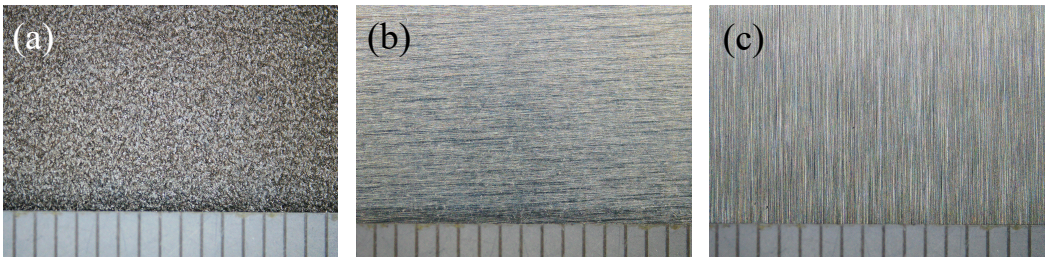

Figure 6.4: Microscope image of samples used in outgassing test showing surface roughness. (a) Additively manufactured Al alloy. (b) Bulk Al. (c) 316LN stainless steel. Ruler for scale indicates 1 mm divisions.

To get an accurate measurement of the outgassing of each sample, pressure rise curves must also be recorded with no sample in the chamber, with the sample mount heated to 60°C as before. This gives a measure of the outgassing of everything within the chamber that is not the sample, which is then subtracted from the outgassing rates measured with the samples present. Outgassing rates of the three samples are presented in Table 6.1.The outgassing rate of the 316LN stainless steel was found to be consistent with the empty chamber, indicating the outgassing rate is lower than can be measured in the current set-up. Interestingly the outgassing of the bulk Al sample and the additively manufactured sample were found to be the same, within the error of the measurement. This appears to indicate that gas pockets within the metallic structure causing virtual leaks are not an issue and standard vacuum cleaning techniques are enough to remove any contaminants present on the material's surface.

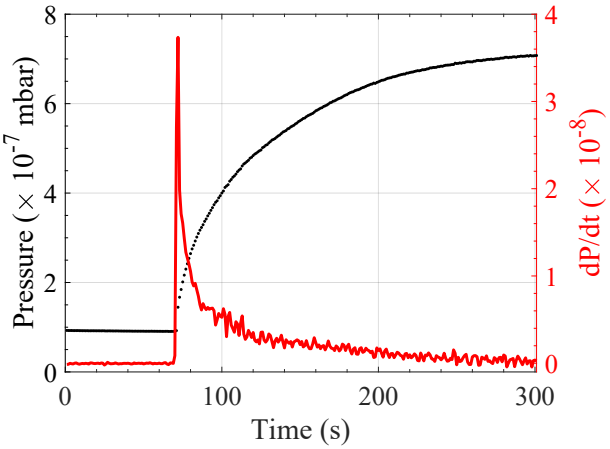

Figure 6.5: Example pressure rise curve used to calculate the outgassing of the 316LN steel sample.

Subsequently to the inception of this project, additive manufacturing has

demonstrated compatibility with UHV vacuum levels.[160] Here the authors successfully demonstrated an additively manufactured UHV chamber with standard ConFlat ports that was able to maintain a chamber pressure of 10^{-10} mbar. This chamber was fabricated in the same material as the microwave cavity discussed here ($AlSi_{10}Mg$) with the authors attributing the good outgassing properties to an oxidised magnesium rich surface layer suppressing the diffusion of various species from the material.

Sample type	Outgassing rate (mbar m^3/ s m^2)
Bulk Al (Duralumin)	$(7.2 \pm 0.8) \times 10^{-9}$
Additively manufactured Al	$(6.6 \pm 0.8) \times 10^{-9}$
316LN stainless steel	$< 5.9 \times 10^{-9}$

Table 6.1: Measured outgassing data.

An obvious next step for future iterations of this clock experiment would be to make the cavity act also as the vacuum chamber. This would significantly reduce the SWaP of the experiment and mean that the vacuum and cavity could be printed as a single bulk component, highly beneficial for future scalability. It would also be interesting to investigate different materials, for example titanium, which is often used in UHV applications and can also be additively manufactured.

6.4 Experimental Realisation of Clock

The experimental set-up built around the microwave cavity was designed and constructed by Ben Lewis[161] with minor improvements to optimise the clock stability carried out during the course of my investigations, discussed in detail in Chapter 7. A primary goal of the experiment during the design process was to investigate a grating-chip atomic fountain where the atoms are launched upwards in a moving molasses, analogous to fountain clocks.[19] This concept was successfully demonstrated utilising CPT interrogation before integrating the microwave cavity into the set-up.[162] Due to the significant additional complexity this scheme entails however, it was not employed for the first demonstration of the microwave cavity clock discussed here.

6.4.1 Experimental Set-up

Optical set-up

The optical set-up along with an energy level diagram of all the necessary atomic transitions is shown in Figure 6.6. This initially consisted of a home-built ECDL[56] single passed through AOM_0 (-1×300 MHz frequency shift) and locked to the $F = 2 \rightarrow F' = 2, 3$ CO transition, resulting in a laser frequency locked 167 MHz below the $F = 2 \rightarrow F' = 2$ transition. Shifting the laser frequency 300 MHz below the lock point serves to make it easier to address all the required transitions using a single laser. The rest of the light is then coupled into a fibred EOM to create the necessary repump frequencies and then used to seed a tapered amplifier (TA) to amplify the light. From the TA the light is split into three optical beam paths each with a double-pass AOM for intensity and frequency control. AOM_1 ($+2 \times$ 212 MHz) shifts the light to be around 2Γ red detuned from the cooling transition which is then coupled into a single mode polarisation maintaining fibre and passed to the vacuum chamber to be used for atom trapping. AOM_2 ($+2 \times 80$ MHz) is used for state preparation (Sec 6.4.2) and AOM_3 ($+2 \times 217$ MHz) for state read out (Sec 6.4.3). Both these beams are coupled into a second common fibre and also passed to the vacuum chamber.

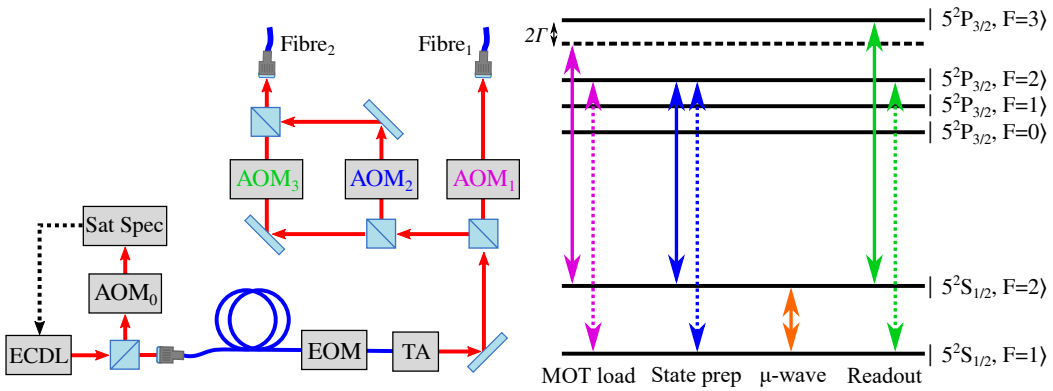

Figure 6.6: Left: Simplified optical set-up employed for the clock experiment. ECDL is locked to an atomic line via saturated absorption spectroscopy (Sat Spec) after passing through AOM_0. Main beam is coupled into a fibred EOM and then used to seed a TA. From the TA light is split into three paths: AOM_1 (trap light), AOM_2 (state preparation light) and AOM_3 (state read out light). Right: Energy level diagram of required transitions in experiment. Arrow colour corresponds to the AOM used to address that transition. Solid arrows correspond to the carrier frequency while dashed arrows indicate repump light.

Due to the limited extinction ratio of AOMs, mechanical shutters[163] (not shown in Figure 6.6 were included in all beam paths, though in operation only the trap beam shutter was actually utilised. This shutter helped ensure no trap light was incident on the atoms during microwave interrogation, reducing light-shift effects on the clock transition.

Subsequently to initial characterisation of the experiment, the ECDL seed laser was swapped to a commercial frequency doubled telecoms laser.[58] This decision was made due to the inherent stability of frequency doubled systems over the notoriously vibrationally sensitive ECDLs. This laser also remains reliably locked over an entire day, beneficial when taking long stability measurements.

Physics Package

The microwave cavity has a volume of ≈67 cm^3 and is mounted within a commercial vacuum chamber with optical access provided via optical viewports in two orthogonal axes. The first axis (vertical w.r.t gravity) is parallel to the cavity axis and allows the trap light to be aligned onto the 2 cm×2 cm grating chip, mounted within the cavity body (see Figure 6.7), after expansion and collimation from the fibre. The second axis (horizontal w.r.t gravity) allows the state preparation and state read out beam to be directed onto the atom cloud, passing through two 4 mm holes in the side of the cavity body. These holes are positioned to allow good optical overlap between the side beam and where the MOT forms above the grating-chip. Sate preparation and read out light is expanded from the fibre to a $1/e^2$ diameter of 7 mm. This over expansion of the beam ensures a relatively constant intensity profile across the atom cloud for state preparation and read out. After expansion and collimation the light is split into two paths using a 90:10 non-polarising beam splitter (NPBS). Light from the reflection port is aligned on to a reference photodiode (PD_{Ref}) while the remainder of the light is aligned through the cavity holes and retro-reflected by a mirror (M) before being aligned onto a second signal photodiode (PD_{Sig}).

Anti-Helmholtz trapping coils are located within the vacuum chamber on a coil former that also houses the microwave cavity.[161] Three axis square Helmholtz shim coils surround the entire vacuum chamber and allow for the cancellation of stray DC magnetic fields and the application of a magnetic bias field (C-field) to lift the atomic degeneracy. UHV is maintained by a 45 l/s ion pump attached to the vacuum system which maintains a pressure of $\approx 10^{-8}$ mbar as measured by

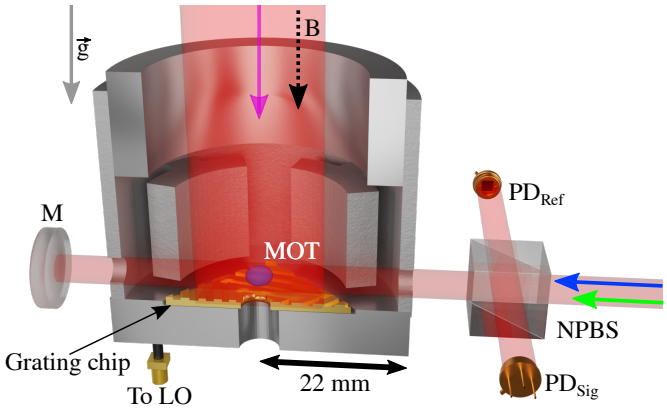

Figure 6.7: Simplified schematic of the clock physics package. Trap light (pink arrow) propagates parallel to the magnetic bias field (black dashed arrow), 90:10 NPBS splits the optical pumping (blue arrow) and read out (green arrow) light onto a reference photodiode (PD_{Ref}) and signal photodiode (PD_{Sig}) after being retro-reflected M. Local oscillator (LO) is connected via a SMA vacuum feedthrough. The direction of gravity (grey arrow) is also shown.

MOT load curves.

The preparation of cold atoms was done in the standard way as discussed in Sec 3.1 with around 1×10^6 atoms typically being loaded into the MOT in 500 ms and cooled to approximately 10μK during a 10 ms red molasses stage. While this atom number is relatively modest this was primarily due to the low alkali density within the chamber during the initial characterisation, corresponding to a MOT load curve with a large time constant. In Chapter 7 the atom number was increased by introducing atom recapture and changing the alkali dispensers.

6.4.2 State Preparation

After molasses the atoms are assumed to be roughly evenly distributed between the five available Zeeman sub-levels of the $F = 2$ ground state. If the clock sequence were directly performed this fact would limit the signal contrast to 20% as only $\approx \frac{1}{5}$ of the atoms are in the $m_F = 0$ clock state. In practice it was found that directly after molasses slightly more atoms are prepared in either of the stretched Zeeman sublevels, $m_F = \pm 2$. This is attributed to the unique beam geometry of the GMOT where the diffracted cooling beams are projected at an angle onto the quadrupole magnetic field. This projection breaks the light polarisation into π and $\sigma^{\pm}$ components.[40,42] When all the trapping beams are accounted for it is thought a slight polarisation imbalance favours

circularly polarised light, optically pumping more atoms to one or other stretched Zeeman sublevel. This effect has recently been predicted theoretically by D. S. Barker *et al.*[164]

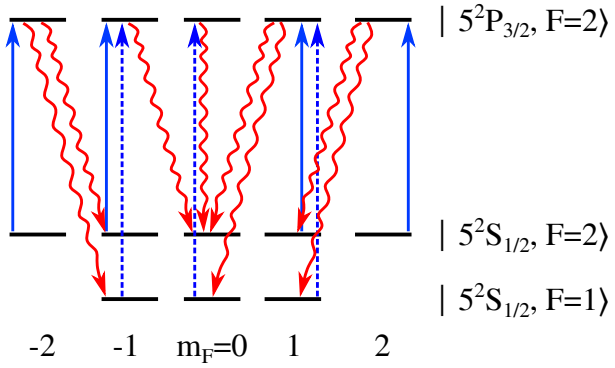

Figure 6.8: State preparation transitions diagram. Solid blue arrows show main optical pumping transition, repump transitions indicated by dashed blue arrows. Decay paths are shown by red arrows. Not all decay paths are indicated.

One can increase the signal contrast by extinguishing the repump light at the end of molasses, optically pumping the atoms to the $F = 1$ state with a maximum possible contrast of 33%, a marginal improvement. Significant increases in contrast are only achievable by optically pumping the atoms into a single $m_F = 0$ level. This is achieved by leveraging a forbidden electric dipole transition. Atoms are pumped with light that is linearly (π) polarised with respect to the C-field, driving the F=2→F'=2 transition with repump light tuned to F=1→F'=2. Due to the selection rule that $\Delta m_F = 0$ transitions are forbidden if $\Delta F = 0$, atoms will accumulate in $|F = 2, m_F = 0\rangle$.[165] The presence of repump light on the F=1→F'=2 is required to recycle atoms shelved in the F=1 hyperfine state manifold. Good magnetic field alignment with the light polarisation axis is critical to achieve good state preparation using this scheme as any amount of circularly polarised light will pump atoms out of the $m_F = 0$ clock-state (see Sec 6.4.4).

6.4.3 State Read out

The final stage in the experimental cycle is state read out. At present this is done in absorption using a probe beam directed through the cavity side holes, measured on PD_{Sig}. The relative absorption of which gives an indication of the population in each ground state. Initially absorption was chosen as each absorbed photon from the probe beam corresponds to an increase in detected signal. Fluorescence

detection is more typically used in microwave fountain clocks due to the high signal to noise ratio (SNR) on a low background signal achievable,[11] allowing the detection noise floor to be pushed towards the quantum projection noise limit.[166] At present the numerical aperture available through the side holes means the collection solid angle for scattered photons is relatively low, making fluorescence detection impractical in the current physics package. Future iterations of the physics package design may use fluorescence detection but for now absorption is sufficient.

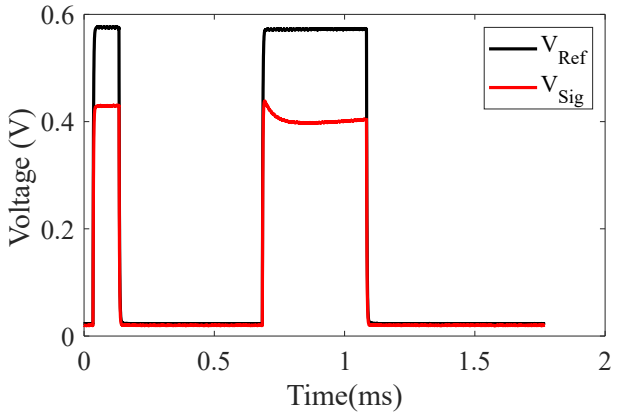

Figure 6.9: State read out voltage traces.

The atomic state populations are read out in a two stage process. First, a short pulse tuned to the $F = 2 \rightarrow F' = 3$ transition with no repump is applied, this gives a measure of the number of atoms in the $F = 2$ state. A second pulse with repump light turned on is then applied. This gives a normalisation factor for the total number of atoms present, suppressing the effect atom number fluctuations have on the SNR. The signal from $\mathrm{PD_{Ref}}$ is subtracted from $\mathrm{PD_{Sig}}$ to reduce the effect probe intensity fluctuations have on the read out. The final state population is calculated as follows:

$$P_2 = \frac{[F=2]}{[F=2]+[F=1]} \equiv \frac{\langle V_{Sig}(Pulse_1)\rangle - \langle V_{Ref}(Pulse_1)\rangle}{\langle V_{Sig}(Pulse_2)\rangle - \langle V_{Ref}(Pulse_2)\rangle}, \tag{6.2}$$

where $\langle V\rangle$ denotes a time averaged voltage as measured by each photodiode. While $V_{Sig}(Pulse_1)$ is relatively flat in time $V_{Sig}(Pulse_2)$ exhibits a dip as atoms are optically pumped out of the $F = 1$ ground state, followed by decreasing absorption as atoms are heated by photon scattering events out of the probe beam. Care must therefore be taken to ensure the voltage signal is averaged around the base of the dip before a significant portion of the atoms are ejected from the probe beam.

6.4.4 Rabi Oscillations

One of the first tests of the experimental set-up was to perform Rabi oscillations, simply cycling the atomic population between the two ground states. This is used to ascertain the microwave power required for the slightly more complex Ramsey interrogation when operating as a clock.

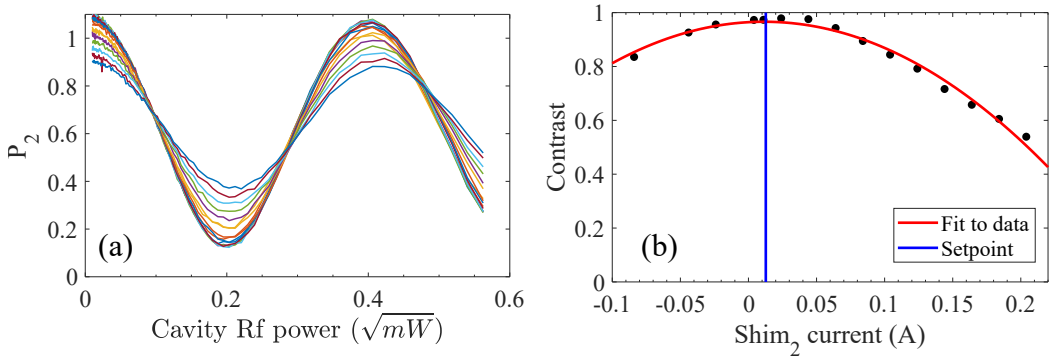

Figure 6.10: Example of one axis magnetic field alignment optimisation. (a) Rabi oscillations obtained with different currents applied to the shim coils. (b) Rabi oscillation contrast plotted as a function of the current applied to the shim. Blue line shows set point for maximum contrast.

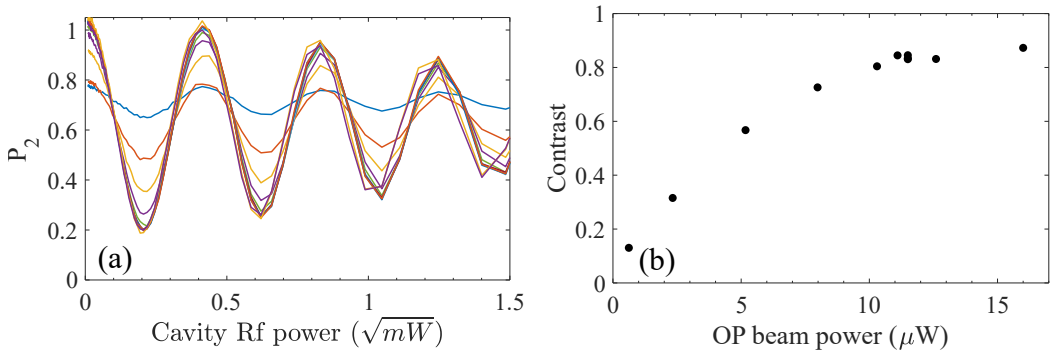

Figure 6.11: State preparation beam power optimisation. (a) Rabi oscillations obtained with different state preparation beam powers. (b) Rabi oscillation contrast plotted as a function state preparation beam power.

The contrast of the first Rabi oscillation was also found to be an excellent metric for the optimisation of the state preparation. Due to the state preparation's sensitivity to the light polarisation, alignment of the magnetic bias field is critical. Figure 6.10(a) shows Rabi oscillations obtained for various currents applied to one of the shim pairs. The contrast of these oscillations is shown in Figure 6.10(b) which is fit with a second order polynomial to obtain the set-point

corresponding to the best contrast. A similar plot can be made for the state preparation beam power, shown in Figure 6.11. It can be seen that the calculated P_2 can sometimes take a non-physical value greater than one. This is due to atom losses between the first and second read out pulse which can slightly skew this value during the normalisation calculation. This is not a large issue as the whole curve is similarly skewed so performing a normalisation recovers a physical value. This may be able to be improved upon in future however by cooling the atoms more or using a larger probe beam so all the atoms that interact with $Pulse_1$ also interact with $Pulse_2$.

A typical normalised example Rabi oscillation is shown in Figure 6.12, the x-axis re-scaled in terms of pulse area. The decay of the oscillations is due to microwave field inhomogeneities across the volume of the cavity occupied by the atomic cloud. As atoms are excited between the two ground-states a phase difference builds up across the cloud due to the slightly different pulse areas observed by each atom. Over several cycles between the two groundstates this serves to wash the fringes out entirely. This effect is discussed in detail in Ref[132] with the field inhomogineities calculated to be around 6%.

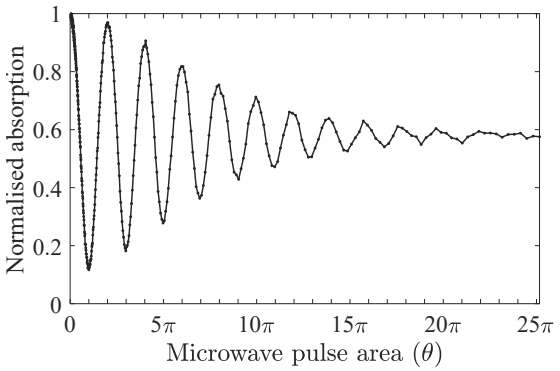

Figure 6.12: Typical example Rabi oscillation.

6.4.5 Zeeman Spectroscopy

The fraction of repump light present during state preparation is another variable that must be tuned to maximise its efficacy. Figure 6.13 shows that as the amount of repump light is increased more atoms are prepared in the F=2 ground state, indicated by the y-offset level of each plot. The large central peak corresponds to the clock π transition, $|F = 2, m_F = 0\rangle \rightarrow \ |F = 1, m_F = 0\rangle$. Likewise the smaller side peaks also correspond to π transitions but in this case of the

$|F = 2, m_F = \pm 1\rangle \rightarrow |F = 1, m_F = \pm 1\rangle$ states. As the state preparation becomes more efficient these side peaks disappear as all Zeeman sublevels apart from $m_F = 0$ are depopulated.

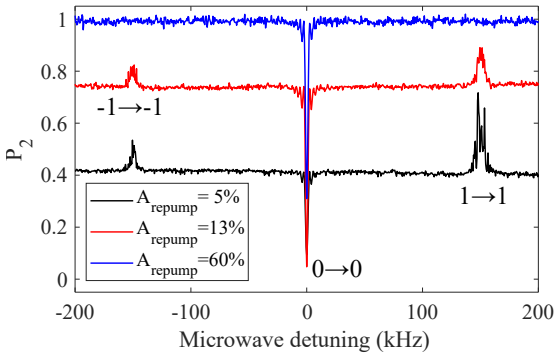

Figure 6.13: Optimisation of repump light fraction during state preparation taken at a bias field of 100 mG. A_{repump} is the sideband amplitude with respect to the carrier. Numbers indicate the relevant m_F levels for each peak.

A key metric of the microwave cavity is the field orientation factor (ξ). As mentioned in Sec 6.3 the microwave field lines must be as parallel as possible over the volume enclosed by the atom cloud and be well aligned with the C-field. If either of these conditions are not met then the cavity will drive additional unwanted $\sigma^{\pm}$ transitions ($\Delta m_F = \pm 1$) in addition to the required π ($\Delta m_F = 0$) transitions. The lack of such peaks, outwith the baseline noise in Figure 6.14, is a good indicator that the C-field is well aligned and the field orientation factor (ξ) is high. This metric is defined as[132]

$$\xi = \frac{\int S_\pi dV}{\int (S_\pi + S_\sigma) dV}, \tag{6.3}$$

where S_π and S_σ are the π and σ components of the Zeeman spectrum respectively and V is the volume enclosed by the atomic cloud. ξ is calculated to be $> 97\%$.[132]

Figure 6.14(b) shows the central Zeeman feature as the microwave detuning is swept across the clock transition. The characteristic $sinc^2$ line shape due to a square microwave pulse is evident. The modulus squared of c_e, as calculated from Eq 2.13, is also plotted for the experimental microwave time, showing excellent agreement with the theoretical line shape.

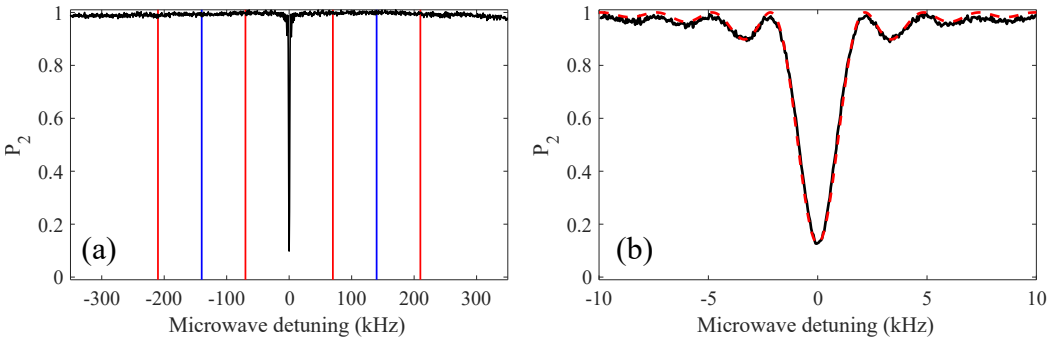

Figure 6.14: Zeeman spectroscopy scanning microwave detuning with optimised experiment and 100 mG bias field. (a) Full Zeeman scan over whole hyperfine ground state structure. Red lines indicate position of $\sigma_{\pm}$ transitions, Blue lines indicate π transitions where $m_F = \pm 1 \rightarrow m'_F = \pm 1$. (b) Central feature of Zeeman scan. Black points show experimental data, red dashed curve shows $|c_e|^2$ as calculated by Eq 2.13, plotted for a microwave pulse time t_m=400 μs. The amplitude of this theory curve is scaled is to experimentally measured amplitude.

Chapter 7

Clock Stability

In order to quantify the performance of any clock and draw meaningful comparisons between devices it is important to understand the distinction between accuracy and stability. An accurate frequency reference is one that operates close to its stated output frequency, often a 10 MHz sine wave or 1 pps trigger. A stable frequency reference operates consistently around the same output frequency over a quoted time period. While many vapour cell based frequency standards are highly stable, their accuracy is typically relatively low due to buffer gas shifts.[1] High accuracy constitutes one of the primary benefits of cold-atom clocks due to the high degree of isolation from their environment, corresponding to lower perturbations of the atomic transition.

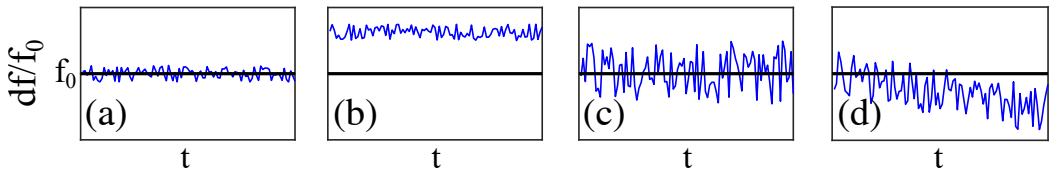

Figure 7.1: (a) Fractional frequency array of an accurate and stable frequency reference. (b) Stable but not accurate. (c) Accurate but not stable. (d) Neither accurate or stable

7.1 Allan Deviation

To truly understand clock performance the clock stability must be assessed over various time periods. This is important because different applications will have drastically different requirements of their time keeping devices, making it necessary to have a rigorous understanding of the clock behaviour over different time

scales. The Allan variance[167] and variations of it are used to define this stability at different times with the 1 s Allan variance often being quoted in discussions of clock performance.

The Allan variance is calculated by considering a fractional frequency array of the measured clock stability compared to some reference oscillator:

$$y(t) = \frac{f_0 - f(t)}{f_0} = \frac{df(t)}{f_0}, \tag{7.1}$$

where $f(t)$ is the instantaneous frequency and f_0 is the nominal frequency. The Allan variance, $\sigma_y(\tau)$, is defined as half the squared mean frequency deviation between two successive time periods, τ, and can be expressed as

$$\sigma_y^2(\tau) = \frac{1}{2(M-1)} \sum_{i=1}^{M-1} (\bar{y}_{i+1}(\tau) - \bar{y}_i(\tau))^2, \tag{7.2}$$

where $\bar{y}_i(\tau)$ is the mean frequency and M is the number of samples.

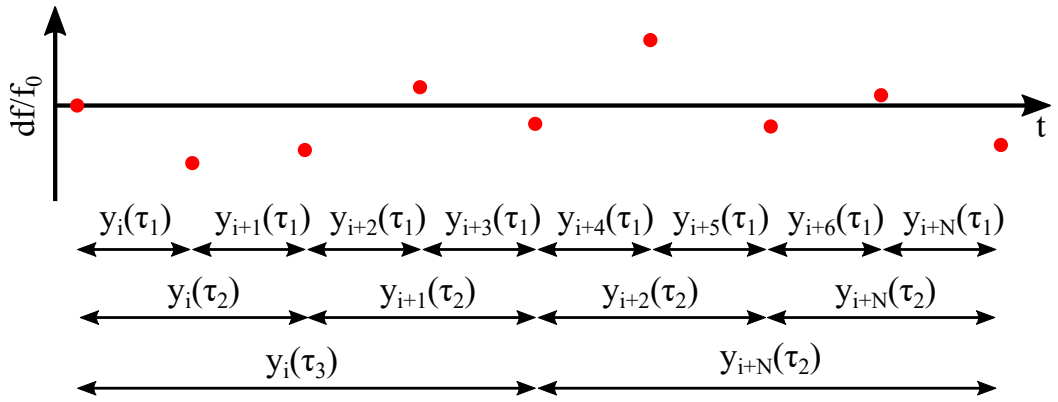

Figure 7.2: Method for calculating the non-overlapping Allan variance. Allan variance is calculated with non-overlapping time samples for increasing averaging windows τ_n.

A variation on the original method of calculating the Allan variance that is now more commonly used is the "Overlapping Allan variance". While conceptually very similar this method overlaps each averaging window, $\tau = n\tau_0$, with the previous one, where τ_0 is the data sampling period and m is an integer describing the length of the averaging window. The entire data set is stepped through in this overlapping manner as shown in Figure 7.3, allowing better confidence bounds to be placed on the resulting Allan deviation plot for the same length data series. The Overlapping Allan deviation is then calculated as follows:

$$\sigma_y^2(\tau) = \frac{1}{2n^2(M-2n+1)} \sum_{j=1}^{(M-2n+1)} \sum_{i=j}^{(j+n-1)} (\bar{y}_{i+n} - \bar{y}_i)^2. \tag{7.3}$$

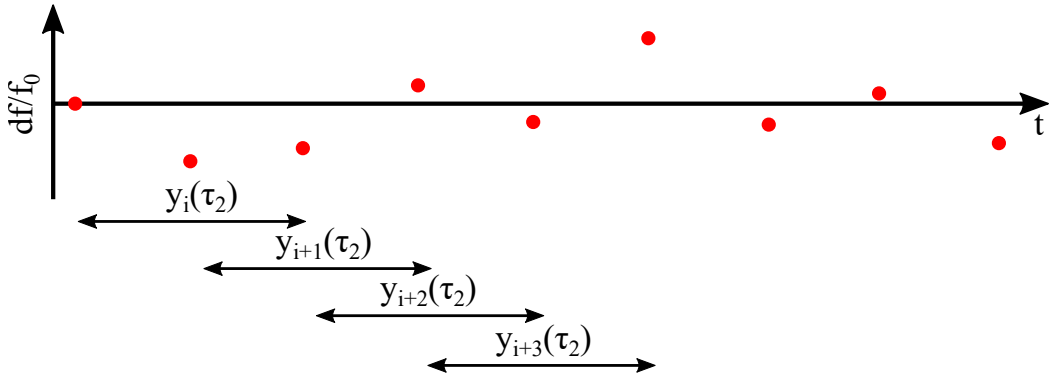

Figure 7.3: Method for calculating the overlapping Allan deviation shown for $n = 3$. This process is repeated for incrementing averaging factors to build up an Allan deviation plot for the whole data set.

In addition to providing an excellent metric to compare different clocks to each other, the gradient of Allan deviation plots also can indicate to the user what noise types are present in their system,[1,168] this is summarised in Table 7.1. An idealised Allan deviation plot is also shown in Figure 7.4 with the different slope regions marked. It is common to refer to the stability of an oscillator in the short, medium and long-term. Although no standard exists defining these periods, an indication of the what is meant when referencing these times is shown on the same figure.

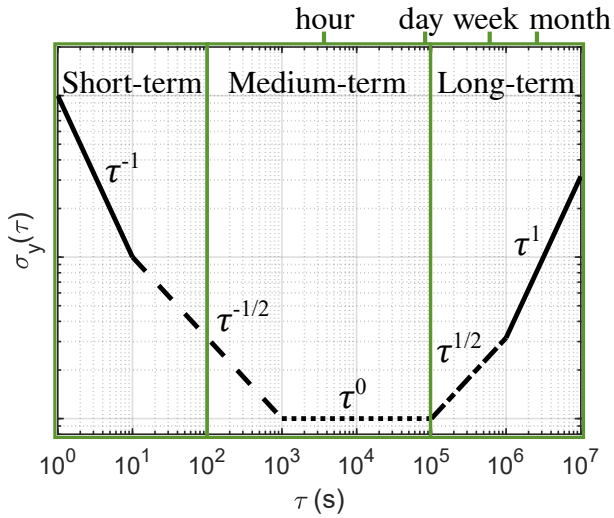

Figure 7.4: Idealised Allan deviation plot showing different slope regions.

Noise type	$\sigma_y(\tau)$ slope	Possible cause
White Phase/ flicker phase noise	τ^{-1}	High frequency noise on clock signal/ electronics
White frequency noise	$\tau^{-1/2}$	Additive white noise sources e.g atom/ photon shot noise
Flicker frequency noise	τ^{0}	Some limit of system e.g. quartz LO
Random frequency walk	$\tau^{1/2}$	Environmental noise
Frequency drift	τ^{1}	Environmental noise

Table 7.1: Table of noise types in clock and the corresponding slope of the Allan deviation on a log-log plot. Possible causes of the noise source are also shown.

7.2 Locking to the Atomic Signal

To lock the local oscillator (LO) to the atomic frequency, an error signal must first be constructed. In pulsed atomic clocks this is generally achieved by sequentially interrogating the atoms at the half width half maximum point of the central Ramsey fringe, as shown in Figure 7.5. The frequency deviation, df, of the local oscillator from the atomic frequency f_0 is then proportional to the difference in these populations with some gain factor, G:

$$df \propto G(y_2 - y_1). \tag{7.4}$$

This error signal is then used to tune the frequency of the local oscillator. The gain factor required is experimentally optimised and depends on the tuning coefficient of the local oscillator along with the gradient of the discriminator slope being locked to. In this case the 10 MHz LO is voltage tuned with a tuning coefficient of -0.07 ppm/V.

7.3 Short-Term Stability Optimisation

To begin optimising the clock a metric of clock stability as a function of the operating conditions is first required. The predicted signal to noise (SNR) limited short-term stability of a local oscillator stabilised to the atomic signal in terms of the Allan deviation is given by[1]

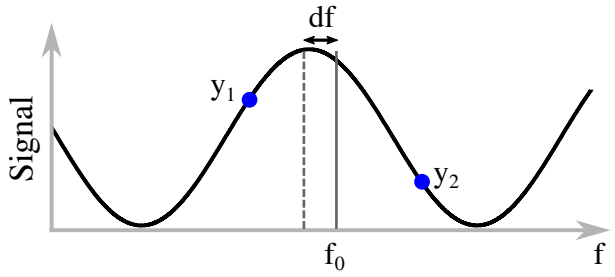

Figure 7.5: Diagram indicating how the clock error signal is constructed by sequentially measuring atomic state populations at the half width half maximum point of the central Ramsey fringe.

$$\sigma_y^{SNR}(\tau) = \frac{1}{\pi C}\frac{\Delta f}{f_0}\frac{1}{SNR}\sqrt{\frac{T_C}{\tau}}, \tag{7.5}$$

where C is the fringe contrast, Δf is the fringe linewidth, f_0 is the operating frequency of the clock, T_C is the full experimental cycle time, and τ is the averaging time. A good starting point for the optimisation of the clock is measuring the fringe SNR at various Ramsey times. Increased Ramsey times result in narrower fringes (Sec 2.2.2) and a correspondingly steeper discriminator slope to lock to, benefiting the short-term stability. In the current configuration however the atomic cloud is in free fall during the Ramsey time. This provides a limit to the maximum useful Ramsey time as the SNR will be degraded as more atoms fall out of the read out beam.

To find the optimum trade-off point between narrow finges and high SNR an experiment was carried out to measure the fringe SNR at the half-width points of the central fringe as a function of Ramsey time. The population at these points was measured repeatedly with the local oscillator stabilised to GPS, ensuring variations in measured populations are not a result of local oscillator frequency drift. SNR is defined as the ratio of the mean amplitude divided by the standard deviation in amplitude. The predicted short term stability is then calculated using Eq 7.5 and plotted as a function of the Ramsey time, shown in Figure 7.6.

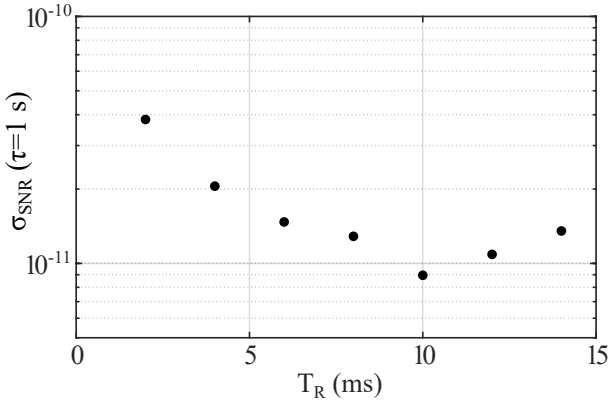

Figure 7.6: Predicted short-term stability (τ=1 s) as a function of Ramsey time.

From Figure 7.6 we find that as the Ramsey time in increased the predicted stability also improves to the 8.95×10^{-12} level for a 10 ms Ramsey time, corresponding to SNR=111. After this time however the predicted stability begins to decrease as the SNR is degraded. This reduction is SNR is attributed to a reduced overlap between the atomic cloud and the read out beam. The reduced overlap is largely due to the atomic cloud falling under gravity with a secondary smaller effect due to the ballistic expansion of the cloud due to its finite temperature.

The extension of this Ramsey time should be possible by moving the holes in the cavity body lower down, introducing elliptical holes to maintain good probe-atom overlap along the path of gravity or by implementing a grating-chip atomic fountain.[161,162] This last option is particularly attractive because as with traditional atomic fountains it would be possible apply both $\pi/2$ pulses when the atoms are at the same vertical point of the cavity. This will allow the phase difference observed by the atoms between the two microwave pulses to be minimised, essential for high contrast Ramsey fringes in a relatively low-Q cavity such as used here. A grating-chip atomic fountain (using CPT interrogation) such as this has already demonstrated Ramsey times out to 100 ms, with a corresponding fringe linewidth of 5 Hz.[162] Longer Ramsey times will result in a larger atomic cloud due to its ballistic expansion during the time of flight. For a temperature of 4 μK for example, the cloud size would increase from a 2σ diameter of 1 mm to 4 mm over the projected 100 ms Ramsey time. As a result, the microwave field will be sampled over a larger volume during the second pulse, increasing the field inhomogeneity experienced by the atoms.[132] This will not however pose too great an issue as even a 30% field inhomogineity, a reasonable worst-case assumption

based on similar LGR cavities,[151] only results in a reduced maximum contrast at the 80% level as calculated using Eq 5 in Ref.[132] Substituting this new contrast into Eq 7.5 along with the reduced atomic linewidth still results in an eight-fold improvement to the short-term stability.

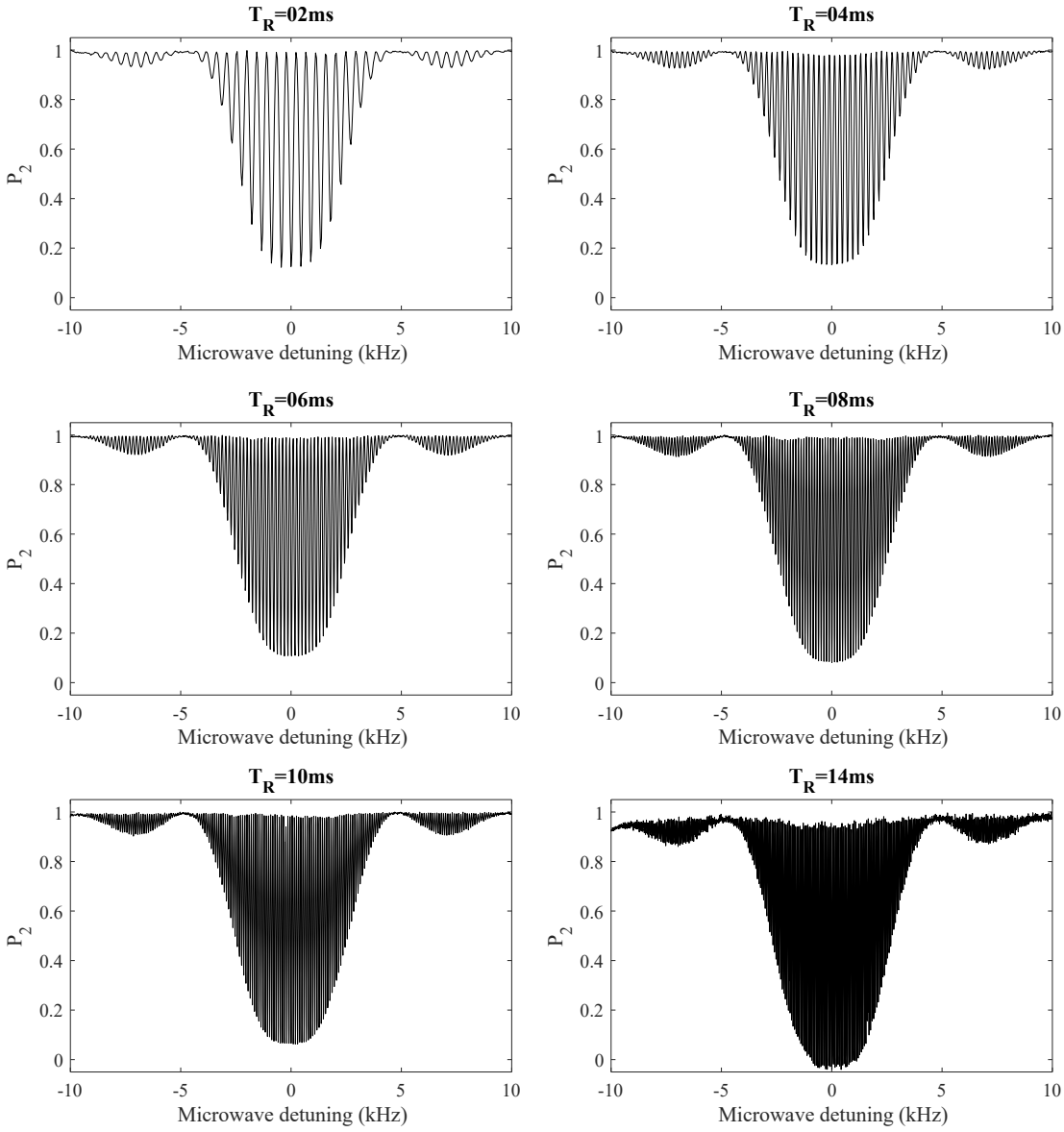

Figure 7.7: Experimental Ramsey fringes for various Ramsey times.

7.3.1 Ramsey Fringe Optimisation

Simulations carried out by E. Batori and published in Ref[131,132] show that the microwave field strength across the cavity length varies. In the typical 10 ms Ramsey time the relative field deviation is expected to be around 10% over the distance the atoms fall. The RF power for a given microwave pulse length to apply

a π pulse is calibrated from the first Rabi oscillation and the time halved to give two $\pi/2$ pulses. This calibration no longer holds true if the atoms experience a different microwave power during the second pulse as they have fallen to a different cavity region.

With a view to optimising the Ramsey fringe contrast this effect was investigated by calibrating the microwave power as normal but varying the duration of the second microwave pulse, t_{m2}. By varying the duration of the second pulse, microwave the pulse area can be controlled. Figure 7.8 (a-b) shows the effect this can have on fringe contrast for a 10 ms Ramsey time. When mapped out fully as shown in Figure 7.8 (c) an optimum pulse duration for a given Ramsey time can be found. Figure 7.8 (d) indicates that as expected longer Ramsey times require a larger pulse area correction, with an additional 20 μs required for a 10 ms Ramsey time. This behaviour is expected as for longer Ramsey times the atomic cloud falls further along the cavity axis. The atomic cloud thus experiences a lower pulse area and requires a higher requested microwave power from the frequency source to correct for the lower amplitude microwave field. Although slight gains at can be made on fringe contrast by tuning the second pulse time the benefits are only at the 1-2% level. Tuning the second pulse in this manner is therefore deemed currently unnecessary. When eventually operating the experiment in a launched mode this tuning may become an important factor to high contrast fringes due to the thermal expansion of the cloud during the longer Ramsey times.

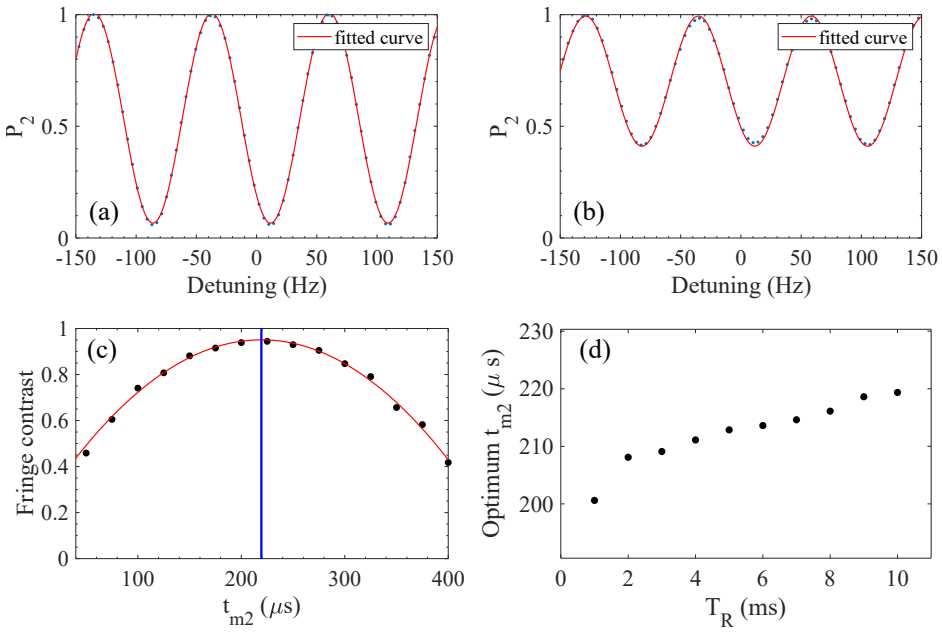

Figure 7.8: (a) Example 10 ms Ramsey fringe with standard 200μs second pulse duration. (b) Example 10 ms Ramsey fringe with 375μs second pulse duration. (c) 10 ms Ramsey fringe contrast as a function of second Ramsey $\pi/2$ pulse duration. (d) Optimum second pulse duration as a function of Ramsey time.

7.3.2 Atom Recapture

So far we have dealt with Ramsey fringe optimisation to improve the performance of the clock. Another important factor that can be improved upon is the experimental cycle time, T_C. The benefits of this are twofold: firstly the predicted clock stability is proportional to $\sqrt{T_C}$ (Eq 7.5) and secondly the Dick effect (discussed in Sec 7.5.3) can be ameliorated by reducing cycle time. At present the experimental cycle time is dominated by the MOT load time (typically 500ms). This rather long load time is necessary due the the low Rb background vapour density in the experiment. In order to reduce cycle time atom recapture was implemented. This technique has successfully been used in other cold-atom experiments to reduce dead time[169–171] and relies on reloading a percentage of the atoms from the previous experimental cycle into a new MOT. Unlike in vapour cell clocks there are no unwanted quantum memory effects due to interrogating the same atoms over two cycles as the atomic populations are randomised in the MOT.

Experimentally recapture is achieved by simply turning the trap light and

quadrupole magnetic field back on before the atoms fully disperse. Over several cycles the steady state atom number is then a function of the atoms loaded from the background vapour, recaptured atoms and the usual atomic losses due to collisions. Rakholia *et al.* find an expression for this steady state atom number by modelling this process as a geometrical sum over several cycles, expressed as[169]

$$N_{ss} = N_{\infty}\frac{T_L}{T_C}\frac{1}{1+\frac{1-r_0}{\beta T_C}}, \tag{7.6}$$

where N_{∞} is the maximum trapped atom number achievable for an infinitely long load time, T_L is the MOT load time, r_0 is the fraction of atoms recaptured between cycles and β is the $1/e$ MOT load time constant extracted from Eq 3.3 ($\approx$ 2 s).

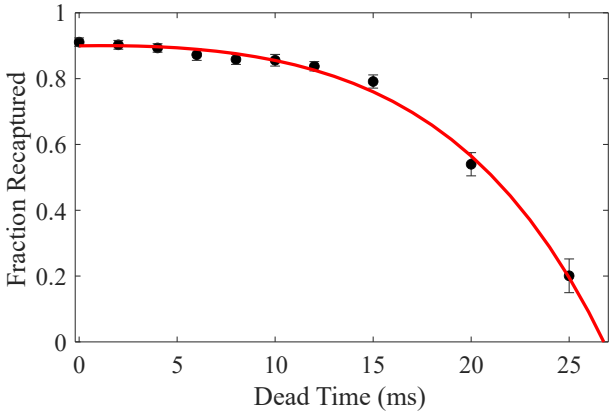

Figure 7.9: Recapture fraction with respect to the dead time. Red line is empirical exponential fit to data.

The fraction of atoms recaptured between cycles was measured for various drop times as shown in Figure 7.9. From this we see 80-90% of the atoms are recaptured between cycles up to a drop time of 15 ms, after which the recapture fraction significantly falls off as more atoms leave the GMOT optical overlap region.

Figure 7.10 (a) shows the mean maximum fluorescence measured by a photodiode over repeated recapture cycles, showing that after around 30 cycles the atom number reaches steady state. An exponential is fitted to these data which is used to extract the maximum trapped atom number in steady state, N_{SS}. N_{SS}/N_{∞} is then measured as a function of drop time for various MOT load times, an example of which is shown in Figure 7.10 (b) for T_L =100 ms. The red line in this plot is the theoretical atom number as calculated by Eq 7.6. From Figure 7.10

(b) we see that the number of atoms recaptured is slightly less than would be expected. The reasons for this are not fully understood, however for our purposes the recapture works sufficiently well that at a 100 ms load time with a 10 ms dead time, analogous to the Ramsey time, we can load 45% of N_∞. This cycle was chosen as trade off between a high experimental cycle rate and a reasonable atom number, representing a full clock cycle rate of 7 Hz. Interestingly, due to the low background vapour density in the system this actually equates to an increase in trapped atom number to 3×10^6 compared to the 1.5×10^6 typical of a 500 ms load time with no recapture. Far higher experimental cycle rates of 100 Hz using recapture have been demonstrated[172] however this is not currently possible in our system due to the low Rb vapour density.

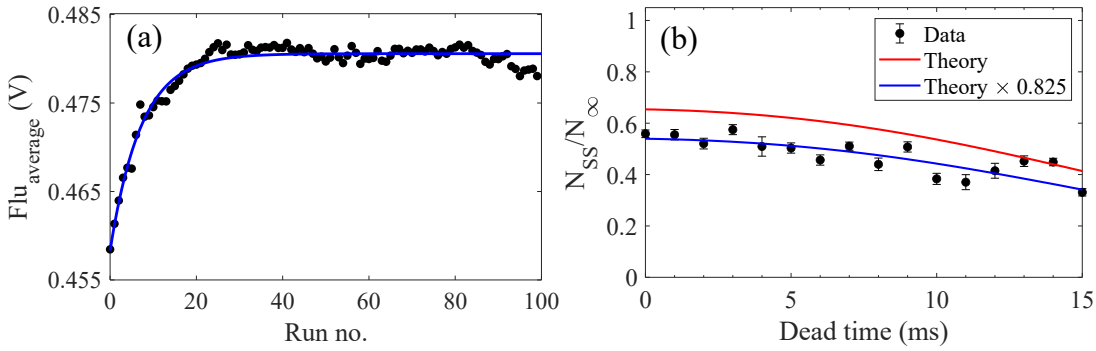

Figure 7.10: (a) MOT fluorescence with respect to the number of cycles showing the atom number reaching steady state for Run no.>30. Blue curve is exponential fit to the data, used to extract N_{SS}. (b) Number of trapped atoms in steady state with respect to the experimental dead time. Error bars are calculated from the standard error of the exponential fit shown in (a).

7.4 Measured Clock Performance

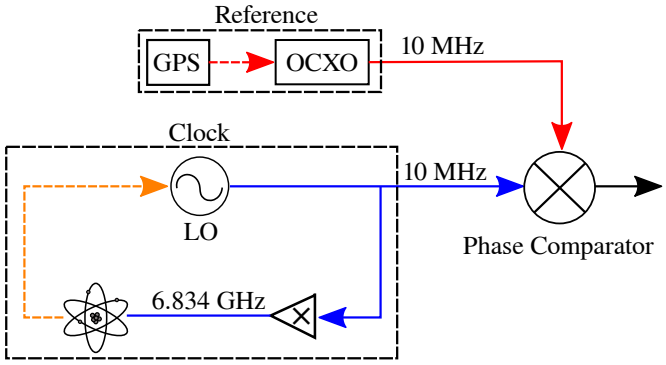

Figure 7.11: General operating principle of the clock and reference oscillator used to measure clock performance.

The performance of the clock is assessed in closed loop, using the constructed error signal to feedback on the the local oscillator (LO). Feedback is applied every two experimental cycles due to the need for a measurement point either side of the central Ramsey fringe (see Sec 7.2). The stability of the clock is then measured by comparing the ≈10 MHz LO against a reference oscillator (discussed in detail in Sec 7.5.5) using a phase comparator (Microchip 53100A). The general scheme for locking and measuring the stability of the clock is shown in in Figure 7.11. The clock stability is then assessed from the resulting fractional frequency array by performing an Overlapping Allan deviation. A typical Allan deviation with the optimised system and a 10 ms Ramsey time is presented in Figure 7.12.

From Figure 7.12 we see that the stability averages down as $1.5 \times 10^{-11}\tau^{-1/2}$ out to 10 s. After this point however the stability deviates slightly from the ideal $\tau^{-1/2}$ dependence out to 100 s where it flatlines. The reasons behind this deviation are discussed in detail in the following section. Also marked on Figure 7.12 is the predicted stability calculated from Eq 7.5, the measured SNR of 111. This line is in reasonable agreement with the measured stability, being out by a factor of approximately 1.7. The reasons behind this disagreement are not currently fully understood.

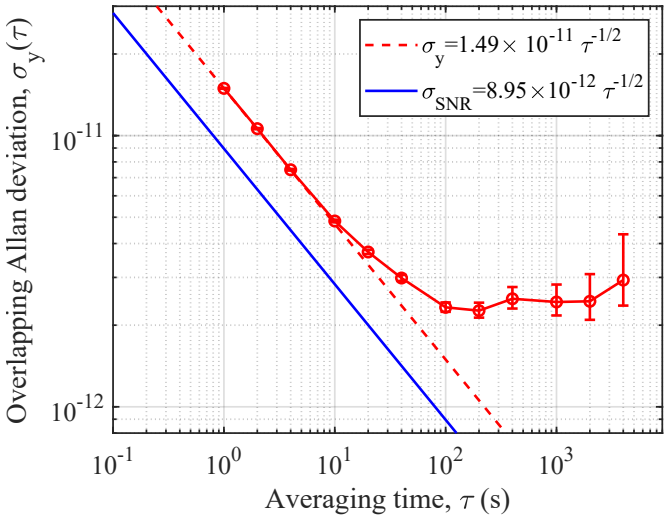

Figure 7.12: Typical Allan deviation of the clock stability measured over around 7 hours. Red points: measured stability. Red dashed line: $\tau^{-1/2}$ dependence of the measured 1 s stability. Blue line: Stability predicted from measured fringe SNR and Eq 7.5.

One of the primary benefits to making a cold-atom atomic clock is the enhanced accuracy over thermal atom counterparts. High accuracy was not a primary goal of the current set-up, for that reason there has been no detailed investigation into systematic shifts on the clock frequency outwith the well-know second order Zeeman shift of around 10 Hz as a result of the 130 mG bias field applied to the atoms. In future it will become necessary to carry out a careful analysis of these systematic shifts, as is done in larger fountain clocks, accounting for effects such as black body shifts and cavity phase shifts.[1]

7.5 Estimation of Noise Contributions

7.5.1 Quantum Projection Noise Limit

If experimental technical noise can been reduced to negligible levels the ultimate limit to clock stability is a result of the quantum nature of the measurement being performed. For the two level system considered here the normalised probability of finding an atom in either state is $|c_1|^2 + |c_2|^2 = 1$. If applying a π pulse to an atom initially in $|1\rangle$, as given by Eq 2.2.2, the final population can be known with certainty: $|c_2|^2 = 1$. This no longer holds in the realistic case of a $\pi/2$ pulse, interrogating the atom at the half maximum point of the Ramsey

fringe. When the final state is measured using the detection beam the atomic wavefunction collapses and is projected into either of the two ground states. In our case, this collapse is a statistical measurement spread over the whole atom cloud, giving the final measured superposition. The uncertainty in this collapse is termed the quantum projection noise (QPN) and was first formalised by Itano *et al.*[166] Here the authors find that the uncertainty of finding an atom in a given state is $\Delta N_{QPN} = \sqrt{Np(1-p)}$[1,166] where N is the number of atoms and p is the excitation fraction ($p = 0.5$ for a $\pi/2$ pulse).

A plot of the measured SNR varying the atom number is presented in Figure 7.13. The blue curve presented in this figure showing the $\sqrt{N}$ relation indicates that in the current system operating with $\approx 3 \times 10^6$ atoms, an SNR of well over 1000 should be possible, around an order of magnitude higher than currently measured. This indicated that if technical noise can be sufficiently suppressed the system is capable of reaching short-term stabilities competitive with other compact cold-atom standards.

The fractional frequency stability of a QPN limited device can be calculated by replacing the SNR factor in Eq 7.5 with $\sqrt{N}$ where N is the number of participating atoms:

$$\sigma_y^{QPN}(\tau) = \frac{1}{\pi}\frac{\Delta f}{f_0}\frac{1}{\sqrt{N}}\sqrt{\frac{T_C}{\tau}}. \tag{7.7}$$

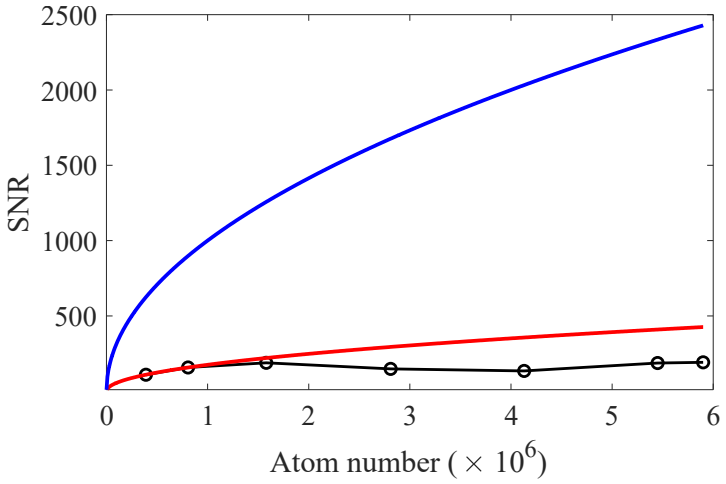

Figure 7.13: Black points: Measured SNR as a function of trapped atom number. Red curve: $\sqrt{N}$ curve, pinned to the first experimental data point. Blue curve: $\sqrt{N}$.

QPN limited SNRs are generally achieved with fluorescence imaging in atomic

fountains,[11,173] however the HORACE experiment has previously demonstrated SNR≥900 using absorption.[143,174] This is encouraging and suggests if various technical noise sources (such as electronics noise in the read out photodiodes) can be reduced this should also be possible in our experiment.

7.5.2 Zeeman Shift

In the first iteration of the clock, magnetic shielding was not included. This design decision was primarily made for the sake of increased optical access to the experiment, useful when characterising the early set-up.[161] While this makes it much simpler to access the experiment, the potential performance of the clock is highly impacted by magnetic field noise. As a simple example, consider a 1% field noise (ΔB) on a 100 mG magnetic bias (B_0) applied to the atoms. The fractional frequency shift to the atomic resonance can be calculated as

$$\frac{df}{f_0} = \frac{2\beta B_0 \Delta B}{f_0}, \tag{7.8}$$

β here is the clock transition's magnetic sensitivity (575 Hz/G^2).[14] This gives a fractional frequency stability limit at the 10^{-12} level.

Clearly this effect is large enough to be of concern in not only the medium and long-term but also at in the short-term if care is not taken to reduce the field noise shot to shot. While impossible to reduce to negligible levels without the introduction of magnetic shielding, this instability can be mitigated somewhat by triggering the experimental cycle off a 50 Hz mains AC line. By initiating the experiment at the same point in the AC cycle each run, shot to shot variations in the magnetic field experienced by the atoms while being interrogated can be minimised.

Practically, triggering is achieved using a Shmitt trigger circuit. This is a comparator circuit that converts the analogue AC mains input to a digital logic output that can be read into the DAQ and used as a trigger. Triggering the experiment in this manner was found to significantly increase the fringe SNR, shown for various trapped atom numbers in Figure 7.14 with and without the Shmitt trigger active. Indicating a reduction in the short-term magnetic field noise due to the 50 Hz mains cycle.

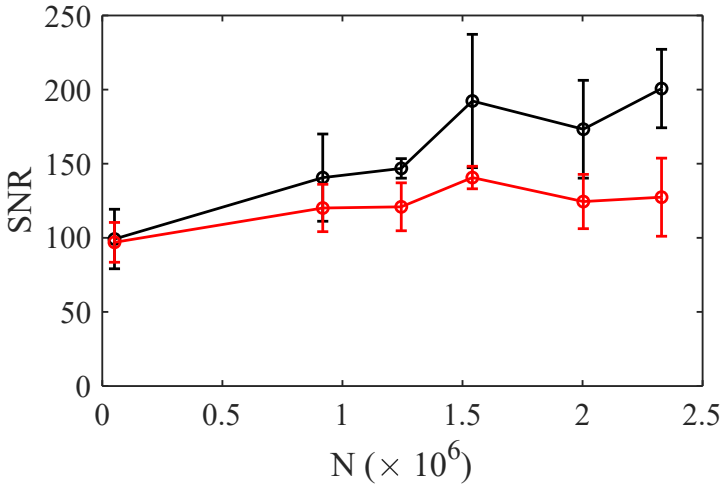

Figure 7.14: Plot showing fringe SNR as a function of trapped atom number triggering the experiment off mains (black) and with no trigger (red). Error bars represent standard error.

While this scheme somewhat mitigates magnetic field noise, the magnetic field stability limit must also measured experimentally to place a lower limit on the achievable stability of the clock for various averaging times. This was achieved by measuring the stability of the $|F = 1, m_F = 1\rangle \rightarrow |F = 2, m_F = 1\rangle$ transition, with the local oscillator locked, and mapping this measurement onto the $m_F = 0 \rightarrow m'_F = 0$ clock transition. By measuring the sensitivity of a much more magnetically sensitive transition ($\beta_{m_F=1} = 1.4$ MHz/G) as opposed to the clock transition which is magnetic field insensitive to first order, a better measurement of magnetic noise should be possible.

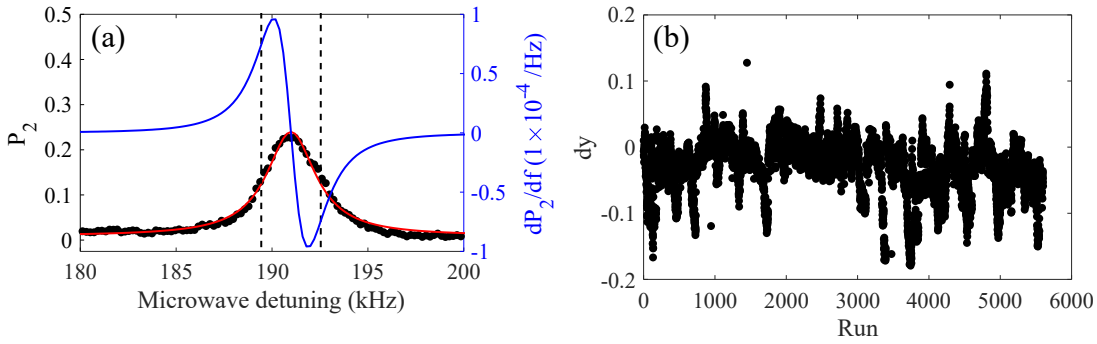

Figure 7.15: (a) Scan over magnetically sensitive Zeeman sublevel transition. Black points: measured data. Red line: Lorentzian fit to the data. Blue line: derivative of the fit. Black dashed line: interrogation points. (b) *dy* array used to calculate the magnetic field stability.

Atoms are prepared in the $|F = 1, m_F = 1\rangle$ state by optically pumping the atomic cloud using the usual $|F = 2\rangle \rightarrow |F = 2\rangle$ transition but instead using roughly σ^+ polarised light with no repump light present. A typical scan over the $|F = 1, m_F = 1\rangle \rightarrow |F = 2, m_F = 1\rangle$ resonance is shown in Figure 7.15. The measurement is performed much as a standard clock operation, probing at the half amplitude points either side of the peak and subtracting the measured populations from each other while the LO is stabilised to GPS. This creates a dy array as shown in Figure 7.15 (b). The dy array is converted to a df array using

$$df_{m_F=1} = \frac{dy}{2m}, \tag{7.9}$$

where m is the features gradient at the probing points. The magnetic field stability can then be calculated as

$$\Delta B = \frac{df_{m_F=1}}{\beta_{m_F=1}}. \tag{7.10}$$

The fractional frequency stability array of the clock transition can then be calculated using Eq 7.8. An Allan deviation is then preformed on the resulting array, shown in Figure 7.16 for different operating conditions.

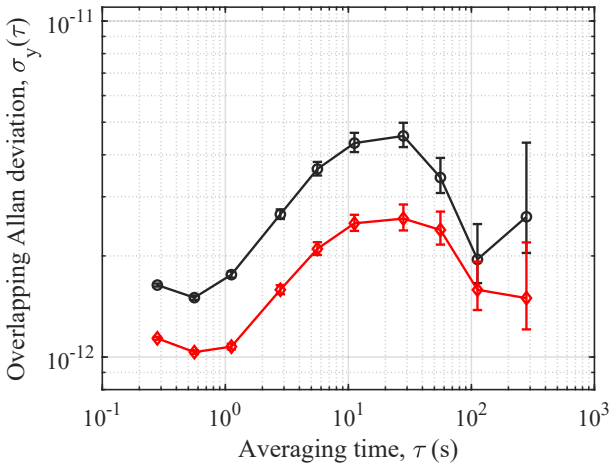

Figure 7.16: Overlapping Allan Deviation of the stability limit due to the second order Zeeman shift. Black circles show the stability limit at a bias field of 288 mG. Red diamonds show stability limit at a bias field of 136 mG.

Figure 7.16 shows that different magnitude bias fields can result in fairly large variations in the stability limit. As expected from Eq 7.8 higher bias fields result in a worse stability, again highlighting the need for magnetic shielding, where the bias field could be decreased further. Some variation in the stability limit

at similar bias fields was also observed day to day, as may be expected from the fairly dynamic magnetic noise environments of an optics lab. From these plots we find a stability limit due to the second order Zeeman shift at the 1×10^{-12} level at $\tau = 1$ s, well below the 1 s SNR limited stability currently possible. A slight bump in the stability limit is observed at around 10 s with the medium-term limit at around 3×10^{-12}.

7.5.3 Dick Effect

In a periodically interrogated frequency reference the phase noise of the local oscillator can be transferred to the clock stability through the Dick effect.[175] When operating in a Ramsey scheme this effect is calculated as[137]

$$\sigma_y^{Dick}(\tau) = \left(\sum_{k=1}^{\infty} sinc^2\left(k\pi \frac{T_R}{T_C}\right) S_y^{LO}\left(\frac{k}{T_C}\right) \right)^{1/2} \tau^{-1/2}, \tag{7.11}$$

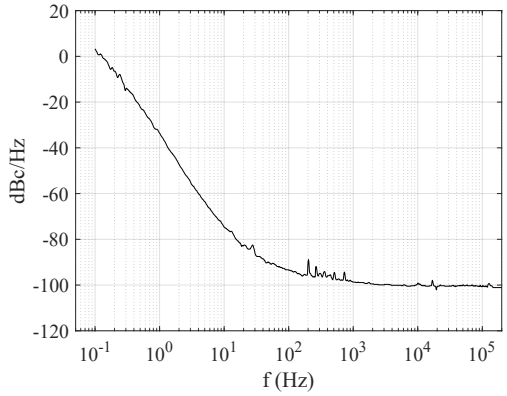

Figure 7.17: Local oscillator phase noise spectrum

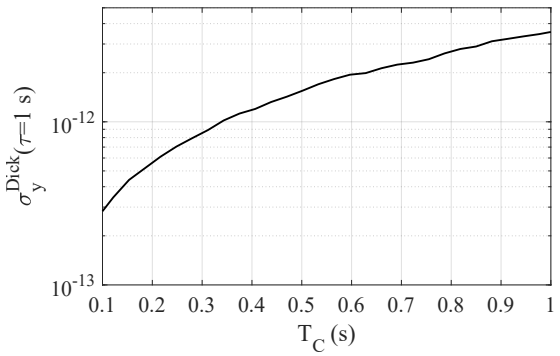

Figure 7.18: Dick effect as a function of experimental cycle time. T_R=10 ms, T_{prep}=30 ms.

where T_R is the Ramsey time, T_C is the experimental cycle time, and S_y^{LO} is the relative frequency noise of the LO, calculated from[176]

$$S_y^{LO} = \left(\frac{f}{f_0}\right)^2 S_\phi(f). \tag{7.12}$$

Here f_0 is the operating frequency, 6.834 GHz, and $S_\phi(f)$ is the power spectral density of the phase noise. The phase noise was experimentally measured using the phase noise analyser (Microchip 53100A) measuring the 10 MHz local oscillator phase noise and scaling this to the noise expected by multiplying this signal to 6.835 GHz. The resulting phase noise spectrum is presented in Figure 7.17. This spectrum assumes the frequency multiplication process does not add any additional phase noise, so the following estimation of the Dick effect is a lower bound estimate. A graph of the Dick effect at $\tau = 1$ s is presented in Figure 7.18 for a 10 ms Ramsey time with an atom preparation and read out time of 30 ms. At the current operating conditions of T_C=140 ms, a lower bound estimation of $4.0 \times 10^{-13}\tau^{-1/2}$ is calculated. This is well below the current 1 s performance of the clock so does not contribute significantly to the clock instability. In future iterations of the clock set-up with improved 1 s stability, this effect will need to be addressed by either reducing the experimental cycle time further or improving the LO in order to reach the short-term stabilities possible of cold-atom systems.

7.5.4 Laser AM and FM Noise

A primary source of noise in optically read out atomic clocks is amplitude noise in the read out beam. It is clear to see that any intensity (AM) or frequency (FM) noise in the read out beam while measuring the state populations results in an AM modulation of the clock error signal. This relative intensity noise (RIN) is subsequently applied to the local oscillator, thus converting the AM noise to FM noise on the clock frequency. To evaluate the extent of this effect in clocks operated in a pulsed mode one can use the formula derived by Calosso *et al.*[177]

$$\sigma_y^{RIN}(\tau) = \frac{2(1-C/2)}{\pi C Q}\left(\sum_{\substack{k>0 \\ k\ odd}}^{\infty} sinc^2\left(\frac{k\pi t_d}{2T_C}\right) S_{RIN}\left(\frac{k}{2T_C}\right)\right)^{1/2} \tau^{-1/2}, \tag{7.13}$$

where C is the fringe contrast, Q is the atomic quality factor ($Q = f_0/\Delta f$), k is an integer, t_d is the time the detection signal is averaged over, T_C the experimental cycle time and S_{RIN} is the power spectral density of the fractional intensity

fluctuations in the probe beam. This effect is similar to the Dick effect in that the probe beam noise is only sampled during the read out phase.

In vapour cell clocks it is possible to repeat the RIN measurement with and without the alkali cell present. This allows the decomposition of probe beam FM and AM noise, as in the first case one measures both FM and AM fluctuations of the probe beam and in the second only the AM component is considered. This is made slightly more complex when working with cold atoms as it is not possible to perform the RIN measurement through the atom cloud without heating and dispersing it through resonant scattering. As a worst case scenario measurement, the RIN was measured through a standard vapour cell with the probe beam frequency positioned half way up the D_2 Doppler resonance. This is not a wholly satisfactory configuration but gives some idea as to the probe FM contribution.

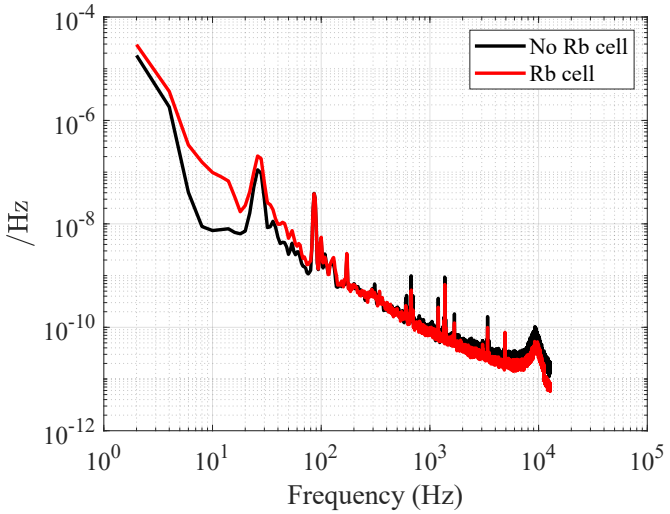

Figure 7.19: Laser RIN spectrum with no Rb cell present (black line) and with the Rb cell present (red line).

After performing the converging sum of Eq 7.13 a stability limit of $1.7 \times 10^{-12}\ \tau^{-1/2}$ and $1.5\ \times 10^{-12}\ \tau^{1/2}$ is found with and without the vapour cell present respectively. This is well below the current stability of the clock, indicating probe beam noise is not limiting clock performance. Interestingly, FM noise on the laser seems to play very little role in the total instability contribution of the measurement, indicating the frequency doubled telecoms laser used throughout the clock investigation has an excellent frequency stability at the frequencies of interest to the clock measurement. If in future the stability of the clock is pushed towards the 10^{-12} level it will be advantageous to reduce intensity noise in the probe beam by introducing feedback onto the read out AOM.

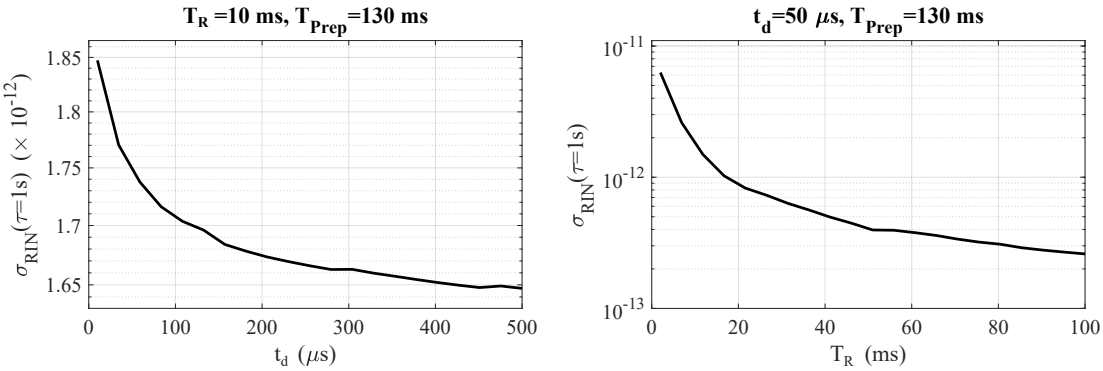

Figure 7.20: Left: 1 s stability limit due to the laser RIN scanning the detection window, t_d. Right: 1 s stability limit due to the laser RIN scanning the Ramsey time, T_R. The atom preparation time and load time, is constant throughout at 130 ms.

The averaging window used in the detection signals, t_d, is currently very short at 50 μs. Using Eq 7.13 it is interesting to scan the averaging time to investigate whether the is any benefit to changing this window. Results of this are shown if Figure 7.20 (a). From this plot we see there is almost no benefit to increasing the detection averaging window, even if the system was currently limited by the probe laser. Similarly, one can scan the Ramsey time, changing Q in Eq 7.13, and observe the effect on the predicted stability limit. Going from the current Ramsey time of 10 ms to the 100 ms Ramsey time, which should be made possible through the atom launch,[161] we see a order of magnitude improvement in the limit due to the probe beam. Once again indicating the strong benefit to performing the launch, assuming the total experimental duty cycle is not inordinately effected.

7.5.5 Reference Oscillator

When measuring the stability of any oscillator it is generally required that the stability of the reference oscillator is significantly better than the device under test. This allows one to associate any deviation in the frequency difference to the device under test. Often masers are used for this purpose as they exhibit excellent short-term and reasonable long-term performance. In lieu of any available masers we use a Wenzel Associates 501-29647 oven controlled crystal oscillator (OCXO) that has been locked to GPS as our reference oscillator. In the following this reference is referred to as GPSDO.

Three-Corner Hat Measurements

In order to evaluate the stability of the GPSDO it is necessary to perform a three-corner hat measurement, where instead of measuring against one high performance reference oscillator, three similarly performing oscillators, each assumed to exhibit independent frequency noise, are compared to each other.[167] Taking each oscillator (labelled A, B, C) and comparing each against the other gives the three frequency stabilities:

$$\begin{aligned} \sigma_{AB}^2 &= \sigma_A^2 + \sigma_B^2 \\ \sigma_{AC}^2 &= \sigma_A^2 + \sigma_C^2 \\ \sigma_{BC}^2 &= \sigma_B^2 + \sigma_C^2. \end{aligned} \tag{7.14}$$

Using simultaneous equations it is then possible to decompose the stability of each oscillator:

$$\begin{aligned} \sigma_A^2 &= \frac{1}{2}(\sigma_{AB}^2 + \sigma_{AC}^2 - \sigma_{BC}^2) \\ \sigma_B^2 &= \frac{1}{2}(\sigma_{AB}^2 + \sigma_{BC}^2 - \sigma_{AC}^2) \\ \sigma_C^2 &= \frac{1}{2}(\sigma_{AC}^2 + \sigma_{BC}^2 - \sigma_{AB}^2). \end{aligned} \tag{7.15}$$

Several similarly performing oscillators are currently available to measure the GPSDO stability against: two Cs beam clocks (Oscilloquartz OSA 3230 and Microchip 5071), a Rb lamp clock (SRS PRS10) and GPS.

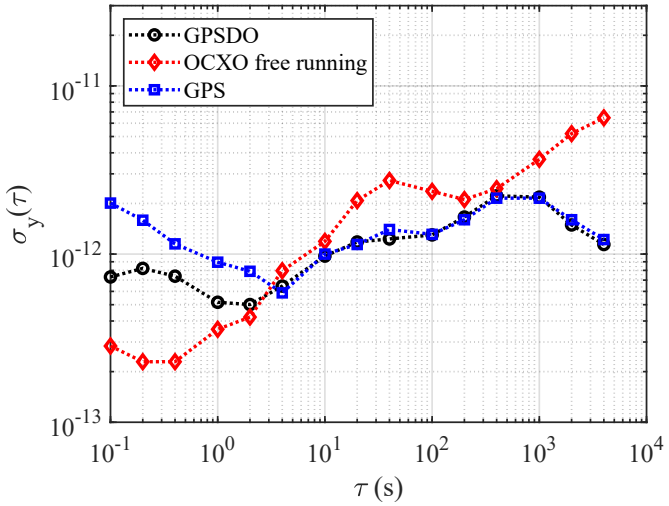

Figure 7.21: Stability of the GPSDO, free running OCXO and GPS, measured using the three-corner hat technique.

The measured stability of the GPSDO, free running OCXO and GPS are shown in Figure 7.21. By referencing the OCXO to GPS it was hoped that we would retain the excellent stability of the OCXO at $\tau < 10$ s with the benefit of good medium to long-term stability from GPS, the most stable reference oscillator available during the measurement campaigns. We see that we do largely retain the good short-term stability of the OCXO with the measured stability almost exactly mapping onto that of the GPS stability at $\tau > 4$ s. A slight bump in the GPSDO stability is observed at ≈ 400 s which helps account for the flattening of the cold-atom clock's measured stability at this time scale, discussed in more detail in Sec 7.5.7.

7.5.6 Locking Electronics

To lock the clock and feedback onto the local oscillator an error signal is constructed as discussed in Sec 7.2. Experimentally the feedback is applied using one of the DAC analogue output channels. This signal is used to voltage tune the LO (Keysight E8257D) frequency which has a tuning coefficient of -0.07 ppm/V. Any voltage noise on this analogue output will be converted into frequency noise on the clock. In addition, due to bit resolution the analogue output step size sets a lower bound on the minimum frequency the LO can be tuned by, imposing a limit to the achievable clock stability.

Typical voltages required to tune the LO to 10 MHz were around 0.7 V, to ensure the highest bit resolution and lowest voltage noise we instead apply 7 V from the DAC and employ a $\times 10$ voltage divider. The minimum voltage step from the 16 bit DAC, set to output (0-10) V is: $V_{Res} = \frac{10V}{10 \times 2^{16}} = 15\ \mu$V, corresponding to a minimum fractional frequency step of 10^{-12}. This minimum frequency tune is slightly below the current performance of the clock but will need to be addressed once future improvements push the stability beyond this level.

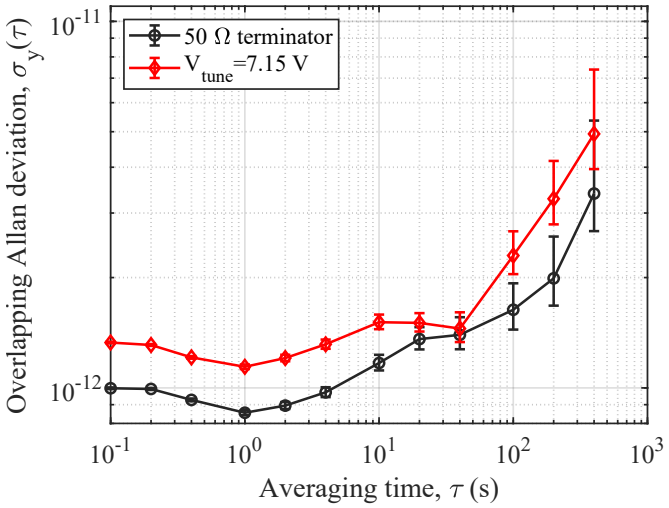

Figure 7.22: Short-term free-running LO stability with 50 Ω terminator in voltage tune port (black circles) and a typical steer voltage from the DAC applied to voltage tune port (red diamonds).

To assess the effect voltage noise has, the 10 MHz signal from the LO is compared against the GPSDO. First with a typical DC voltage applied and then with a 50 Ω terminator in the LO tune port as shown in Figure 7.22. By comparing these two plots we see that voltage noise has a small but currently insignificant effect on the LO stability.

7.5.7 Error Budget

After investigating the various sources of instability in a clock, the results can be collated in an error budget, as shown in Table 7.2. This tabular form provides an easy means to assess the largest instability contributors and whether any instability sources are unaccounted for by comparing the measured stability against the sum of the known instability sources.

From Table 7.2 we see that the fringe SNR currently dominates the 1 s stability of the clock. Future work on this project must therefore initially focus on the reduction of this noise source in order to push the clock stability towards the QPN limit. In Sec 7.5.4 the clock instability due to the read out lasers AM and FM noise was investigated and measured to contribute well below the current SNR limit. The limiting factor to the SNR must therefore be sought elsewhere. Other than the SNR contribution the other noise sources are at the low 10^{-12} to mid 10^{-13} level and have a limited contribution to the 1 s stability of the clock. When the total predicted instability is compared to the measured 1 s stability of

the clock we find the measured stability is a factor of around 1.7 worse. While this is a reasonable agreement, it is clear that a non-trivial instability source is as yet unaccounted for.

Noise source	σ contribution ($\tau = 1s$)
SNR	8.95×10^{-12}
Electronic noise	1.14×10^{-12}
Dick	4.00×10^{-13}
Zeeman	1.07×10^{-12}
QPN	4.90×10^{-13}
Total $\left(\sqrt{\sum \sigma_n^2}\right)$	9.03×10^{-12}
Measured	1.49×10^{-11}

Table 7.2: Table of noise sources and their contributions to the 1 s Allan deviations stability.

When the clock stability is plotted on the same Allan deviation plot as the Zeeman shift stability limit (Sec 7.5.2) and the reference oscillator stability (Sec 7.5.5) the reasons for the behaviour of the clock in the medium-term becomes clear. We see that after initially averaging down with an ideal $\tau^{-1/2}$ gradient the measured stability departs from this line at approximately 10 s. This intersects almost exactly with the stability limit due to the second order Zeeman shift on the clock transition as a result of the experiment being magnetically unshilded. Furthermore, we see that after this point at around 600 s the stability limit due to the reference oscillator also intersects with the measured clock stability. The combination of these two limits accounts for the flatlining of the clock stability in the medium-term at around 1×10^{-12}. This plot gives an excellent basis for future optimisation of the set-up.

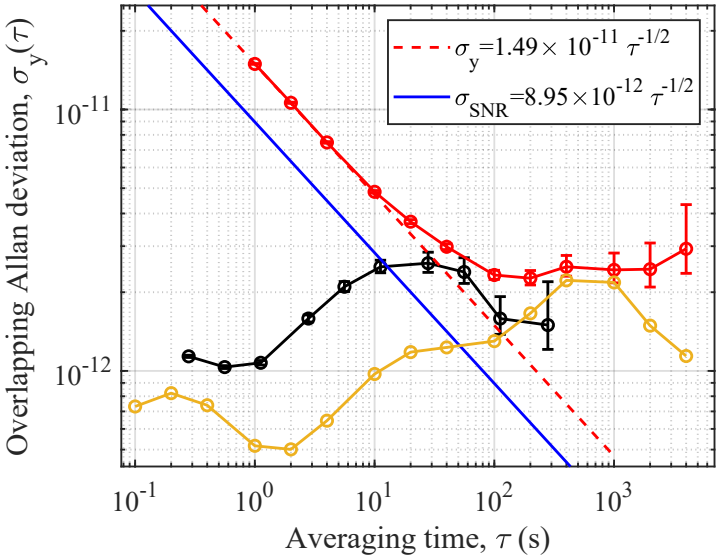

Figure 7.23: Red points: Overlapping Allan deviation of local oscillator's stability when locked to atomic signal. Blue solid line: stability predicted by (Eq 7.5) and measured fringe SNR. Red dashed line: $\tau^{-1/2}$ dependence of the measured 1 s stability. Black points: stability limit due to the second-order Zeeman shift. Yellow points: measured GPSDO reference oscillator stability.

7.6 Conclusion and Future Work

In conclusion, a compact cold-atom microwave clock based on an additively manufactured loop-gap-resonator cavity interacting with laser cooled atoms loaded from a GMOT chip has been demonstrated. In the present system the experimentally optimised short-term clock stability is measured as $\sigma_y(\tau) = 1.5\times10^{-11}\ \tau^{-1/2}$, primarily limited by the Ramsey fringe SNR. In the medium-term the clock stability is primarily limited by the second-order Zeeman shift due to operating in an unshilded environment. A secondary limit is placed on the medium-term stability performance by the reference oscillator itself exhibiting a stability bump at around 700 s. By addressing these issues, the short-term stability is expected to be improved to be more in line with other cold-atom cavity clock demonstrations.[142,146–148]

Future work on the clock performance should include introducing magnetic shielding and thorough investigation of the short-term stability limit in order to reconcile the difference in expected and observed short term-stability. This will most likely include a careful optimisation of the read out scheme with lower noise photodiodes and a concerted effort to reduce electronic noise in the system

as a whole. Actively feeding back onto the read out beam intensity alongside a dedicated study of the optimum intensity to use could also prove beneficial. It may eventually prove fruitful to investigate other noise sources such as microwave power fluctuations if the clock performance can be driven to increased stabilities.[154]

The current physics package is inherently compact and remains highly amenable to further miniaturisation. The use of additive manufacturing also maintains a highly scalable manufacturing process. Additively manufactured vacuum chambers have also recently demonstrated compatibility with UHV[160] pressure levels. This raises the enticing possibility of the cavity body itself simultaneously acting as a UHV chamber, allowing the entire physics package to be manufactured as a single bulk component, drastically reducing the size of the system. In addition to this, passively pumped vacuum chambers have now been shown to maintain the UHV levels required for atom trapping for extended periods,[77,78] allowing for a reduction in power consumption by negating the continuous use of an ion pump.

Whilst the stability performance of our clock is currently 10-50 times below the state-of-the-art commercial offerings,[147–149] similar performances should be possible with the discussed improvements to the system. With more focus on system integration in a second generation of the clock, the experiment size should also be much improved, in line or even smaller than current offerings due to the highly compact physics package. We therefore believe this work represents a step towards highly compact and portable cold-atom frequency standards.

Chapter 8

Conclusion

This thesis has described several distinct investigations into enabling technologies towards a more compact next generation of cold-atom sensors. Grating magneto-optical traps form the heart of all these investigations with each experiment addressing a different sub-system required for future cold-atom sensors.

In Chapter 4 microfabricated components for the reduction of the overall size of laser cooling platforms were investigated. The first half of this chapter discussed microfabricated vacuum chambers. Experiments here centred around the specific issues of imaging the atom clouds, along with ways to improve upon the maximum trapped atom number observed within these compact cells. Both these investigations were a success, proving it is possible to image atoms trapped by a GMOT in these silicon based cells through the hole in the grating chip. Previous demonstrations with these cells found imaging and atom number extraction difficult, relying on a two photon excitation of the cloud along with band pass filters to reduced the scattered light levels and reveal the MOT.[79] Here it has been shown that it is possible to use the trap beam itself for an absorption imaging sequence on the atoms through a hole in the grating chip. This solution is much more compact when compared to previous two-photon excitation as no additional lasers outwith the normal trapping laser are required. Similarly, methods of increasing the trapped atom number in these compact cells were proposed and later demonstrated successful. Due to the reduced vacuum volume of the compact cell, much of the grating optical overlap volume was not within the chamber, reducing the number of trapped atoms. By increasing the thickness of the cells it has subsequently been demonstrated that atom numbers in line with traditional vacuum chambers are possible in these silicon vacuum chambers.[90]

In the second portion of this chapter, MEMS scanning mirrors were success-

fully integrated with a GMOT and used to paint hyperfine repump light potentials onto a cloud of atoms optically pumped into a dark state. By painting this light, localised fluorescence of the atom cloud is observed in various patterns: line, circle and square. This proof of principle investigation shows it is possible to locally address cold-atom clouds with these microfabricated mirrors, potentially negating the need for high power AOMs in future chip-scale devices.

Chapter 5 discussed the integration GMOT technology with optical lattices created by reflecting/diffracting a single lattice beam off the same grating chip. Strong evidence for the formation of the 1D and 3D lattice geometries was demonstrated in this manner by aligning to different sections of the grating chip and utilising appropriate wavelengths of light. By using the same optic to first load and cool atoms into a MOT and then load an optical lattice, the optical system required for lattice experiments is much simplified and reduced. This has the added benefit that all the lattice beams used to form the interference pattern share a common phase. Any variation in this phase therefore, either via laser noise or mechanical noise, is common to all beams. This creates a much more stable lattice structure where sensitivity to acoustic vibrations is reduced. The added stability and ease of alignment of this system is ideally suited for future compact optical lattice clocks by extending this proof-of-principle experiment to other elements such as strontium.

Finally, in Chapter 6-7 the system architecture for a new cold-atom microwave clock based around an additively manufactured loop-gap-resonator microwave cavity and GMOT was introduced and characterised. This system was able to demonstrate high contrast Ramsey fringes for Ramsey times up to 20 ms, limited by the drop in SNR as the atom cloud falls out of the probe beam. Further to this, a working clock using the atomic feedback to steer a 10 MHz quartz oscillator in closed loop operation was also demonstrated. Initial performance of this system was demonstrated to be at the 10^{-11} level at 1 s, limited by fringe SNR. In the medium term the clock stability initially averages down with an ideal $1/\sqrt{\tau}$ dependence before reaching a flicker noise floor at the 10^{-12} level due to the duel effect of magnetic field noise and a slight drift of the reference oscillator at longer time scales. Additive manufacturing of the microwave cavity was found to have no noticeable impact on the vacuum quality with a dedicated study on the material outgassing properties being carried out. This physics package and method of fabrication is ideally suited to more large-scale production due to the high manufacturing tolerances and ease of production afforded by additive

manufacturing of the cavity body.

8.1 Future Work

8.1.1 Microfabricated components

Future work in this area should be centred around the demonstration of passive pumping in the compact vacuum cells for extended periods of at least a year, though ideally more. If this can be demonstrated it will significantly reduce the size and power consumption of these compact vacuum chambers even more by negating the need for an ion pump. These systems are ideally suited to portable cold-atom sensors of various types. In addition to this, integration of on-chip laser systems is currently progressing in leaps and bounds. A recent demonstration of an integrated chip based laser systems was made where the authors demonstrated a working interferometer using cold atoms trapped in a titanium vacuum cell.[72] A fully integrated, on-chip sensor is therefore no longer a distant possibility and would open the door to more widespread adoption of cold-atom technology by significantly reducing the manufacturing cost and complexity of these devices. By utilising a vacuum chamber made with similar MEMS processes the manufacturing and integration complexity should be much reduced in future devices.

8.1.2 On-chip optical lattice

Future work in this area should focus on the extension of the techniques demonstrated here in ^{87}Rb to other elements, namely the alkaline-earths. This should open the possibility for a much simplified optical delivery system for both clocks and interferomenters based around atoms trapped in optical lattices. It may also be interesting to investigate different diffraction grating structures and how they effect the lattice crystalline structure. Improved models of the lattice structure will likely also be of benefit, accounting for additional effects such as beam polarisation. Integration of gratings with magnetic chip traps is also of great interest and is actively under investigation by the group in Leibniz University Hannover in collaboration with the University of Strathclyde. The integration of these additional trap types allows for the formation of Bose-Einstein condensates fully on chip which can then be loaded into the optical lattice and manipulated further.

Similar experiments have now been demonstrated in micro-gravity on the International Space Station[178] and it is easy to see how further integration of GMOTs with chip traps and lattices could be of interest as this sort of technology becomes more widespread.

8.1.3 Compact cold-atom microwave clock

Work on the cold-atom microwave clock going forward must focus on two distinct areas: firstly improvements to the clock performance in both the short and long-term. This will be achieved by improving the detection system and reducing electronic noise as a whole, along with the introduction of magnetic shielding. Due to ease of access during early characterisation magnetic shielding has been left out of Generation 1, this must be rectified for future generations in order to fully leverage the benefits offered by cold-atom clocks. A bonus goal would be the introduction of an atom launch in the sequence. This would allow longer Ramsey times and improved short-term stability of the clock. While not strictly required to reach stabilities at the stated performance goal of $\approx 10^{-13}$ at 1 s, the increased performance offered by a launch is still an attractive prospect. This could allow the clock to run in two operational modes: one with a high cycle rate and good performance, and a second mode with slightly improved performance at the cost of a lower cycle rate and higher sensitivity to effects such as mechanical vibrations.

A second major area of improvement to the clock should focus on system integration. The eventual goal here is to create a high-performance clock that fits entirely into a 19 inch rack. This goal is feasible but will require careful work in several key areas so as to reach the high performance demanded while maintaining a compact package. A first obvious step to greater system integration is creating a microwave cavity that is also able to act as the vacuum chamber. This should be possible with current technology[77,78] with a first demonstration likely still maintaining UHV via active pumping. In time, UHV pressures could be maintained by passive pumping alone (at least intermittently) which will additionally reduce power consumption of the clock. The next major area of system integration is the laser system and wider optical set-up. This should be of low enough frequency and intensity noise to allow high SNR Ramsey fringes to be measured while maintaining as compact a form factor as possible. In addition, the laser system should be robust against various temperature, pressure and vi-

brational environments without degradation to its performance.

Bibliography

[1] F. Riehle, *Frequency Standards* (Wiley-VHC, 2004).

[2] N. Dimarcq *et al.*, *Roadmap towards the redefinition of the second*, Metrologia **61**, 012001 (2024).

[3] F. G. Major, *Quo Vadis: Evolution of Modern Navigation* (Springer New York, 2014).

[4] UK Parliament, *Facts and figures: Big Ben and Elizabeth Tower*, Available Online at https://www.parliament.uk/about/living-heritage/building/palace/big-ben/facts-figures/, Accessed Nov 2023.

[5] J. D. Prestage, R. L. Tjoelker, and L. Maleki, *Atomic Clocks and Variations of the Fine Structure Constant*, Physical Review Letters **74**, 3511 (1995).

[6] B. L. S. Marlow and D. R. Scherer, *A Review of Commercial and Emerging Atomic Frequency Standards*, IEEE Transactions on Ultrasonics, Ferroelectrics, and Frequency Control **68**, 2007 (2021).

[7] T. Bothwell *et al.*, *Resolving the gravitational redshift across a millimetre-scale atomic sample*, Nature **602**, 420 (2022).

[8] S. Knappe *et al.*, *A microfabricated atomic clock*, Applied Physics Letters **85**, 1460 (2004).

[9] *Success Story: Chip-Scale Atomic Clocks*, Available Online at https://www.nist.gov/noac/success-story-chip-scale-atomic-clock, Accessed Nov 2023.

[10] A. D. Ludlow, M. M. Boyd, J. Ye, E. Peik, and P. Schmidt, *Optical atomic clocks*, Reviews of Modern Physics **87**, 637 (2015).

[11] R. Wynands and S. Weyers, *Atomic fountain clocks*, Metrologia **42**, S64 (2005).

[12] X. Zheng *et al.*, *Differential clock comparisons with a multiplexed optical lattice clock*, Nature **602**, 425 (2022).

[13] C. J. Foot, *Atomic Physics* (Oxford University Press, 2014).

[14] D. A. Steck, *Rubidium 87 D Line Data*, Available Online at http://steck.us/alkalidata, Version 2.1.5.

[15] P. R. Berman, *Atom interferometry* (Academic press, 1997).

[16] D. W. Sesko and C. E. Wieman, *Observation of the cesium clock transition in laser-cooled atoms*, Optics Letters **14**, 269 (1989).

[17] N. F. Ramsey, *A Molecular Beam Resonance Method with Separated Oscillating Fields*, Physical Review **78**, 695 (1950).

[18] N. F. Ramsey, *Experiments with separated oscillatory fields and hydrogen masers*, Reviews of Modern Physics **62**, 541 (1990).

[19] M. A. Kasevich, E. Riis, S. Chu, and R. G. DeVoe, *rf spectroscopy in an atomic fountain*, Physical Review Letters **63**, 612 (1989).

[20] D. A. Steck, *Rubidium 85 D Line Data*, Available Online at http://steck.us/alkalidata, Version 2.1.6.

[21] C. E. Wieman and L. Hollberg, *Using diode lasers for atomic physics*, Review of Scientific Instruments **62**, 1 (1991).

[22] W. D. Phillips and H. Metcalf, *Laser Deceleration of an Atomic Beam*, Physical Review Letters **48**, 596 (1982).

[23] S. Chu, L. Hollberg, J. E. Bjorkholm, A. Cable, and A. Ashkin, *Three-dimensional viscous confinement and cooling of atoms by resonance radiation pressure*, Physical Review Letters **55**, 48 (1985).

[24] E. L. Raab, M. Prentiss, A. Cable, S. Chu, and D. E. Pritchard, *Trapping of Neutral Sodium Atoms with Radiation Pressure*, Physical Review Letters **59**, 2631 (1987).

[25] W. D. Phillips, *Nobel Lecture: Laser cooling and trapping of neutral atoms*, Reviews of Modern Physics **70**, 721 (1998).

[26] S. Chu, *Nobel Lecture: The manipulation of neutral particles*, Reviews of Modern Physics **70**, 685 (1998).

[27] C. N. Cohen-Tannoudji, *Nobel Lecture: Manipulating atoms with photons*, Reviews of Modern Physics **70**, 707 (1998).

[28] C. Adams and E. Riis, *Laser cooling and trapping of neutral atoms*, Progress in Quantum Electronics **21**, 1 (1997).

[29] H. J. Metcalf and P. van der Straten, *Laser cooling and trapping of atoms*, Journal of the Optical Society of America B **20**, 887 (2003).

[30] P. D. Lett *et al.*, *Optical molasses*, Journal of the Optical Society of America B **6**, 2084 (1989).

[31] J. Reichel, W. Hänsel, and T. W. Hänsch, *Atomic Micromanipulation with Magnetic Surface Traps*, Physical Review Letters **83**, 3398 (1999).

[32] K. I. Lee, J. A. Kim, H. R. Noh, and W. Jhe, *Single-beam atom trap in a pyramidal and conical hollow mirror*, Optics Letters **21**, 1177 (1996).

[33] F. Shimizu, K. Shimizu, and H. Takuma, *Four-beam laser trap of neutral atoms*, Optics Letters **16**, 339 (1991).

[34] C. C. Nshii *et al.*, *A surface-patterned chip as a strong source of ultracold atoms for quantum technologies*, Nature Nanotechnology **8**, 321 (2013).

[35] L. Zhu *et al.*, *A dielectric metasurface optical chip for the generation of cold atoms*, Science Advances **6**, eabb6667 (2020).

[36] S. Bondza, T. Leopold, R. Schwarz, and C. Lisdat, *Achromatic, planar Fresnel-Reflector for a Single-beam Magneto-optical Trap*, 2023, arXiv:2310.14861.

[37] J. P. McGilligan, P. F. Griffin, E. Riis, and A. S. Arnold, *Phase-space properties of magneto-optical traps utilising micro-fabricated gratings*, Optics Express **23**, 8948 (2015).

[38] J. P. McGilligan, P. F. Griffin, E. Riis, and A. S. Arnold, *Diffraction-grating characterization for cold-atom experiments*, Journal of the Optical Society of America B **33**, 1271 (2016).

[39] J. P. McGilligan *et al.*, *Grating chips for quantum technologies*, Scientific Reports **7**, 384 (2017).

[40] M. Vangeleyn, P. F. Griffin, E. Riis, and A. S. Arnold, *Single-laser, one beam, tetrahedral magneto-optical trap*, Optics Express **17**, 13601 (2009).

[41] M. Vangeleyn, P. F. Griffin, E. Riis, and A. S. Arnold, *Laser cooling with a single laser beam and a planar diffractor*, Optics Letters **35**, 3453 (2010).

[42] M. Vangeleyn, *Atom trapping in non-trivial geometries for micro-fabrication applications*, PhD thesis, University of Strathclyde, 2011.

[43] J. P. McGilligan, *Micro-fabricated Diffractive Optics for Quantum Sensors and Atomic Clocks*, PhD thesis, University of Strathclyde, 2017.

[44] H. Heine, *A high-flux cold atom source based on a nano-structured atom chip*, PhD thesis, Leibniz University Hannover, 2023.

[45] A. Sitaram *et al.*, *Confinement of an alkaline-earth element in a grating magneto-optical trap*, Review of Scientific Instruments **91**, 103202 (2020).

[46] S. Bondza, C. Lisdat, S. Kroker, and T. Leopold, *Two-Color Grating Magneto-Optical Trap for Narrow-Line Laser Cooling*, Physical Review Applied **17**, 044002 (2022).

[47] O. S. Burrow *et al.*, *Optimal binary gratings for multi-wavelength magneto-optical traps*, Optics Express **31**, 40871 (2023).

[48] P. D. Lett *et al.*, *Observation of Atoms Laser Cooled below the Doppler Limit*, Physical Review Letters **61**, 169 (1988).

[49] J. Dalibard and C. Cohen-Tannoudji, *Laser cooling below the Doppler limit by polarization gradients: simple theoretical models*, Journal of the Optical Society of America B **6**, 2023 (1989).

[50] D. Boiron *et al.*, *Laser cooling of cesium atoms in gray optical molasses down to 1.1 μK*, Physical Review A **53**, R3734 (1996).

[51] S. Rosi *et al.*, Λ *-enhanced grey molasses on the D2 transition of Rubidium-87 atoms*, Scientific Reports **8**, 1301 (2018).

[52] A. Arnold, *Preparation and Manipulation of an ^{87}Rb Bose-Einstein Condensate*, PhD thesis, University of Sussex, 1999.

[53] G. Grynberg and J.-Y. Courtois, *Proposal for a Magneto-Optical Lattice for Trapping Atoms in Nearly-Dark States*, Europhysics Letters (EPL) **27**, 41 (1994).

[54] M. Weidemüller, T. Esslinger, M. A. Ol'shanii, A. Hemmerich, and T. W. Hänsch, *A Novel Scheme for Efficient Cooling below the Photon Recoil Limit*, Europhysics Letters (EPL) **27**, 109 (1994).

[55] J. P. McGilligan *et al.*, *Micro-fabricated components for cold atom sensors*, Review of Scientific Instruments **93**, 091101 (2022).

[56] A. S. Arnold, J. S. Wilson, and M. G. Boshier, *A simple extended-cavity diode laser*, Review of Scientific Instruments **69**, 1236 (1998).

[57] D. W. Preston, *Doppler-free saturated absorption: Laser spectroscopy*, American Journal of Physics **64**, 1432 (1996).

[58] *Muquans ILS product series*, Available Online at https://www.muquans.com/, Accessed Jan 2023.

[59] T. Lévèque, L. Antoni-Micollier, B. Faure, and J. Berthon, *A laser setup for rubidium cooling dedicated to space applications*, Applied Physics B **116**, 997 (2014).

[60] *Tunable Cateye Lasers (CEL)*, Available Online at https://www.moglabs.com/products/cateye-laser, Accessed Oct 2023.

[61] *Ytterbium Continuous Wave Fiber Lasers*, Available Online at https://www.ipgphotonics.com/en/products/lasers/low-power-cw-fiber-lasers/0-98-1-1-micron/ylm-and-ylr-1-100-w#[ylm], Accessed Oct 2023.

[62] E. A. Donley, T. P. Heavner, F. Levi, M. O. Tataw, and S. R. Jefferts, *Double-pass acousto-optic modulator system*, Review of Scientific Instruments **76**, 063112 (2005).

[63] W. R. McGehee *et al.*, *Magneto-optical trapping using planar optics*, New Journal of Physics **23**, 013021 (2021).

[64] B. Oliver, J. G. Bradley, and H. Farrar, *Helium concentration in the Earth's lower atmosphere*, Geochimica et Cosmochimica Acta **48**, 1759 (1984).

[65] SAES, *ALKALI METALS DISPENSERS*, Available Online at https://www.saesgetters.com/products-functions/products/dispensers/alkali-metals-dispensers, Accessed March 2023.

[66] T. Arpornthip, C. A. Sackett, and K. J. Hughes, *Vacuum-pressure measurement using a magneto-optical trap*, Physical Review A **85**, 033420 (2012).

[67] R. W. G. Moore *et al.*, *Measurement of vacuum pressure with a magneto-optical trap: A pressure-rise method*, Review of Scientific Instruments **86**, 093108 (2015).

[68] D. S. Barker *et al.*, *Λ-enhanced gray molasses in a tetrahedral laser beam geometry*, Optics Express **30**, 9959 (2022).

[69] A. Suleymanzade, *Millimeter Wave Photons for Hybrid Quantum Systems*, PhD thesis, University of Chicago, 2021.

[70] I. Despard, *The Construction of a Bosonic Quantum-Gas Microscope*, PhD thesis, University of Strathclyde, 2022.

[71] J. A. Rushton, M. Aldous, and M. D. Himsworth, *Contributed Review: The feasibility of a fully miniaturized magneto-optical trap for portable ultracold quantum technology*, Review of Scientific Instruments **85**, 121501 (2014).

[72] J. Lee *et al.*, *A compact cold-atom interferometer with a high data-rate grating magneto-optical trap and a photonic-integrated-circuit-compatible laser system*, Nature Communications **13**, 5131 (2022).

[73] A. Isichenko *et al.*, *Photonic integrated beam delivery for a rubidium 3D magneto-optical trap*, Nature Communications **14**, 3080 (2023).

[74] A. Bregazzi *et al.*, *A simple imaging solution for chip-scale laser cooling*, Applied Physics Letters **119**, 184002 (2021).

[75] A. Bregazzi *et al.*, *Cold-atom shaping with MEMS scanning mirrors*, Optics Letters **48**, 37 (2022).

[76] Y.-Y. Jau *et al.*, *Low-power, miniature ^{171}Yb ion clock using an ultra-small vacuum package*, Applied Physics Letters **101**, 253518 (2012).

[77] B. J. Little *et al.*, *A passively pumped vacuum package sustaining cold atoms for more than 200 days*, AVS Quantum Science **3**, 035001 (2021).

[78] O. S. Burrow *et al.*, *Stand-alone vacuum cell for compact ultracold quantum technologies*, Applied Physics Letters **119**, 124002 (2021).

[79] J. P. McGilligan *et al.*, *Laser cooling in a chip-scale platform*, Applied Physics Letters **117**, 054001 (2020).

[80] R. Boudot *et al.*, *Enhanced observation time of magneto-optical traps using micro-machined non-evaporable getter pumps*, Scientific Reports **10**, 16590 (2020).

[81] A. T. Dellis, V. Shah, E. A. Donley, S. Knappe, and J. Kitching, *Low helium permeation cells for atomic microsystems technology*, Optics Letters **41**, 2775 (2016).

[82] E. Imhof *et al.*, *Two-dimensional grating magneto-optical trap*, Physical Review A **96**, 033636 (2017).

[83] J. Franssen, T. de Raadt, M. van Ninhuijs, and O. Luiten, *Compact ultracold electron source based on a grating magneto-optical trap*, Physical Review Accelerators and Beams **22**, 023401 (2019).

[84] D. Barker *et al.*, *Single-Beam Zeeman Slower and Magneto-Optical Trap Using a Nanofabricated Grating*, Physical Review Applied **11**, 064023 (2019).

[85] K. Lindquist, M. Stephens, and C. Wieman, *Experimental and theoretical study of the vapor-cell Zeeman optical trap*, Physical Review A **46**, 4082 (1992).

[86] K. E. Gibble, S. Kasapi, and S. Chu, *Improved magneto-optic trapping in a vapor cell*, Optics Letters **17**, 526 (1992).

[87] G. W. Hoth, E. A. Donley, and J. Kitching, *Atom number in magneto-optic traps with millimeter scale laser beams*, Optics Letters **38**, 661 (2013).

[88] S. Pollock, J. P. Cotter, A. Laliotis, F. Ramirez-Martinez, and E. A. Hinds, *Characteristics of integrated magneto-optical traps for atom chips*, New Journal of Physics **13**, 043029 (2011).

[89] S. Dyer *et al.*, *Micro-machined deep silicon atomic vapor cells*, Journal of Applied Physics **132**, 134401 (2022).

[90] S. Dyer *et al.*, *Chip-Scale Packages for a Tunable Wavelength Reference and Laser Cooling Platform*, Physical Review Applied **19**, 044015 (2023).

[91] L. Niu *et al.*, *Optimized fringe removal algorithm for absorption images*, Applied Physics Letters **113**, 144103 (2018).

[92] F. Xiong, Y. Long, and C. V. Parker, *Enhanced principle component method for fringe removal in cold atom images*, Journal of the Optical Society of America B **37**, 2041 (2020).

[93] R. Grimm, M. Weidemüller, and Y. B. Ovchinnikov, *Optical Dipole Traps for Neutral Atoms*, in *Advances In Atomic, Molecular, and Optical Physics*, pp. 95–170, Elsevier, 2000.

[94] D. Barredo, S. de Léséleuc, V. Lienhard, T. Lahaye, and A. Browaeys, *An atom-by-atom assembler of defect-free arbitrary two-dimensional atomic arrays*, Science **354**, 1021 (2016).

[95] F. Nogrette *et al.*, *Single-Atom Trapping in Holographic 2D Arrays of Microtraps with Arbitrary Geometries*, Physical Review X **4**, 021034 (2014).

[96] D. Stuart and A. Kuhn, *Single-atom trapping and transport in DMD-controlled optical tweezers*, New Journal of Physics **20**, 023013 (2018).

[97] K. Henderson, C. Ryu, C. MacCormick, and M. G. Boshier, *Experimental demonstration of painting arbitrary and dynamic potentials for Bose–Einstein condensates*, New Journal of Physics **11**, 043030 (2009).

[98] T. A. Bell *et al.*, *Bose–Einstein condensation in large time-averaged optical ring potentials*, New Journal of Physics **18**, 089501 (2016).

[99] C. Knoernschild *et al.*, *Independent individual addressing of multiple neutral atom qubits with a micromirror-based beam steering system*, Applied Physics Letters **97**, 134101 (2010).

[100] S. Crain, E. Mount, S. Baek, and J. Kim, *Individual addressing of trapped 171Yb+ ion qubits using a microelectromechanical systems-based beam steering system*, Applied Physics Letters **105**, 181115 (2014).

[101] Y. Wang *et al.*, *High-Fidelity Two-Qubit Gates Using a Microelectromechanical-System-Based Beam Steering System for Individual Qubit Addressing*, Physical Review Letters **125**, 150505 (2020).

[102] S. Kim, R. R. Mcleod, M. Saffman, and K. H. Wagner, *Doppler-free, multiwavelength acousto-optic deflector for two-photon addressing arrays of Rb atoms in a quantum information processor*, Applied Optics **47**, 1816 (2008).

[103] P. Janin, *MEMS Devices for the Control of Trapped Atomic Particles*, PhD thesis, University of Strathclyde, 2022.

[104] P. Janin, D. Uttamchandani, and R. Bauer, *On-Chip Frequency Tuning of Fast Resonant MEMS Scanner*, Journal of Microelectromechanical Systems **31**, 977 (2022).

[105] M. Shuker, O. Firstenberg, R. Pugatch, A. Ron, and N. Davidson, *Storing Images in Warm Atomic Vapor*, Physical Review Letters **100**, 223601 (2008).

[106] B. Peaudecerf, M. Andia, M. Brown, E. Haller, and S. Kuhr, *Microwave preparation of two-dimensional fermionic spin mixtures*, New Journal of Physics **21**, 013020 (2019).

[107] C. Ryu and M. G. Boshier, *Integrated coherent matter wave circuits*, New Journal of Physics **17**, 092002 (2015).

[108] Y. B. Ovchinnikov, *A perspective on integrated atomo-photonic waveguide circuits*, Applied Physics Letters **120**, 010502 (2022).

[109] J. F. Sherson *et al.*, *Single-atom-resolved fluorescence imaging of an atomic Mott insulator*, Nature **467**, 68 (2010).

[110] M. Takamoto *et al.*, *Test of general relativity by a pair of transportable optical lattice clocks*, Nature Photonics **14**, 411 (2020).

[111] J. Grotti *et al.*, *Geodesy and metrology with a transportable optical clock*, Nature Physics **14**, 437 (2018).

[112] W. Bowden *et al.*, *A pyramid MOT with integrated optical cavities as a cold atom platform for an optical lattice clock*, Scientific Reports **9**, 11704 (2019).

[113] A. R. Ferdinand *et al.*, *A scalable infrastructure for strontium optical clocks*, in *2022 Conference on Lasers and Electro-Optics (CLEO)*, pp. 1–2, 2022.

[114] D. Gallego, S. Hofferberth, T. Schumm, P. Krüger, and J. Schmiedmayer, *Optical lattice on an atom chip*, Optics Letters **34**, 3463 (2009).

[115] C. J. E. Straatsma *et al.*, *On-chip optical lattice for cold atom experiments*, Optics Letters **40**, 3368 (2015).

[116] S. A. Hopkins and A. V. Durrant, *Parameters for polarization gradients in three-dimensional electromagnetic standing waves*, Physical Review A **56**, 4012–4022 (1997).

[117] A. Rauschenbeutel, H. Schadwinkel, V. Gomer, and D. Meschede, *Standing light fields for cold atoms with intrinsically stable and variable time phases*, Optics Communications **148**, 45–48 (1998).

[118] F. Gerbier and Y. Castin, *Heating rates for an atom in a far-detuned optical lattice*, Physical Review A **82**, 013615 (2010).

[119] K. Weatherill, *A CO_2 Laser Lattice Experiment for Cold Atoms*, PhD thesis, Durham University, 2007.

[120] A. Ashkin, *Trapping of Atoms by Resonance Radiation Pressure*, Physical Review Letters **40**, 729 (1978).

[121] S. Chu, J. E. Bjorkholm, A. Ashkin, and A. Cable, *Experimental Observation of Optically Trapped Atoms*, Physical Review Letters **57**, 314 (1986).

[122] M. J. Webber, *Handbook of Optical Materials* (CRC Press, 2004).

[123] M. B. Squires *et al.*, *Ex vacuo atom chip Bose-Einstein condensate*, Applied Physics Letters **109**, 264101 (2016).

[124] A. Daffurn, R. F. Offer, and A. S. Arnold, *A simple, powerful diode laser system for atomic physics*, Applied Optics **60**, 5832 (2021).

[125] K. M. O'Hara, M. E. Gehm, S. R. Granade, and J. E. Thomas, *Scaling laws for evaporative cooling in time-dependent optical traps*, Physical Review A **64**, 051403 (2001).

[126] T. A. Savard, K. M. O'Hara, and J. E. Thomas, *Laser-noise-induced heating in far-off resonance optical traps*, Physical Review A **56**, R1095–R1098 (1997).

[127] L. Torralbo-Campo, G. D. Bruce, G. Smirne, and D. Cassettari, *Light-induced atomic desorption in a compact system for ultracold atoms*, Scientific Reports **5**, 14729 (2015).

[128] C. Monroe, PhD thesis, University of Colorado, 1992.

[129] S. Friebel, C. D'Andrea, J. Walz, M. Weitz, and T. W. Hänsch, *CO_2-laser optical lattice with cold rubidium atoms*, Physical Review A **57**, R20 (1998).

[130] J. Wu, R. Newell, M. Hausmann, D. J. Vieira, and X. Zhao, *Loading dynamics of optical trap and parametric excitation resonances of trapped atoms*, Journal of Applied Physics **100**, 054903 (2006).

[131] E. Batori, *Studies on miniature and compact Ramsey double-resonance Rubidium atomic clocks using hot vapors and cold atoms*, PhD thesis, University of Neuchâtel, 2023.

[132] E. Batori *et al.*, *An additive-manufactured microwave cavity for a compact cold-atom clock*, Journal of Applied Physics **133**, 224401 (2023).

[133] A. Bregazzi *et al.*, *A cold-atom Ramsey clock with a low volume physics package*, Scientific Reports **14**, 931 (2024).

[134] L. Essen and J. V. L. Parry, *An Atomic Standard of Frequency and Time Interval: A Cæsium Resonator*, Nature **176**, 280 (1955).

[135] M. A. Lombardi, T. P. Heavner, and S. R. Jefferts, *NIST Primary Frequency Standards and the Realization of the SI Second*, NCSLI Measure **2**, 74 (2007).

[136] J. Camparo, *The rubidium atomic clock and basic research*, Physics Today **60**, 33 (2007).

[137] S. Micalizio, C. E. Calosso, A. Godone, and F. Levi, *Metrological characterization of the pulsed Rb clock with optical detection*, Metrologia **49**, 425 (2012).

[138] J. Vanier and C. Mandache, *The passive optically pumped Rb frequency standard: the laser approach*, Applied Physics B **87**, 565 (2007).

[139] C. Stefanucci *et al.*, *Compact microwave cavity for high performance rubidium frequency standards*, Review of Scientific Instruments **83**, 104706 (2012).

[140] Q. Hao *et al.*, *A physics package for rubidium atomic frequency standard with a short-term stability of* $2.4 \times 10^{-13}\ \tau^{-1/2}$, Review of Scientific Instruments **87**, 123111 (2016).

[141] E. Batori *et al.*, *μPOP Clock: A Microcell Atomic Clock Based on a Double-Resonance Ramsey Scheme*, Physical Review Applied **18**, 054039 (2022).

[142] F.-X. Esnault, D. Holleville, N. Rossetto, S. Guerandel, and N. Dimarcq, *High-stability compact atomic clock based on isotropic laser cooling*, Physical Review A **82**, 033436 (2010).

[143] F. Esnault, N. Rossetto, D. Holleville, J. Delporte, and N. Dimarcq, *HORACE: A compact cold atom clock for Galileo*, Advances in Space Research **47**, 854 (2011).

[144] S. T. Müller, D. V. Magalhães, R. F. Alves, and V. S. Bagnato, *Compact frequency standard based on an intracavity sample of cold cesium atoms*, Journal of the Optical Society of America B **28**, 2592 (2011).

[145] P. Liu *et al.*, *Scheme for a compact cold-atom clock based on diffuse laser cooling in a cylindrical cavity*, Physical Review A **92**, 062101 (2015).

[146] S. Lee *et al.*, *A compact cold-atom clock based on a loop-gap cavity*, Applied Physics Letters **119**, 064002 (2021).

[147] Muquans, *MuClock data sheet*, Available Online at https://www.muquans.com/product/muclock/, Accessed Jan 2023.

[148] Spectra Dynamics, *cRb Clock data sheet*, Available Online at https://spectradynamics.com/products/crb-clock/, Accessed Jan 2023.

[149] AOSense, *Cold-Atom Frequency Standard data sheet*, Available Online at https://aosense.com/product/cold-atom-frequency-standard/, Accessed Jan 2023.

[150] M. Givon *et al.*, *In-vacuum microwave resonator for a compact cold atom frequency standard*, 2022, arXiv:2208.09038.

[151] S. Kang, M. Gharavipour, C. Affolderbach, F. Gruet, and G. Mileti, *Demonstration of a high-performance pulsed optically pumped Rb clock based on a compact magnetron-type microwave cavity*, Journal of Applied Physics **117**, 104510 (2015).

[152] C. Affolderbach *et al.*, *Study of additive manufactured microwave cavities for pulsed optically pumped atomic clock applications*, Applied Physics Letters **112**, 113502 (2018).

[153] E. Batori *et al.*, *μ_{POP} Clock: A Microcell Atomic Clock Based on a Double-Resonance Ramsey Scheme*, Physical Review Applied **18**, 054039 (2022).

[154] M. Gozzelino *et al.*, *Realization of a pulsed optically pumped Rb clock with a frequency stability below 10^{-15}*, Scientific Reports **13**, 12974 (2023).

[155] Microchip, *MHM-2020 Active Hydrogen Maser data sheet*, Available Online at https://www.microchip.com/en-us/products/clock-and-timing/components/atomic-clocks/atomic-system-clocks/mhm-2020-hydrogen-masers, Accessed August 2023.

[156] S. Micalizio, A. Godone, F. Levi, and C. Calosso, *Medium-long term frequency stability of pulsed vapor cell clocks*, IEEE Transactions on Ultrasonics, Ferroelectrics and Frequency Control **57**, 1524 (2010).

[157] T. D. Ngo, A. Kashani, G. Imbalzano, K. T. Nguyen, and D. Hui, *Additive manufacturing (3D printing): A review of materials, methods, applications and challenges*, Composites Part B: Engineering **143**, 172 (2018).

[158] M. Pellaton *et al.*, *3D printed microwave cavity for atomic clock applications: proof of concept*, Electronics Letters **54**, 691 (2018).

[159] P. A. Redhead, *Recommended practices for measuring and reporting outgassing data*, Journal of Vacuum Science & Technology A: Vacuum, Surfaces, and Films **20**, 1667 (2002).

[160] N. Cooper *et al.*, *Additively manufactured ultra-high vacuum chamber for portable quantum technologies*, Additive Manufacturing **40**, 101898 (2021).

[161] B. Lewis, *A cold-atom fountain clock from a diffractive optic*, PhD thesis, University of Strathclyde, 2022.

[162] B. Lewis, R. Elvin, A. S. Arnold, E. Riis, and P. F. Griffin, *A grating-chip atomic fountain*, Applied Physics Letters **121**, 164001 (2022).

[163] G. H. Zhang, B. Braverman, A. Kawasaki, and V. Vuletić, *Note: Fast compact laser shutter using a direct current motor and three-dimensional printing*, Review of Scientific Instruments **86**, 126105 (2015).

[164] D. S. Barker *et al.*, *Grating magneto-optical traps with complicated level structures*, New Journal of Physics **25**, 103046 (2023).

[165] Y.-X. Duan *et al.*, *State Preparation in a Cold Atom Clock by Optical Pumping*, Chinese Physics Letters **34**, 073201 (2017).

[166] W. M. Itano *et al.*, *Quantum projection noise: Population fluctuations in two-level systems*, Physical Review A **47**, 3554 (1993).

[167] D. Allan, *Time and Frequency (Time-Domain) Characterization, Estimation, and Prediction of Precision Clocks and Oscillators*, IEEE Transactions on Ultrasonics, Ferroelectrics and Frequency Control **34**, 647 (1987).

[168] J. Rutman, *Characterization of phase and frequency instabilities in precision frequency sources: Fifteen years of progress*, Proceedings of the IEEE **66**, 1048 (1978).

[169] A. V. Rakholia, H. J. McGuinness, and G. W. Biedermann, *Dual-Axis High-Data-Rate Atom Interferometer via Cold Ensemble Exchange*, Physical Review Applied **2**, 054012 (2014).

[170] F.-X. Esnault *et al.*, *Cold-atom double-Λ coherent population trapping clock*, Physical Review A **88**, 042120 (2013).

[171] G. W. Hoth *et al.*, *Towards a compact atomic clock based on coherent population trapping and the grating magneto-optical trap*, in *Optical, Opto-Atomic, and Entanglement-Enhanced Precision Metrology*, edited by S. M. Shahriar and J. Scheuer, SPIE, 2019.

[172] B. Adams, S. Kinge, K. Bongs, and Y. H. Lien, *Magneto-optical trap performance for high-bandwidth applications*, Physical Review A **108**, 063111 (2023).

[173] G. Santarelli *et al.*, *Quantum Projection Noise in an Atomic Fountain: A High Stability Cesium Frequency Standard*, Physical Review Letters **82**, 4619 (1999).

[174] F. Esnault *et al.*, *Reaching a few $10^{-13}\tau^{-1/2}$ stability level with the compact cold atom clock HORACE*, in *2008 IEEE International Frequency Control Symposium*, pp. 381–385, IEEE, 2008.

[175] G. Santarelli *et al.*, *Frequency stability degradation of an oscillator slaved to a periodically interrogated atomic resonator*, IEEE Transactions on Ultrasonics, Ferroelectrics and Frequency Control **45**, 887 (1998).

[176] E. Rubiola and F. Vernotte, *The Companion of Enrico's Chart for Phase Noise and Two-Sample Variances*, IEEE Transactions on Microwave Theory and Techniques **71**, 2996 (2023).

[177] C. E. Calosso *et al.*, *Intensity Detection Noise in Pulsed Vapor-Cell Frequency Standards*, IEEE Transactions on Ultrasonics, Ferroelectrics, and Frequency Control **67**, 1074 (2020).

[178] D. C. Aveline *et al.*, *Observation of Bose–Einstein condensates in an Earth-orbiting research lab*, Nature **582**, 193 (2020).